UNIVERSIDADE FEDERAL DE ALAGOAS
INSTITUTO DE FÍSICA

PEDRO VICTOR B B P DE MELO

Nonlinear and electro-optical properties of liquid crystal systems doped with gold nanorods

Maceió - Brasil

June - 2019

PEDRO VICTOR B B P DE MELO

Nonlinear and electro-optical properties of liquid crystal systems doped with gold nanorods

Trabalho de dissertação apresentado no Instituto de Física da Universidade Federal de Alagoas, como parte dos requisitos para a obtenção do título de Mestre em Física.

Orientador: Prof. Dr. Italo Nunes de Oliveira

Maceió - Brasil

June - 2019

PARECER DA BANCA EXAMINADORA DE DEFESA DE

DISSERTAÇAO DE MESTRADO

"Nonlinear and electro-optical properties of liquid crystal systems doped with gold nanorods"

por

Pedro Victor Bulhoes Barros Portela de Melo

A Banca Examinadora composta pelos professores Italo Marcos Nunes de Oliveira (presidente da banca e orientador), do Instituto de Física da Universidade Federal de Alagoas, Marcelo Leite Lyra, do Instituto de Física da Universidade Federal de Alagoas, Artur da Silva Gouveia Neto, do Instituto de Física da Universidade Federal de Alagoas e Fernando Jorge Sampaio Moraes, da Universidade Federal Rural de Pernambuco consideram o candidato aprovado com grau " _A_ ".

Maceió, 16 de julho de 2019

Prof. Dr. Italo Marcos Nunes de Oliveira

Prof. Dr. Marcelo Leite Lyra

Prof. Dr. Artur da Silva Gouveia Neto

Prof. Dr. Fernando Jorge Sampaio Moraes

Agradecimentos

Aproveito este espaço para agradecer a todos que contribuíram de maneira direta e indireta durante esses últimos anos da minha formação.

Ao grupo de pesquisa, por possibilitar o presente trabalho. Em especial meu orientador Italo e meus companheiros de trabalho Rafael e Ricardo, que colaboraram de maneira direta com os resultados obtidos aqui, e Catharina, me ajudando bastante com a correção dos erros de digitação na escrita.

Além da parte profissional, agradeço à amizade e apoio recebido por todos. Ao pessoal da sala 6 e agregados, pela convivência. Todos são pessoas especiais que influenciam ou influenciaram cotidianamente a minha vida. Rafael (Frango) e Ric, pelas discussões sem fim sobre qualquer assunto, contanto que seja inútil, pela honestidade e camaradagem. Raul, Elenilda (Mochileira) e Pâm, pelas conversas e risadas nos nossos dias. Caca, Débye e Waltinho, pelo apoio, proteção, carinho e compreensão incondicionais. Não imagino o que seria hoje sem o amor que recebo a todo momento. Ellena (Juliana), por tantos anos de compaixão e paciência. Italo, Socorro e Sérgio, pela complacência, pelos conselhos sobre a vida e disponibilidade integral para qualquer assunto.

Aos amigos de instituto, pelo sossego e leveza diários. Ao Luan, pela franqueza e permanecer proximidade irrestrita. Michele, por me fornecer uma visão da vida tão diferente da que eu tenho e me fazer pensar. Wand, pela serenidade, sensatez e humanidade. Ao João, meus parabéns por conseguir fazer a Caca te aguentar. Léo, por inspirar tranquilidade. Aos outros amigos e colegas do cotidiano no instituto, meus agradecimentos pela amizade e respeito, de coração.

À minha família, pela animação e alegria constantes. Vó Chica, pelas companhias de finais de semana. Vô Dêvis, pelas boas memórias que deixou. À Senadora e ao Prefeito, pelas boas risadas. À minha mãe, pela justiça e amor. Ao meu pai, pela confiança. Aos meus irmãos, pelo respeito. Aos meus tios, infelizmente são muitos e não terei condições de citar aqui, mas pela influência e inspiração. À Cris, pela disposição.

Aos meus amigos e companheiros ou ex-companheiros de treino, meu muito obrigado.

Amoredo e Juninho, pelo apoio e preocupação incessantes. Clênio (Ogro) pela grande amizade que persiste com o tempo, mesmo com as distâncias. Karina e Louise, pelos desabafos e ouvidos pacientes, além da alegria constante.

Caso tenha me esquecido de alguém, meu sincero perdão. Estou tendo que escrever isso meio nas pressas para defender com urgência.

Abstract

The present study is devoted to the investigation of the reorientation and nonlinear optical properties of 8CB liquid crystal samples doped with gold nanorods with distinct width to length ratios (aspect ratios). By using the Z-scan technique, the mechanisms behind phase distortions and nonlinear absorption by samples under homeotropic anchoring conditions are evaluated. Our results reveal that thermal effects are the leading phenomena causing distortions in the incident beam wavefront for normal light incidence. When the oblique incidence regime is concerned, nonlinearities in the refractive index play a larger role in phase shifts, due to the reorientation of the far-field director caused by the electric field of impinging light. The temperature dependence of $\chi^{(3)}$ nonlinearities are investigated, where an anomalous behavior of the nonlinear refractive index is observed close to the nematic-smectic-A phase transition. In addition, a gradual increase in magnitude of the nonlinear absorption coefficient appears at temperatures where the smectic order is well-established. Furthermore, the effects of gold nanorod aspect ratio in the viscoelastic properties of twisted nematic cells under an AC electric field are explored, with a reduction in the Freedericksz threshold voltage being accounted as impurities are introduced in the sample. A decrease of reorientation times is reported for samples containing gold nanorods compared to the undoped liquid crystal, with a further reduction in the system containing more elongated nanoparticles. The longitudinal plasmonic extinction band was also excited in order to evaluate the contributions of the surface plasmon resonance to switch times. The Gooch-Tarry conditions and Mauguin minima are also exploited to extract the thermal dependence of the nematic birefringence of samples, where a decreased discontinuity in the nematic order parameter is observed for doped materials. A thorough discussion of the interplay between the introduction of gold nanorods and the liquid-crystalline order is performed, unveiling the possibility of novel applications for plasmonic systems.

Keywords: liquid crystals, gold nanorods, nematic reorientation.

Resumo

O presente trabalho é voltado para a investigação das propriedades de reorientação e ópticas não-lineares de amostras de 8CB dopadas com nanobastões de ouro em distintas razões de comprimento por raio (razão de aspecto). Utilizando a técnica de Z-scan, os mecanismos responsáveis pelas distorções de fase e absorção não-linear em amostras com ancoramento homeotroópico são avaliados. Nossos resultados revelam que efeitos térmicos são o principal fenômeno causando distorções na frente de onda do feixe para incidência normal. Quando o regime oblíquo é considerado, contribuições não-linearidades no índice de refração desempenham um papel maior nas distorções de fase, devido à reorientação do diretor de campo distante causada pelo campo elétrico da luz incidente. A dependência com a temperatura das contribuições de $\chi^{(3)}$ para a não-linearidade são investigadas, onde um comportamento anômalo do índice de refração não-linear é observado próximo da transição de fase nemática-esmética-A. Além disto, um aumento gradual em valor absoluto do coeficiente de absorção não-linear surge em temperaturas onde a ordem esmética é bem estabelecida. Além disso, os efeitos da razão de aspecto nas propriedades viscoelásticas de células nemáticas twist submissas a um campo elétrico AC são exploradas, com uma redução na voltagem limiar de reorientação sendo observada quando impurezas são introduzidas na amostra. Uma redução dos tempos de reorientação é observada para amostras contendo nanobastões comparado com a amostra pura, com um efeito mais pronunciado no sistema contendo as nanopartículas mais alongadas. A banda de extinção plasmônica longitudinal é excitada com o objetivo de avaliar as contribuições da ressonância plasmônica de superfície para os tempos de reorientação. As condições de Gooch-Tarry e mínimos de Mauguin são explorados com o intuito de extrair a dependência térmica da birrefringência nemática das amostras, com uma redução da descontinuidade do parâmetro de ordem nemático sendo observada para materiais dopados. Uma discussão da relação entre a introdução de nanobastões de ouro e a ordem líquida-cristalina é investigada, revelando a possibilidade de novas aplicações para sistemas plasmônicos.

Palavras-chave: cristais líquidos, nanobastões de ouro, reorientação nemática.

Contents

1

Introduction to liquid crystals

1.1 Order and states of matter

Liquid crystals are, in essence, a state of matter possessing properties in between those presented by solids and those presented by liquids. It is, however, not quite simple to define a liquid crystal without introducing some prior concepts. As stated by de Gennes and Prost, "to understand the significance of these new states of matter, it may be useful to recall first the distinction between a crystal and a liquid" [1].

Let us start by defining what would be a crystal. Crystals are structures presenting a very special property: if one has a primitive pattern located at a certain position, say, $\vec{x}_0$, and one goes arbitrarily far from that point, the probability of finding the same pattern remains finite. Experimental-wise, the Bragg X-ray scattering will show sharp peaks periodically. These are signs of a highly ordered microscopic structure. Since crystals present this degree of order, they can be defined by what is called a Bravais lattice, an infinite array of atoms distributed throughout space, generated by the repetition of a minimum cell. Mathematically, this can be described as [2, 3]

$$\vec{R} = n_1 \hat{a}_1 + n_2 \hat{a}_2 + n_3 \hat{a}_3, \tag{1.1}$$

where n_i are integers and $\hat{a}_i$ are the basis vectors which span the lattice throughout space. If one walks away from $\vec{x}_0$ to a new point $\vec{x}$ in space, the structure located around such

point will be described as

$$\vec{R} = \vec{x} + n_1 \hat{a}_1 + n_2 \hat{a}_2 + n_3 \hat{a}_3, \tag{1.2}$$

which represents a repetition of the original pattern, recovering our initial concepts of how a crystal should be like.

One way to quantify the order in a system commonly adopted in statistical mechanics is the use of correlation functions. In the canonical ensemble, one may define the correlation function as the thermal average of the inner product of two variables, say, $\vec{s}_1(\vec{r}, t)$ and $\vec{s}_2(\vec{r}, t)$ at distinct positions and times [4]. That is,

$$C(\vec{r}, t) \equiv \langle \vec{s}_1(\vec{r}, t) \cdot \vec{s}_2(\vec{r} + \vec{r}', t + t') \rangle. \tag{1.3}$$

The random variables here need not be different. $\vec{s}_1$ and $\vec{s}_2$ may refer to the same quantity, as the spin of electrons, the density of molecules, or the positions of the center of mass of particles. Correlation functions, hence, give us insight on how two microscopic variables will be related to one another across space and time on average. We may as well consider the steady-state (or equilibrium state) of a system, where temporal evolutions are irrelevant and only spatial correlations are of significance (t' is set to zero in equation (1.3)).

Through X-ray crystallography experiments, one may determine experimentally how the microscopic structure of materials is ordered. The procedure consists in bombing samples with X-rays, which will be diffracted to many directions with varying intensities, according to the atomic or molecular structure of the material. Inspecting the specific directions and amplitudes, a picture of the electron density within the sample may be constructed, leading to a reckoning of the molecular or atomic arrangement of the material.

A crystal X-ray diffraction pattern, for instance, will be described as

$$\lim_{|\vec{x} - \vec{x}'| \to \infty} \langle \rho(\vec{x}) \rho(\vec{x}') \rangle = F(\vec{x} - \vec{x}'), \tag{1.4}$$

11

where $\langle \rho(\vec{x})\rho(\vec{x}') \rangle$ is the density-density correlation function (or pair correlation function) and $F(\vec{x} - \vec{x}')$ a periodic function of vector basis $\vec{a}$. In other words, if one starts at a point $\vec{x}$ and walks arbitrarily far away from that point to a new position $\vec{x}'$, the density of atoms or molecules on a thermal average will be related by some periodic function of position, no matter how far $\vec{x}$ is from $\vec{x}'$.

Liquids, on the other hand, present a whole different set of properties. The probability of finding a similar structure in a different place in an isotropic liquid vanishes as one gets far away from the reference, except for an average density. That is,

$$\lim_{|\vec{x} - \vec{x}'| \to \infty} \langle \rho(\vec{x})\rho(\vec{x}') \rangle \simeq \bar{\rho}^2. \tag{1.5}$$

Liquids present an isotropic length scale for which all correlations are lost, usually called ξ. On the measurements of X-ray diffraction, diffuse peaks with typical width ξ^{-1} appear. These properties make liquids disordered, even though their molecules are strongly interacting.

Liquid crystals are a mix between both states of matter. They must present isotropic liquid-like order in at least one dimension, and its density-density correlation function does not depend solely on the positions of the center of mass of each particle, but also their orientation with respect to a defined axis.

Considering three-dimensional space, one can classify liquid crystals in three main broad categories:

- Centers of mass presenting isotropic liquid-like order, but with anisotropic correlation lengths. That is, there being two typical length scales for which disorder appears, $\xi_\perp$ and $\xi_\parallel$ (or order decays);

- Centers of mass presenting crystalline order in one direction only, and the other two presenting isotropic liquid-like typical length decays;

- Centers of mass presenting crystalline order in two directions, with the third direction order decaying as an isotropic liquid.

The first category given here is what is usually called a *nematic*: a phase where the centers of mass of molecules seem to be disordered, with the disorder, however, decaying differently in two specific definite directions. The word nematic comes from the Greek $\nu\eta\mu\alpha$ (nema), which means "thread", in reference to the topological defects appearing in nematics. The second category would be what is commonly known as a *smectic*. Since the centers of mass present crystalline order in one direction, they arrange in such a way to form well-defined layers, but their lack of high degree of order in the other two dimensions make the molecules within a layer able to flow smoothly along it, and layers able to slide over one another. The word smectic comes from the Latin "smecticus", meaning cleaning, a reference to soap-like properties. The third category represents the *columnar* phases, where molecules arrange themselves in a two-dimensional array, stacking over one another, forming columns within the sample. Because of the absence of a high degree of ordering in the third direction, molecules may flow within a same column.

Not all materials present liquid-crystalline phases (also called mesophases), and neither do all materials that present them, present all of the phases. In particular, if a mesophase is achievable in some material, that liquid-crystalline state of matter need not be the only mesophase that such material presents. There may be multiple phase transitions between these several possibilities of liquid-crystalline orderings, where the same material can present one or many phases depending on its physical conditions.

In order for a chemical compound to exhibit mesophases, molecules must present some specific molecular geometry in which anisotropy is innate. As we have described before, their density-density correlation function has to depend on the molecular orientation with respect to a definite axis, even when the positions of the centers of mass present no long-range order. There are two main candidates that appear frequently in nature: elongated (prolate, or calamitic) and disc-like (oblate) molecules, being either chiral or achiral. For the purpose of this work, two specific mesophases formed by achiral calamitic molecules will be discussed.

Figure 1.1: Schematic representation of molecules constituting nematic (a) and smectic-A (b) phases, showing the mean molecular alignment to a fixed far-field direction, as well as the layered structure present in (b), the less symmetric phase.
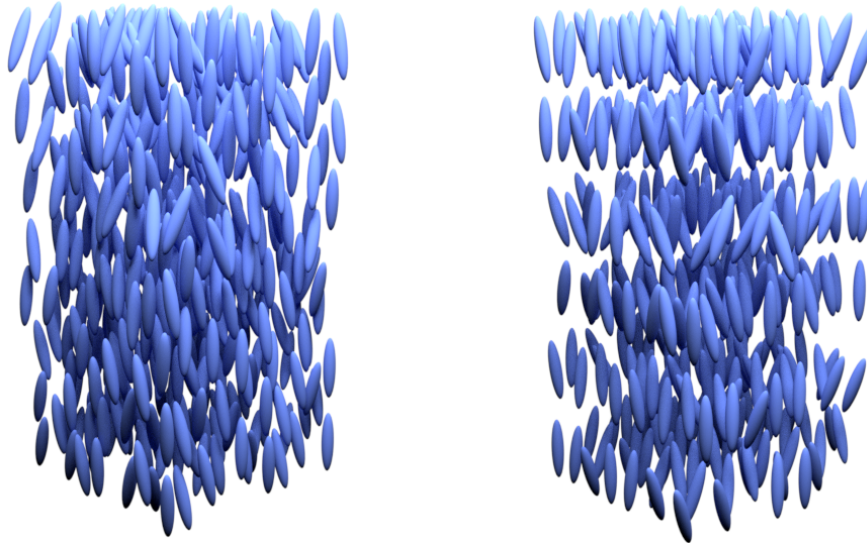
Source: Author (2019).

1.2 Liquid-crystalline phases

Thermotropic liquid crystals are a class of materials exhibiting liquid-crystalline phases under specific thermodynamic conditions. For a certain temperature range (considering pressure values around sea-level standard), thermal fluctuations will not be high enough to drive the system to an isotropic state, but sufficient to destroy highly ordered crystalline assemblies. Under such range, our material will present physical properties lying in one of the categories described in the previous section, and may even transition between one another, if heated or cooled. For example, a compound may present a smectic phase and exhibit a transition to the less ordered nematic phase before reaching an isotropic state, or even transitions between other smectic phases. For the next subsections, we will delve a little bit more into the physical properties of nematics and smectics, as well as phase transitions between both.

1.2.1 Uniaxial nematics

A nematic liquid crystal is a liquid-crystalline mesophase where the centers of mass of the constituting molecules present no long-range order. Equivalently, it is common to hear that nematics present no long-range *positional* order. In this aspect, they are

just like liquids, except for the anisotropy in the correlation length scales. However, the molecules self-align to compose long-range directional order. If, for example, the molecular shape is calamitic (rod-shaped), their long axes point, on an average, to the same direction. Such properties make nematics free to flow just like liquids, but their preferred orientation reflects in the macroscopic tensor properties, ensuing, for instance, in optical, dielectric and magnetic anisotropy, like crystals do. This preferred molecular orientation is usually called $\vec{n}$, the director vector. Due to the molecular anisotropy, $\vec{n}$ is easily realigned by magnetic or electric fields. Another important property of the director is that the directions $\vec{n}$ and $-\vec{n}$ must be indistinguishable. If molecules carry any dipole moment, they will cancel out throughout the bulk, mainly based on two arguments: If dipoles are really present and molecules are asymmetric in shape, there will be as many shapes "up" as there will be "down", for any imbalance would be punished by steric interactions causing costly elastic distortions along the material, an argument that can be proven mathematically [5]. On the other hand, if no asymmetry is present on molecular shape, a problem arises with known physical interactions between molecules: the exchange couplings are much weaker than other conventional molecular interactions, such as van der Waals, steric repulsion, and so on. Ferromagnetic liquid crystals have been reported before, but they are a result of magnetic nanoparticle suspensions [6], not magnetic dipole-carrying molecules. For most of the cases, the director may be regarded as symmetric, since such lack of symmetry is an exception in nowadays most considered liquid-crystalline systems. A schematic representation of uniaxial nematics is shown in figure 1.1(a).

1.2.2   Smectic-A phase

A smectic liquid crystal is a mesophase that occurs at lower temperatures than nematics. The centers of mass this time present quasi-long range order in one direction, giving rise to a layered structure. Molecules within one layer may flow freely along their layers, and layers can slide smoothly one over another. Along the other directions, smectics present no long-range order. Furthermore, smectics also present long-range orientational order in one direction, just like nematics, where we may also define a director vector $\vec{n}$

to the smectic phase, presenting the same properties discussed before for the director vector of the nematic phase. Since now we have two vectors, namely, the normal to layer surface and $\vec{n}$, one may define an angle, say, α, between these two directions. If $\alpha = 0$, for instance, the smectic phase is called a smectic-A. If otherwise, the state of matter is called smectic-C. Once again, the director orientation and layered structure guarantee anisotropic macroscopic tensor properties. Other smectic phases presenting triangular lattice positional ordering that extends through a few dozens of nanometers are also possible, and are called hexatic smectics [1], but will not be discussed here. A schematic representation of smectic-A is shown in figure 1.1(b).

1.3 Liquid crystal cells

Since the direction of $\vec{n}$ is, to this point, arbitrary in space, it is useful to impose minor forces in the material, such as boundary conditions on the walls of the sample container (or cell). By guiding the average direction of molecules, one can also guide the axis on which anisotropy will occur. This same feature can be achieved adjusting the direction and magnitude of external fields. Understanding the conformation of molecules subject to surface alignments and their behavior under the influence of external fields, one may control mechanical, optical, electrical, magnetic, and thermal effects; enabling oneself to extract useful physical properties from the systems.

Two main alignment conditions are usually employed in liquid crystal research, namely, homeotropically- and homogeneously-aligned surfaces. The former induces a perpendicular alignment of molecules at the substrate, and it may be achieved in practice by chemically treating glass surfaces with surfactants and detergents, such as silanes or special polyimide compounds. Homogeneously-aligned surfaces impose alignment parallel to the substrate, usually along a definite, constant, direction. To achieve this state, polyimide may be deposited over the glass surface and be mechanically rubbed afterwards with velvet or paper, towards the direction of desired alignment. By combining two substrates of known alignment conditions, one may produce cells with diverse director profiles. See, for example, the states represented in figure 1.2.

Figure 1.2: Parallel planar, homeotropic and twist alignment cells, filled with an achiral calamitic liquid crystal. Homogeneous alignment glass surfaces force molecules to align parallel to the substrate, while homeotropic alignment glass surfaces force molecules to align perpendicular to the substrate. By setting two homogeneously aligned glass surfaces with their alignment direction parallel to each other, the director stays constant throughout the sample, parallel to the substrates, and uniform along the bulk. Homeotropically-aligned cells are observed when two surfaces imposing perpendicular boundary conditions on the molecules in contact with the glass surface are placed parallel to each other. In such configuration, the director will be constant and perpendicular to the substrates throughout the sample. If one now builds a cell with two homogeneously-aligned glasses, but the angle between the two alignment directions is non-null, the director will follow a smooth helical path until reaching the other plate, satisfying the boundary conditions. A combination between one homogeneously- and one homeotropically-aligned cell is also possible, but not shown here.
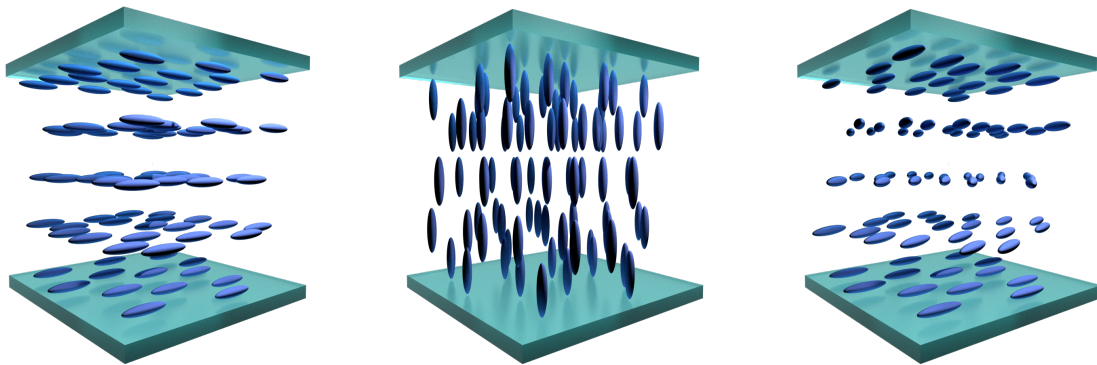
Source: Author (2019).

In order to produce regular cells, two aligned glass plates may be put parallel to each other, separated by strips of some film of fixed thickness, such as silica, mylar, or cellulose. The gap between both substrates may then be filled with a liquid-crystalline material. If we consider a calamitic achiral liquid crystal between two glass surfaces homogeneously-aligned in the same direction, the director will remain uniform throughout the sample, parallel to the glass surfaces and constant along the bulk. Such configuration is called parallel planar, and is the first cell type represented in figure 1.2.

Since the alignment direction in parallel planar cells is known, the director is known, and so is the anisotropy axis. That way, it's possible to deal with an optically isotropic or anisotropic material, depending only on the angle between the polarization of incident light and alignment direction. For instance, if incident light presents a linear polarization parallel or perpendicular to the director, the material will behave as an optically isotropic sample. Equivalently, it is possible to observe a birefringent material with any possible combination of the two indices of refraction, depending on the angle between $\vec{n}$ and the polarization of light. Due to their anisotropic nature, liquid crystal molecules are also

easily reoriented when interacting with external fields. An external electric field may also be employed to reorient the director, and the anisotropy axis may be fine-tuned by field strength, an easily controlled parameter. Such feature makes planar alignment cells suitable to useful everyday applications, such as display technology, where samples may go from a fully isotropic to a strongly anisotropic state, depending only on the switching of an external field.

Similarly, two parallel homeotropically-aligned glass surfaces will induce a perpendicular orientation of molecules over the glass surface, and such preferred mean orientation will hold throughout the bulk, making the director perpendicular to the substrate. Those are usually called homeotropic cells, and are represented as the second cell type in figure 1.2. This configuration is optically isotropic for perpendicular incidence, independent of light polarization direction, unlike planar cells. Even though only the ordinary axis is accessible for this case, this may actually be of some help in cells being insensitive to alignment along the optical axis, and thus reducing errors in experiments. Such feature makes homeotropic cells filled with liquid crystals presenting positive dielectric anisotropy less common in technological applications, but extremely useful for experimentation.

The third configuration shown in figure 1.2 is the twisted alignment, in which two homogeneously-aligned surfaces are put together such as their alignment directions make a definite angle between each other. The director will be parallel to the surfaces, and vary smoothly in a way to satisfy the boundary conditions at both substrates. That is, $\vec{n}$ will rotate in a helical fashion, with the helical axis perpendicular to the glass surfaces. This somewhat curious conformation has interesting properties. If we consider the twisting angle being $\pi/2$ rad, for example, polarized light at certain wavelengths impinging the sample perpendicularly will have its polarization follow the helix of the director and be rotated by $\pi/2$ rad exactly, if the initial polarization direction is parallel to the input substrate alignment. Such calculations will be performed later in this text. This feature will be almost perfect for wavelengths ranging from the whole visible to ultraviolet spectrum, making twisted nematic samples completely dark in between parallel polarizers and almost transparent when placed between crossed polarizers (if the "correct" alignment

of polarizers is ensured). For molecules with positive dielectric anisotropy, an external electric field can be applied perpendicular to the glass surfaces and induce a state similar to the homeotropic alignment mentioned before, making the sample optically isotropic. In other words, samples can go from fully bright to dark (or the opposite, depending on whether polarizers are perpendicular or parallel to each other) by controlling an external field. For the aforementioned reason, twisted nematic cells are frequently used in display technology and light modulation devices.

Regarding the elastic response of molecules to electronically-applied external fields, uniaxial liquid crystals may present either negative or positive anisotropies, depending on the microscopic characteristics of the material and physical conditions under which the material is subjected to. For instance, when the frequency of external AC electric fields is increased, the formerly positive dielectric anisotropy of materials is decreased and eventually reverted to negative values [7]. Such distinction between positive or negative anisotropy leads to very different responses for identical stimuli. An external electric field will induce director reorientation, to be parallel to the field in the case of positive dielectric anisotropy and perpendicular for a negative sign. In practice, external uniform electric fields may be easily induced perpendicular to the cell surfaces. The procedure consists in coating glass surfaces with indium tin oxide and applying a voltage between both plates.

One simple and illustrative demonstration of how liquid crystal cells might be useful for everyday applications is the simple twisted nematic liquid crystal display itself (TN-LCD). It consists in one of the most fundamental examples of an electrically-controlled birefringence device using liquid crystals, which enables the fast, efficient, and low power consumption switching between two states — namely, one completely bright to the human eye and another completely dark. When placed between crossed polarizers, a $\pi/2$ rad twisted nematic cell will almost perfectly rotate the polarization of visible and ultraviolet light, in a way that it exits the cell with a polarization state practically perpendicular to the input state; making the display completely bright to the human eye. A voltage may then be applied to both glass substrates, where the ensuing electric field will reorient the far-field director. That is, the field will sway positive dielectric anisotropy molecules to

Figure 1.3: Schematic representation of a twisted nematic liquid crystal display set to the naturally-on state. Considering a positive dielectric anisotropy, when an electric field is applied perpendicular to glass surfaces, a reorientation of the director occurs, destroying the formerly twisted director pattern and giving rise to a new configuration, where molecules will try to align parallel to the applied field. To induce a completely off state, voltages of approximately $2-5$ times the threshold voltage (around 1.5 to 4 V) are required for usual cyanobiphenyls, as will be shown later in text. Such state is called the electrically-switched-off state.
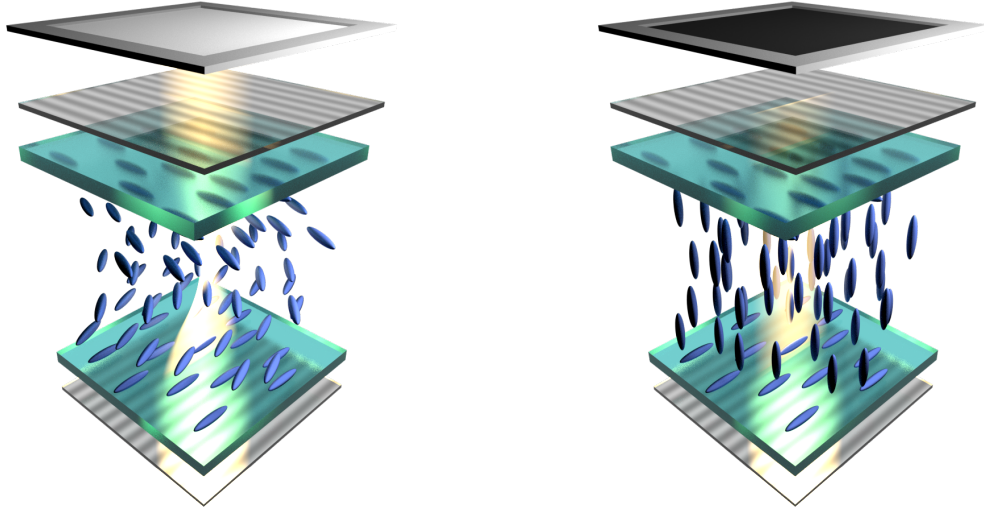
Source: Author (2019).

try to align along the field lines in order to minimize free energy. This new configuration of reoriented molecules is now optically isotropic, and the display appears completely dark between crossed polarizers. A depiction of the TN-LCD is shown in figure 1.3.

It is important to stress that by no means liquid crystal technology is nowadays limited to displays. Due to their light-modulating properties, simplicity to implement external control, and fine-tuning of sample responses, liquid crystals are ubiquitous in many technological application branches nowadays. For example, tunable band gap cholesteric LCs have proven to be well suited for several photonic applications, including — but not limited to — adjustable optical filters [8, 9], electro-tunable diodes [10], as well as tunable lasers [11, 12, 13, 14]. The optical properties of twisted nematic cells make them outstanding phase and amplitude modulating devices, being noteworthy candidates for applicabilities at phase retardation plates, liquid crystal displays, and spatial light modulators [15, 16, 17, 18]. Another remarkable example is the role played by liquid crystals in tunable metamaterials technology, a branch that is quickly developing over the past years [19, 20, 21, 22, 23, 24].

1.4 Liquid crystalline guest-host systems

Doping liquid crystals with guest molecules and/or particles may lead to dramatical effects on the macroscopic sample properties. To improve the response of liquid crystals, one may take advantage of the introduction of guests inside liquid crystal samples and their curious responses. Chiral dopants, for instance, induce cholesteric and chiral smectic phases, and may give rise to ferroelectric materials well suited for practical applications [25, 26]. Dichroic dyes might present tunable optical absorption, according to amplitudes of external electric fields for samples undergone Freedericksz transitions [27, 28]. Ferro-electric nanoparticles may increase nematic to isotropic transition temperatures by values as high as 5 K, as well as present a dramatic enhancement in the sensitivity to external fields [29], and considerable improvements in two-beam coupling [30]. Due to their large dimensions compared to molecular scales, colloidal particles induce elastic distortions in the nematic order, bringing about long-range interactions, thus enabling the arrangement of several self-assembled structures [31, 32, 33].

Overall, guest-host systems have proven to yield several improvements in optical, elastic, and thermodynamic properties, as well as novel responses; features yet to be re-ported for undoped samples. Recently, a lot of attention has been drawn to the study of liquid-crystalline systems containing plasmonic nanoparticles as the doping agent. Due to advances in synthesis methods, a fine-tune of nanoparticle shape, size, and surface anchor-ing conditions can be achieved. The introduction of such colloidal nanoparticles brings about topological defects around the impurities, depending on the capping agent used to stabilize dispersions (see figure 1.4). Consequently, disturbances of the orientational order will follow, reflecting in macroscopic elastic responses. Moreover, surface plasmon resonance has proven to be of fundamental importance to some electro-, thermo-, and nonlinear optical properties of samples due to collective phenomena; where size, shape and anisotropy have played major roles in dictating observed behaviors [34].

Gold nanoparticles, for instance, have shown to induce local electric fields around themselves, due to plasmonic excitation by incident light. Those local fields, in turn, cause director reorientation around the impurity centers, yielding a change in the refractive

Figure 1.4: Schematic representation showing a rod-shaped nanoparticle with different surface anchoring conditions. Note how different anchoring conditions bring about fundamentally distinct topological defects. For homeotropic anchoring (a), a disclination ring is observed. For parallel anchoring (b), two surface boojums at extremities of the nanorods are observed. For gold nanorod syntheses, one may employ different capping agents that are equally efficient at colloidal stabilization and aggregate prevention, but each inducing distinct anchoring conditions at the nanoparticle surface. For example, cetyltrimethylammonium bromide (CTAB) induces homeotropic anchoring conditions, while parallel boundary conditions are expected for m-polyethylene glycol (m-PEG) stabilization.
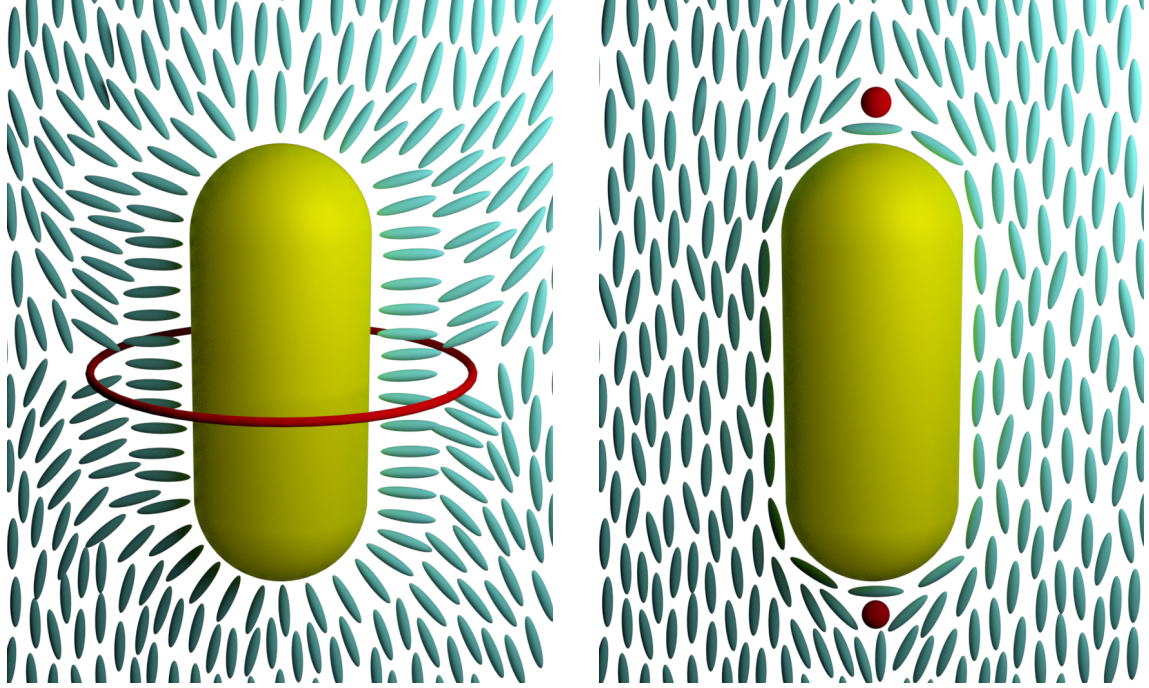
Source: Author (2019).

indices of the sample [24]. Enhanced nonlinear optical responses of nematic liquid crystals were also reported, where gold nanoparticles act as heat sources, with effects improving as concentration of dopants increases [35]. Lyotropic liquid crystals doped with gold nanospheres present an enhanced thermo-optical and nonlinear optical response as colloid concentrations rise, with a stronger dependence on the number of nonmesogenic impurities compared to aqueous dispersions [36].

In particular, it was previously reported that for homeotropic samples in the vicinities of the nematic-smectic-A phase transition, the critical behavior of the thermal diffusivity and thermal beam phase shift is responsive to the shape of gold nanoparticles, with a suppression of the discontinuities being more pronounced in the sample containing gold nanospheres than in the sample containing nanorods. Furthermore, for temperatures where the smectic order is well-established, a saturation of the single-photon absorption is reported in the sample containing gold nanorods, indicating that as temperatures are

reduced, local thermal fluctuations of the director are further hindered, influencing an overall alignment of the nanorods and the advent of a collective nonlinear response [34]. Even though a plethora of studies discuss the plasmonic effects on the thermo-optical and nonlinear optical properties of liquid crystals, only a few of them are devoted to analyzing the effects of the smectic ordering.

A lot of attention has also been drawn over the past years to the investigation of electro-optical responses in nematic liquid crystals containing gold nanorods, where several enhanced features were reported in planar cells, such as a lowering of splay and bend elastic constants, as well as a striking independence on temperature of such parameters [37]. Plasmonic analogues were also shown to be suitable replacements for dichroic dyes in technological applications, due to a greater stability and absence of aggregates [38]. A self-assembly of gold nanorods codoped with nanocomposite materials was also observed in nematic systems, where the orientation of plasmonic nanorods could be fine-tuned to enable the selection of distinct polarized surface plasmon resonance spectra [39]. Albeit liquid-crystalline samples doped with gold nanorods have been extensively explored under parallel planar boundary conditions, a few works were devoted to plasmonic and elastic distortion effects of cells submitted to twist surface anchoring.

In the present work, the effects of a beam impinging at oblique incidence onto a liquid-crystalline system containing gold nanorods at the vicinities of the nematic-smectic-A phase transition are evaluated. Due to optically-induced director reorientations, a nonlinear optical refractive response takes place over thermal effects, being the leading beam distortion phenomena as opposed to the normal incidence configuration [34]. Moreover, an anomalous increase of the nonlinear refractive index n_2 is observed near the vicinities of the nematic-smectic-A phase transition. Such observation is then explained under the light of director instabilities near the phase transition temperature, due to an enhanced anisotropy of Frank elastic constants. As temperatures are lowered and the smectic order becomes well established, a saturable nonlinear absorption is reported, just like at the regime of normal incidence [34], with the nonlinear absorption coefficient β increasing in magnitude as the sample is further cooled, until reaching an apparent plateau.

Moreover, the electro-optical properties of twisted cells containing liquid crystals doped with gold nanorods at two distinct aspect ratios are also exploited. The steady-state transmittances were obtained for several voltages, where samples containing nanoparticles presented a slight decrease in threshold voltages, together with a much steeper profile than the undoped one, with the sample doped with the more elongated particles being the steepest. The time-dependent transmittance curves were also analyzed, and the reorientation time curves for each sample calculated from the data. A significant decrease in reorientation times is reported as impurities are added to the system, with the response being faster in the sample containing the higher aspect ratio nanorods. A thorough discussion is given on the nature of the observed phenomenon, under the light of induced elastic distortions and the Osipov-Terentjev framework. In order to evaluate the contributions of the longitudinal plasmonic extinction band to the enhancement of the electro-optical response, samples were pumped at various powers by a DPSS laser operating at the near infrared, close to the plasmonic peaks. Further, the transmission spectra of cells were obtained for various temperatures, which enabled us to estimate the thermal behavior of the birefringence according to the Gooch-Tarry conditions and Mauguin minima. A reduction in the discontinuity of the birefringence at the nematic-isotropic phase transition was observed, probably due to a decrease in the nematic order parameter caused by the introduction of disorder centers.

2

Lensing phenomena in low absorption thin media

When matter is subject to the presence of radiation at strong intensities, some curious phenomena may occur. For a sample free to move back and forth along the propagation direction of a focused beam (say, over the z-axis), the light irradiance profile over the sample will be dependent on its position, z. This distribution of intensities may interact electro-optically or thermally with our material, causing changes in its index of refraction, n. Such interactions might provoke a radial refractive index profile, $n(r)$, which will be related to the intensity distribution of light, $I(r)$. Depending on how the sample refractive index responds to such intensity profile, a self-focusing or self-defocusing phenomenon of the beam may be observed — due to the lens-like behavior caused by the ensuing refractive index gradient. If we let $z = 0$ be our focus and consider a self-focusing response, a reduction in the transmittance will be observed for $z < 0$, while an increase is measured for $z > 0$. The opposite holds true for a self-defocusing process. Several systems presenting optically-induced refractive index gradients have been previously reported [40, 41, 42], some of which will be discussed in detail here.

When a sample is exposed to electromagnetic radiation, electrons in the material take up the energy of some incident photons, transitioning to a new quantum state, where electromagnetic energy is transformed in internal energy of the sample. Such internal energy increase may lead to thermal variations within the material, possibly altering

macroscopic physical properties, depending on the particular thermal sensitivity of each respective physical parameter. The index of refraction of the sample might be sensitive to slight local variations of temperature, depending on dn/dT, such that an external beam profile impinging the material will ensue a similar temperature profile, and a subsequent refractive index gradient. The aforementioned radial variations on the index of refraction result in a consequent lens-like behavior, called the thermal-lens effect.

Another common phenomenon arises when the beam irradiance is strong enough such that nonlinearities in the electric polarization density become relevant, in a manner that the optical response of the material becomes nonlinear. If we are considering materials possessing inversion symmetry, the nonlinearities are induced through contributions of both real and imaginary components of $\chi^{(3)}$, $\chi^{(5)}$, and further odd polarizability coefficients, $\chi^{(2n+1)}$, with their effects being more or less pronounced according to field strength and material sensitivity. Depending on the laser profile, an index of refraction gradient mimicking the beam profile will be formed in the sample, ensuing a gradient-index lens-like behavior. Such phenomenon is called the optical Kerr effect. A thorough discussion of the aforementioned features is presented later in this chapter.

2.1 Thermal-lens model

When a beam described by some intensity profile is incident upon a sample, the molecules of the material will absorb some of its energy, raising the sample temperature. As a consequence, a thermal profile is observed along the sample, being related to the intensity profile of the impinging beam through the diffusion equation. Such temperature gradient throughout the sample will affect the refractive index, which is sensible to thermal variations, and cause the material to behave like a lens [43, 44, 45]. Such response is called the thermal-lens effect, and a schematic representation of the phenomenon is shown in figure 2.1.

The heat diffusion on the sample on the presence of an energy source term will be

Figure 2.1: Schematic representation of an optically-induced temperature gradient, which, in turn, induces a refractive index distribution throughout the sample, giving rise to a thermally-induced lensing effect. Dashed lines here represent the output light intensity profile in the absence of any material. Solid lines after the sample represent the self-focusing behavior caused by the material properties.
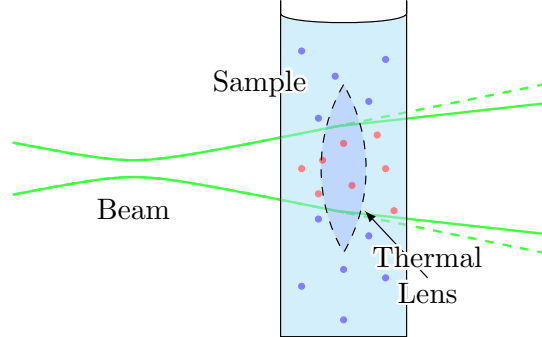
Source: Author (2019).

described by the heat equation, given by [43]

$$c\rho \frac{\partial}{\partial \tau} \left[\Delta T(r, \tau) \right] = \dot{q}(r) + k\nabla^2 \left[\Delta T(r, \tau) \right]. \tag{2.1}$$

Here, $\Delta T(r, \tau)$ is the temperature profile of the sample, induced by a heat source, $\dot{q}(r)$, called the source term. It is the energy flow into a unit volume per unit time at a distance r from the axis. The other constants in the equation together with their units are presented below in table 2.1.

Table 2.1: Parameters appearing in equation (2.1).

c	specific heat	cal g^{-1} K^{-1}
ρ	density	g cm^{-3}
τ	time	s
r	radial coordinate	cm
k	thermal conductivity	cal s^{-1} cm^{-1} K^{-1}

The change in intensity as a light beam passes through a medium presenting a small and linear absorption can be described as

$$\Delta I(r) = I(r) - I_0(r) \approx I_0(r)b\ell_0, \tag{2.2}$$

where b is the sample absorbance, in cm^{-1}, and ℓ_0 is the sample thickness (in cm). $I(r)$ is the light intensity exiting the cell and $I_0(r)$ is the intensity entering the cell. The heat source — corresponding to the energy flow into a unit volume per unit time — will be

the intensity change per unit distance (thickness in this case), defined as

$$\dot{q}(r) = \frac{\Delta I(r)}{\ell_0} \approx I_0(r)b. \qquad (2.3)$$

Since Gaussian beams at TEM_{00} are common experimental lasers and have a function with well-known properties as a profile, we may use them as our beam profile of choice. Such beam will have its radial intensity profile described by

$$I_0(r) = \frac{2(0.24P)}{\pi\omega^2} \exp\left(\frac{-2r^2}{\omega^2}\right). \qquad (2.4)$$

ω here is the beam radius, or spot size, in cm. P is the laser power, in W. The factor of 0.24 is the Joule constant, in order to transform $\text{W} \rightarrow \text{cal s}^{-1}$.

Our source term then will be

$$\dot{q}(r) = \frac{2(0.24P)b}{\pi\omega^2} \exp\left(\frac{-2r^2}{\omega^2}\right). \qquad (2.5)$$

With equation (2.5) as the heat source, the solution to equation (2.1) can be shown by the Green function method to be [46]

$$\Delta T(r,\tau) = \frac{2(0.24P)b}{\pi c\rho\omega^2} \int_0^\tau \left(\frac{1}{1 + 2\tau'/\tau_c}\right) \exp\left(\frac{-2r^2/\omega^2}{1 + 2\tau'/\tau_c}\right) d\tau', \qquad (2.6)$$

where τ_c is defined as

$$\tau_c \equiv \frac{\omega^2 c\rho}{4k}, \qquad (2.7)$$

and is usually called the characteristic time for thermal-lens buildup.

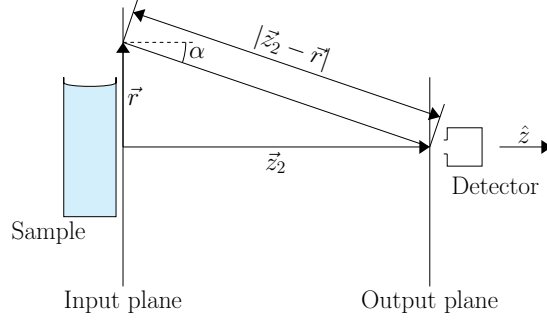On a first approximation, the refractive index as a function of temperature can be written as

$$n(r,\tau) = n_0 + \frac{dn}{dT}\Delta T(r,\tau), \qquad (2.8)$$

where n_0 is the refractive index of the sample at the initial temperature and dn/dT is the ratio of change in the refractive index resulting from temperature variations.

Since we have equation (2.6), the temperature dependence of the refractive index dis-

Figure 2.2: Geometry of the experiment and parameters appearing at the diffraction integral, at equation (2.9).

tribution over the sample can be obtained directly. Such distribution will cause phase distortions on the resulting input beam wave, and in order to calculate this lensing behavior, equation (2.8) will be important later on.

Let us now analyze how the ensuing thermally-induced lens will affect the beam wavefront at the output plane, where the detector is located. The Huygens principle states that the complex phase and amplitude of the resulting wave in the output plane will be the sum of all contributions related to each Huygens wavelets emerging from their respectively source point in the input plane. Mathematically, the Huygens principle can be stated in terms of the diffraction integral,

$$\tilde{U}_{\text{bc}}(\tau) = \frac{i}{\lambda} \int_0^\infty \int_0^{2\pi} \tilde{U}_{\text{i}}(r,\tau) \left(\frac{1 + \cos\alpha}{2} \right) \frac{\exp\left[-i(2\pi/\lambda)|\vec{z}_2 - \vec{r}|\right]}{|\vec{z}_2 - \vec{r}|} r\,dr\,d\phi. \qquad (2.9)$$

Figure 2.2 shows all the parameters used above. The first term in the integrand is the complex phase and amplitude of the wavelets exiting the input plane (that is, right after the sample). The second quantity in the integrand is the inclination factor, and the third is the phase attenuation of a wave after traveling across a distance $|\vec{z}_2 - \vec{r}|$. The result, $\tilde{U}_{\text{bc}}(\tau)$, is the ensuing complex phase and amplitude at the output plane, right on axis $(r = 0)$, where the detector is placed.

In fact, some rearrangements may be done in the experimental setup in order to simplify the diffraction integral. The detector might be placed far away from the sample such as z_2 may be taken as much larger than r, which will lead to $|\vec{z}_2 - \vec{r}| \approx z_2$ and $(1 + \cos\alpha)/2 \approx 1$. For the exponential, a first order approximation is better suited, for

Figure 2.3: Geometry of the optical path differences and phase distribution with thermal-lens sample being absent (a) and present (b).
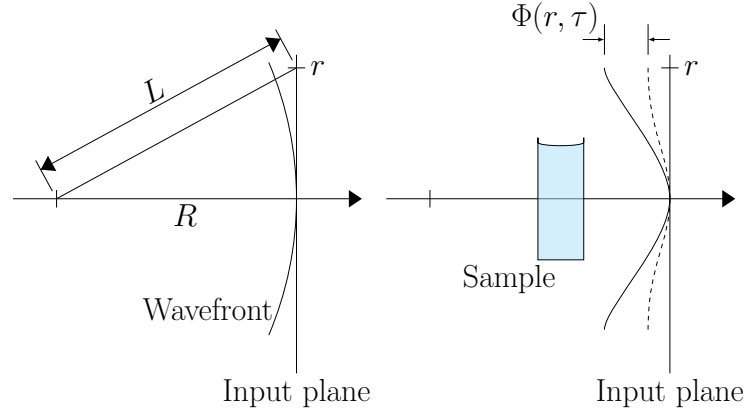
even though the exponent may be small by itself, the exponential of such small value may not be so negligible. Bearing the previous discussion in mind, the argument of the exponential will be better represented by $(2\pi/\lambda)|\vec{z}_2 - \vec{r}| \approx (2\pi/\lambda)[z_2 + r^2/(2z_2)]$. With these previous considerations, equation (2.9) is simplified to

$$\tilde{U}_{\mathrm{bc}}(\tau) = A \int_0^\infty \int_0^{2\pi} \tilde{U}_{\mathrm{i}}(r, \tau) \exp\left(-i\frac{\pi}{\lambda}\frac{r^2}{z_2}\right) r\,dr\,d\phi. \tag{2.10}$$

Here, all constants are merged together into A.

In order to find an expression for $\tilde{U}_{\mathrm{i}}(r, \tau)$, we are going to ignore the effects of the lensing medium and consider a composition of spherical waves of radius R and Gaussian amplitude distribution. Subsequently, the phase distortions caused by the lensing medium will be found and taken into account. Then, the amplitude distributions of the waves exiting the sample will be

$$|\tilde{U}_{\mathrm{i}}(r)| = B \exp\left(\frac{-r^2}{\omega^2}\right). \tag{2.11}$$

The geometry for optical path differences can be used to calculate the phase at points on the input plane. Since optical paths are related to phase differences with a proportionality factor of $2\pi/\lambda$, we may observe the wave geometry represented schematically in figure 2.3 to obtain the phase of each spherical wave. By following the aforementioned

approach, the reckoned phase shifts will be given by

$$\frac{2\pi}{\lambda}L = \frac{2\pi}{\lambda}\sqrt{R^2 + r^2} \tag{2.12}$$

$$\approx \frac{2\pi}{\lambda}\left(R + \frac{r^2}{2R}\right). \tag{2.13}$$

Our approximation is valid, because the beam is confined to a small region around the z-axis, such that $R \gg r$ holds. From equation (2.13), consequently, the relative phase distribution of our spherical waves (also called the phase lag) will be $\pi r^2/\lambda R$.

The effects of the lensing medium may be considered as an aberration in order to take into account the extra phase lag caused by the sample. That means we should add another term to the original phase lag of the spherical wave. Let us once again consider the geometry of optical path lengths. Initially, the optical path is $\Phi_0 = n_0\ell_0$, and the optical path variations for off-axis points about z is written as

$$\Phi(r,\tau) = \ell_0[n(r,\tau) - n(0,\tau)]. \tag{2.14}$$

This is where equation (2.8) becomes important. Knowing our solution, equation (2.6), the additional phase lag will be

$$\frac{2\pi}{\lambda}\Phi(r,\tau) = \frac{2\pi}{\lambda}\frac{dn}{dT}\ell_0[\Delta T(0,\tau) - \Delta T(r,\tau)]. \tag{2.15}$$

Considering we have the following expressions: the amplitude distribution for the waves on the input plane (equation (2.11)), the initial phase lag (equation (2.13)), and the additional phase lag (equation (2.15)), the complex phase and amplitude on the input plane will be

$$\tilde{U}_{\mathrm{i}}(r,\tau) = B\exp\left(\frac{-r^2}{\omega^2}\right)\exp\left[-i\frac{\pi}{\lambda}\left(\frac{r^2}{R} + 2\Phi\right)\right]. \tag{2.16}$$

Substituting equation (2.16) in the diffraction integral (equation (2.10)), performing the change of variables $u = r^2/\omega^2$, and integrating over ϕ, we arrive at

$$\tilde{U}_{\mathrm{bc}}(\tau) = C\int_0^\infty \exp\left\{-\left[u + i\left(\frac{2\pi}{\lambda}\Phi(u,\tau) + \frac{\pi\omega^2}{\lambda}\left(\frac{1}{R} + \frac{1}{z_2}\right)u\right)\right]\right\}du. \tag{2.17}$$

31

Remember that ω here is not the angular frequency of light, but the beam radius. Consequently, since we are considering our beam to be Gaussian, the following relations are true [47]

$$\omega(z_1) = \omega_0 \sqrt{1 + \left(\frac{z_1}{z_R}\right)^2}, \tag{2.18}$$

$$R(z_1) = z_1 \left[1 + \left(\frac{z_R}{z_1}\right)^2\right], \tag{2.19}$$

where z_R (sometimes denoted as z_c) is the Rayleigh range (or confocal parameter) of the Gaussian beam, defined as $z_R = \pi\omega_0^2/\lambda$. Here, ω_0 is the minimum beam waist — that is, the spot size at $z_1 = 0$.

With such relations, the third term in the exponential of equation (2.17) becomes

$$i\frac{\pi\omega^2}{\lambda}\left(\frac{1}{R} + \frac{1}{z_2}\right)u = i\left[\frac{z_1}{z_R} + \frac{z_1}{z_2}\left(\frac{z_1}{z_R} + \frac{z_R}{z_1}\right)\right]u. \tag{2.20}$$

But our detector is placed at the far-field, such that all terms containing z_1/z_2 or z_R/z_2 may be neglected. Furthermore, we will also consider

$$\exp\left(-i\frac{2\pi}{\lambda}\Phi\right) \approx 1 - i\frac{2\pi}{\lambda}\Phi, \tag{2.21}$$

assuming $(2\pi/\lambda)\Phi \ll 1$, a condition usually met in thermal-lens experiments [43]. The diffraction integral is now

$$\tilde{U}_{bc}(\tau) = C\int_0^\infty \left(1 - i\frac{2\pi}{\lambda}\Phi\right)\exp\left[-(1 + i\xi)u\right]du, \tag{2.22}$$

with $\xi = z_1/z_R$.

By finally using our solution (equation (2.6)) to find the additional phase lag (equation (2.15)), we will have

$$\frac{2\pi}{\lambda}\Phi(u,\tau) = \frac{\theta}{\tau_c}\int_0^\tau \eta[1 - \exp\left(-2\eta u\right)]d\tau', \tag{2.23}$$

where

$$\theta = \frac{0.24 P \ell_0}{\lambda} \frac{b}{k} \frac{dn}{dT}, \tag{2.24}$$

$$\eta(\tau') = \frac{1}{1 + 2\tau'/\tau_c}. \tag{2.25}$$

Substituting equation (2.23) in equation (2.22), we are left with

$$\tilde{U}_{bc}(\tau) = C \int_0^\infty \left[1 - i \frac{\theta}{\tau_c} \int_0^\tau \eta[1 - \exp{(-2\eta u)}] d\tau' \right] \exp{[-(1 + i\xi)u]} du. \tag{2.26}$$

Performing first the integral with respect to u and then proceeding to carry out the integrations in τ', we may find a closed expression for $\tilde{U}_{bc}(\tau)$. After integrating equation (2.26), we should now find the intensity measured in our detectors, $I_{bc}(\tau) = |\tilde{U}_{bc}(\tau)|^2$. Such measurable quantity will be

$$I(\tau) = I(0) \left[1 - \frac{\theta}{2} \arctan \left(\frac{2\xi}{3 + \xi^2 + (9 + \xi^2)(\tau_c/2\tau)} \right) \right]^2. \tag{2.27}$$

A common experiment performed to obtain the beam phase shift, θ, directly from curve fitting, is to take the steady-state regime of equation (2.27), where $\tau \to \infty$ and all transient effects die out. In such useful configuration, the measured normalized steady-state transmittance is then

$$T_N(\xi) = \left[1 - \frac{\theta}{2} \arctan \left(\frac{2\xi}{3 + \xi^2} \right) \right]^2, \tag{2.28}$$

where, as we can see, θ is the only free parameter in the transmittance profile.

The fractional intensity change, in turn, will be given by

$$\frac{I(\tau) - I(\infty)}{I(\infty)} = \frac{1 - \theta \arctan \left[\frac{2\xi}{3 + \xi^2 + (9 + \xi^2)(\tau_c/2\tau)} \right]}{1 - \theta \arctan \left(\frac{2\xi}{3 + \xi^2} \right)} - 1, \tag{2.29}$$

if we ignore terms of the order θ^2. Notice that if the sample is positioned at $z_1 = \sqrt{3} z_R$ ($\xi = \sqrt{3}$), we can measure τ_c and, consequently, the thermal diffusivity of our material,

as shown below

$$\frac{I(\tau) - I(\infty)}{I(\infty)} = \frac{1 - \theta \arctan \frac{0.577}{1+\tau_c/\tau}}{1 - \theta(0.524)} - 1. \tag{2.30}$$

Since we have already obtained θ from equation (2.28), a modulated (or chopped) laser beam may be employed to obtain the transient transmitted intensities and measure τ_c — the characteristic thermal lens buildup time — which is the only free parameter in equation (2.30).

2.2   Nonlinear refraction and absorption

Under the presence of electric fields, some materials experience a change in their index of refraction according to the magnitude of the applied field, due to nonlinear contributions to the electric polarizability density. The electric field responsible for triggering such nonlinear response may be due to light itself, where beams with high enough local irradiance provide an ensuing variation of the sample refractive index, causing phase distortions in the incident beam wavefront. Consequently, several phenomena may be observed as beam intensity is boosted, such as self-focusing, self-phase modulation and modulational instability.

Based on the principles of spatial beam distortion, reference [48] presents a single-beam method for measuring the sign and magnitude of refractive nonlinearities that offers simplicity as well as high sensitivity [48, 49], called the Z-scan technique. The proposed experimental setup measures the beam phase distortions caused by lensing media, and the model developed by the authors enables a fast identification of the nonlinear optical response of the sample. In the Z-scan method, a quick analysis of the obtained transmittance profile yields both an immediate identification of the sign of the nonlinear optical parameters β and n_2, as well as a quick estimative for both values.

The experimental apparatus of the Z-scan experiment consists in a Gaussian beam set to be focused at an arbitrary position $z = 0$, where the sample will be moved back and forth along the z-direction. According to the incident beam radius, a different optical response will be obtained, as represented in figure 2.4. The ensuing transmittance will

Figure 2.4: Experimental apparatus of the Z-scan technique, as discussed in main text. Optical components are labeled accordingly in the figure. Here, our diode-pumped solid state laser operating at TEM_{00} will be focused by a lens, and, according to sample positioning, a more or less pronounced thermo- and/or nonlinear optical response will be triggered. Characteristic self-focusing or -defocusing profiles will be observed, where the shape of transmission curves will determine the corresponding main physical mechanisms associated with the phenomena. By the adjust of normalized Z-scan transmittance curves according to the most suitable model, one may obtain beam phase shifts directly for the condition of a closed aperture ($S \approx 0$), which will be related to dn/dT or n_2. For the open aperture configuration ($S = 1$), β follows directly.
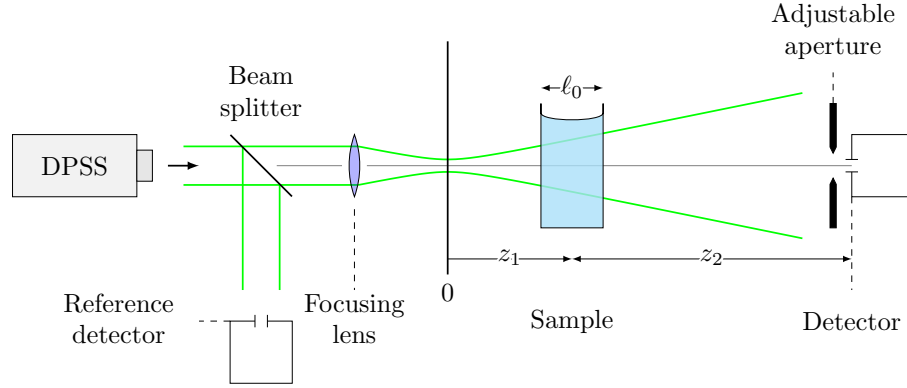
Source: Author (2019).

be recorded by a photodetector after passing a variable aperture tool, such as an iris. Because of this "sweeping" path along the z-axis, the technique was named the Z-scan. In particular, smaller apertures favor the observation of nonlinear refraction effects, while larger apertures become more sensitive to nonlinear absorption effects, to the point of being completely insensitive to n_2 for a fully open configuration, as we shall later see.

As one may notice, for the closed aperture configuration, the experimental setup is identical to the thermal-lens experiment described before. This means that the transmittance profile of the experiment is sensitive to both thermal-lens and nonlinear effects, and one should be careful when inspecting the detected curves. Thermal-lenses, however, present a transmittance profile quite distinct from nonlinear optical effects, because each phenomenon arises from fundamentally different mechanisms. Nevertheless, in most cases, experimental cautions may be assured to filter one effect or the other, and the same apparatus gives insight about phenomena arising from dissimilar principles.

In order to evaluate the behavior of light after traversing a nonlinear medium, let us examine a fast cubic nonlinearity in the refractive index, given by

$$n = n_0 + \frac{n_2}{2}|E|^2 = n_0 + \gamma I, \tag{2.31}$$

35

where n_0 is the linear index of refraction, I is the beam irradiance within the sample (SI), E is the peak electric field (CGS), and n_2 and γ are the nonlinear refractive indices in CGS and SI systems of units, respectively. In particular, $n_2 = (cn_0/40\pi)\gamma$, with c being the speed of light in vacuum (SI). Let us now consider a Gaussian beam in TEM$_{00}$ traveling along the positive z-axis,

$$E(z, r, \tau) = E_0(\tau)\frac{\omega_0}{\omega(z)} \exp\left(-\frac{r^2}{\omega^2(z)} - i\frac{2\pi}{\lambda}\frac{r^2}{2R(z)}\right) \exp\left(-i\Phi(z, \tau)\right). \tag{2.32}$$

As discussed in the previous section, ω is the spot size (or beam radius), ω_0 is the minimum beam waist, and λ is the wavelength — all in free space. $E_0(\tau)$ contains the temporal envelope of the laser pulse, with its peak being the maximum amplitude at focus, and $\exp\left(-i\Phi(z, \tau)\right)$ represents a combination of all the temporal phase variations along z. Here, we will proceed calculating the radial phase variations, $\Delta\Phi(r)$, introduce their contribution to equation (2.32), and find the resulting transmittance for a determined aperture.

Since the thickness of our sample is an experimental parameter of our choice, we may ensure that $\ell_0 < z_\mathrm{R}$ holds. Also, $\ell_0 \ll z_\mathrm{R}/\Delta\Phi(0)$ is a condition shown to hold empirically by [49]. With such conditions in mind, the electric field amplitude ($\sqrt{I}$) and phase (Φ) are governed by the slowly varying envelope approximation [47, 49, 48] as a pair of differential equations,

$$\frac{d\Delta\Phi}{dz'} = \Delta n(I)\frac{2\pi}{\lambda}, \tag{2.33}$$

$$\frac{dI}{dz'} = -\alpha(I)I. \tag{2.34}$$

Here, our variable z' is the penetration depth within the sample, $\Delta n(I)$ is the refractive index variation caused by the laser beam, and $\alpha(I)$ is a term containing all absorptive contributions. For a cubic nonlinearity in the refractive index (no $\chi^{(5)}$ or higher order effects) and negligible nonlinear absorption ($\beta \approx 0$), our set of equations may be directly solved to yield

$$\Delta\Phi(z, r, \tau) = \frac{\Delta\Phi_0(\tau)}{1 + z^2/z_\mathrm{R}^2} \exp\left(-\frac{2r^2}{\omega^2(z)}\right). \tag{2.35}$$

$\Delta\Phi_0(\tau)$ here is the phase shift at the focus over the z-axis, defined as

$$\Delta\Phi_0(\tau) = \frac{2\pi}{\lambda}\gamma I_0(\tau)L_{\text{eff}}, \tag{2.36}$$

with $I_0(\tau)$ being the beam irradiance at the focus and $L_{\text{eff}} = [1 - \exp(-\alpha\ell_0)]/\alpha$ the effective length of the sample, with α being the linear absorption coefficient.

The electric field exiting the sample now will have a difference in amplitude and phase, due to linear absorption and the phase shift just found at equation (2.35), which will be

$$E_{\text{e}}(z, r, \tau) = E(z, r, \tau)\exp\left(-\frac{\alpha}{2}\ell_0\right)\exp\left[i\Delta\Phi(z, r, \tau)\right]. \tag{2.37}$$

We will now proceed using the Gaussian decomposition of beams, in which the complex electric field at the input plane is decomposed in a series of Gaussian beams through a Taylor series expansion of $\exp[-i\Delta\Phi(z, r, \tau)]$, the complex phase term [50]. Our series expansion will be

$$\exp\left[-i\Delta\Phi(z, r, \tau)\right] = \sum_{m=0}^{\infty}\frac{[i\Delta\Phi_0(z, \tau)]^m}{m!}\exp\left(\frac{-2mr^2}{\omega^2(z)}\right). \tag{2.38}$$

Each Gaussian beam is assumed to propagate through space to the output plane, where they are combined to reconstruct the resulting beam. The electric field at the aperture (output plane) is then represented by [49, 48]

$$E_{\text{a}}(r, \tau) = E(z, r = 0, \tau)\exp\left(-\frac{\alpha}{2}\ell_0\right)\sum_{m=0}^{\infty}\frac{[i\Delta\Phi_0(z, \tau)]^m}{m!}\frac{\omega_{0m}}{\omega_m}\exp\left(-\frac{r^2}{\omega_m^2} - \frac{i\pi r^2}{\lambda R_m} + i\theta_m\right). \tag{2.39}$$

If our detector is placed at $z = z_2$ and we define $g = 1 + z_2/R(z)$, the yet undefined parameters in equation (2.39) are

$$\omega_{0m} = \frac{\omega^2(z)}{2m + 1}, \tag{2.40}$$

$$z_{2m} = \frac{\pi\omega_{0m}^2}{\lambda}, \tag{2.41}$$

$$\omega_m^2 = \omega_{0m}^2\left[g^2 + \frac{z_2^2}{z_{2m}^2}\right], \tag{2.42}$$

$$R_m = z_2 \left[1 - \frac{g}{g^2 + z_2^2/z_{2m}^2} \right]^{-1}, \qquad (2.43)$$

$$\theta_m = \arctan \left(\frac{z_2/z_{2m}}{g} \right). \qquad (2.44)$$

The transmitted power through the aperture can be found by integrating the electric field throughout the aperture radius. That is,

$$P_T(\Delta\Phi_0(\tau)) = c\epsilon_0 n_0 \pi \int_0^{r_a} |E_a(r,\tau)|^2 r\,dr, \qquad (2.45)$$

where ϵ_0 is the electrical permittivity in vacuum. The normalized Z-scan transmittance is then

$$T_N(z) = \frac{\int_{-\infty}^{\infty} P_T(\Delta\Phi_0(\tau))d\tau}{S \int_{-\infty}^{\infty} P_i(\tau)d\tau}. \qquad (2.46)$$

Here, $P_i(\tau) = \pi\omega_0^2 I_0(\tau)/2$ is the beam power penetrating the sample at τ, and $S = 1 - \exp\left(-2r_a^2/\omega_a^2\right)$ is the aperture transmittance when the linear regime is considered, with ω_a being the beam radius at the aperture.

For a closed aperture and $\xi = z/z_R$, by considering the two leading terms of the expansion equation (2.39), the steady-state transmittance will be given by [49]

$$T_N(\xi) = 1 - \frac{4\Delta\Phi_0\xi}{(\xi^2 + 9)(\xi^2 + 1)}. \qquad (2.47)$$

Even though equation (2.47) is a powerful tool to measure nonlinear optical refraction in thin samples, it does not, however, take into account effects related to nonlinear optical absorption in the ensuing transmittance. Some materials present a strong resonant transition of energy levels which may be associated with two recurring phenomena, in particular: either a fast rate excitation preventing electrons to decay back to ground state before it becomes depleted; or the population of a new excited level, accessed by the electrons through the absorption of the energy of multiple photons.

For instance, let us take a closer look at $\chi^{(3)}$ nonlinearities, considering the third-order

nonlinear susceptibility as a complex quantity,

$$\chi^{(3)} = \chi^{(3)}_{\text{Re}} + i\chi^{(3)}_{\text{Im}}, \tag{2.48}$$

where $\chi^{(3)}_{\text{Re}}$ and $\chi^{(3)}_{\text{Im}}$ are the real and imaginary components of $\chi^{(3)}$, respectively. The real part of the nonlinear susceptibility is related to γ (or n_2) as follows

$$\chi^{(3)}_{\text{Re}} = 2n_0^2\epsilon_0 c\gamma, \tag{2.49}$$

while the imaginary component is related to the nonlinear absorption coefficient (β) as

$$\chi^{(3)}_{\text{Im}} = \frac{n_0^2\epsilon_0 c\lambda}{2\pi}\beta. \tag{2.50}$$

Our initial set of differential equations — equation (2.33) and equation (2.34) — will now be rewritten to take into account the effects of nonlinear absorption. That is, $\alpha(I) = \alpha + \beta I$. Once again, by direct integration, the exiting beam irradiance at the input plane will be

$$I_e(z, r, \tau) = \frac{I(z, r, \tau)\exp(-\alpha\ell_0)}{1 + \beta L_{\text{eff}}I(z, r, \tau)}, \tag{2.51}$$

while the beam phase shift is

$$\Delta\phi(z, r, \tau) = \frac{2\pi}{\lambda}\frac{\gamma}{\beta}\ln[1 + \beta L_{\text{eff}}I(z, r, \tau)]. \tag{2.52}$$

Consequently, the complex electric field at the input plane is

$$E_e(z, r, \tau) = \sqrt{I_e(z, r, \tau)}\exp(i\Delta\phi), \tag{2.53}$$

$$= E(z, r, \tau)\exp\left(-\frac{\alpha}{2}\ell_0\right)[1 + \beta L_{\text{eff}}I(z, r, \tau)]^{i2\pi\gamma/(\lambda\beta)-1/2}. \tag{2.54}$$

Let us call $q(z, r, \tau) = 1 + \beta L_{\text{eff}}I(z, r, \tau)$. If $|q(z, r, \tau)| < 1$, following a binomial series expansion in powers of $q(z, r, \tau)$, equation (2.54) can be written as a Gaussian

decomposition as follows

$$E_{\mathrm{e}}(z,r,\tau) = E(z,r,\tau) \exp\left(-\frac{\alpha}{2}\ell_0\right) \sum_{m=0}^{\infty} \frac{q(z,r,\tau)^m}{m!} \left[\prod_{n=0}^{m}\left(\frac{i2\pi\gamma}{\lambda\beta} - \frac{1}{2} - n + 1\right)\right]. \quad (2.55)$$

where the binomial coefficient has been defined in terms of the product, Π. By factoring out $i4\pi\gamma/(\lambda\beta)$, equation (2.55) can be represented analogously to equation (2.39), by making the following substitution:

$$\frac{[i\Delta\phi_0(z,\tau)]^m}{m!} \to f_m = \frac{[\Delta\phi_0(z,\tau)]^m}{m!} \prod_{n=0}^{m}\left[1 + \frac{\lambda\beta}{4\pi\gamma}(2n-1)\right]. \quad (2.56)$$

Note how the coupling factor here, $\lambda\beta/(4\pi\gamma)$, is the ratio $\chi_{\mathrm{Im}}^{(3)}/\chi_{\mathrm{Re}}^{(3)}$, indicating that nonlinearities in the refractive index and nonlinearities in the absorption coefficient are coupled together.

If we consider the open aperture configuration, however, the Z-scan experiment becomes insensitive to n_2 effects, as predicted by equation (2.46). Beam distortions become irrelevant to overall measurements and only nonlinear absorption effects take place. We can now proceed integrating equation (2.51) in the open aperture configuration ($S = 1$) with respect to r to obtain the transmitted power

$$P(z,\tau) = P_{\mathrm{i}}(\tau) \exp\left(-\alpha\ell_0\right) \frac{\ln\left[1 + q_0(z,\tau)\right]}{q_0(z,\tau)}. \quad (2.57)$$

Here, $q_0(z,\tau) = \beta I_0(\tau)L_{\mathrm{eff}}/(1 + z/z_{\mathrm{R}}^2)$ and $P_{\mathrm{i}}(\tau) = \pi\omega_0^2 I_0(\tau)/2$ is the instantaneous input power within the sample, as defined before. If we consider our incident beam to be a temporally Gaussian pulse, the measured power can be integrated with respect to time to yield the measured transmittance

$$T_{\mathrm{N}}(z)_{S=1} = \frac{1}{\sqrt{\pi}q_0(z,0)} \int_{-\infty}^{\infty} \ln\left[1 + q_0(z,0)\exp\left(-\tau'^2\right)\right]d\tau'. \quad (2.58)$$

Once again, if $|q_0(z,0)| < 1$, we can take advantage of the identities

$$\ln[1 + a\exp(-x^2)] = -\sum_{m=1}^{\infty} \frac{(-1)^m [a\exp(-x^2)]^m}{m} \qquad (2.59)$$

and

$$\int_{-\infty}^{\infty} [\exp(-x^2)]^m dx = \frac{\sqrt{\pi}}{\sqrt{m}} \qquad (2.60)$$

to express equation (2.58) in a more convenient summation form,

$$T_N(z)_{S=1} = \sum_{m=0}^{\infty} \frac{[-q_0(z,0)]^m}{(m+1)^{3/2}}. \qquad (2.61)$$

Equation (2.61) can be used as an expression to the normalized Z-scan transmittance for the open aperture configuration to determine β alone, since at $S = 1$ the transmittance curves are insensitive to beam distortion effects. When β is determined, $\chi_{\text{Im}}^{(3)}$ is known, and the coupling factor can be reckoned by any $S < 1$ Z-scan experiment. This leads us to a determined value for $\chi_{\text{Re}}^{(3)}$ and, consequently, n_2. Higher order effects such as $\chi^{(5)}$ contributions can also be calculated by the Sheik-Bahae method: the further nonlinearities just have to be considered on equations (2.33) and (2.34). Consequently, different expressions would be obtained for equations (2.51) and (2.52), but the Gaussian decomposition method, equation (2.55), will still hold. For the purpose of this work, we will limit ourselves to $\chi^{(3)}$ nonlinearities, and state that the equivalent $\chi^{(5)}$ normalized Z-scan transmittance will show a valley-peak separation of $\Delta_{\text{v−p}} \approx 1.2$, and $\Delta T_{\text{v−p}} \approx 0.21|\Delta\Phi_0|$ for the closed aperture ($S \rightarrow 0$) configuration [49].

2.3 Director reorientation-induced nonlinear refraction

Since the liquid crystal director is extremely sensitive to external electric fields, amplitudes as low as light's electric field may reorient the director and give rise to a change in the extraordinary refractive index. Such refractive index depends on the director ori-

entation according to the following equation [51, 52]

$$n_{\rm e}(\theta) = \frac{n_\parallel n_\perp}{\sqrt{n_\parallel^2 \cos^2\theta + n_\perp^2 \sin^2\theta}}, \tag{2.62}$$

where θ is the angle formed by the perpendicular axis of the molecules and the far-field director.

In order to avoid director reorientations, samples are prepared with specific boundary conditions to keep the director uniform throughout the bulk and parallel or perpendicular to the incident wave vector. This approach avoids dealing with LC birefringence, since light will only be interacting with one of the refractive indices. If one exits the aforementioned regime, either by introducing an external field or by letting light impinge the sample with a certain oblique incidence angle, an electrical or optical birefringence may be induced.

As we shall later see, the theory of continuum dictates the behavior of the director according to the minimization of Helmholtz free energy, where splay, bend, twist and electric field-induced distortions will be taken into account. For a fixed temperature, the free energy densities associated with such deformations of the director will be [1]

$$f_{\rm splay} = \frac{1}{2}K_{11}(\nabla \cdot \vec{n})^2, \tag{2.63}$$

$$f_{\rm twist} = \frac{1}{2}K_{22}(\vec{n} \cdot \nabla \times \vec{n})^2, \text{ and} \tag{2.64}$$

$$f_{\rm bend} = \frac{1}{2}K_{33}(\vec{n} \times \nabla \times \vec{n})^2. \tag{2.65}$$

Here, K_{11}, K_{22}, and K_{33} are the splay, twist and bend elastic constants of the liquid crystal.

If we consider a beam impinging our sample obliquely, as shown in figure 2.5, a dipole interaction will be observed between the dielectric anisotropy of the molecules and the electric field of light. The free energy density associated with such interaction is written as [52]

$$f_{\rm op} = -\frac{1}{4\pi}\int \vec{D} \cdot d\vec{E} = -\frac{\epsilon_\perp}{8\pi}E^2 - \frac{\Delta\epsilon\langle(\vec{n} \cdot \vec{E})^2\rangle}{8\pi}, \tag{2.66}$$

Figure 2.5: Director reorientation brought about by the electric field of light, ensuing an optically-induced birefringence and consequent nonlinear refraction.
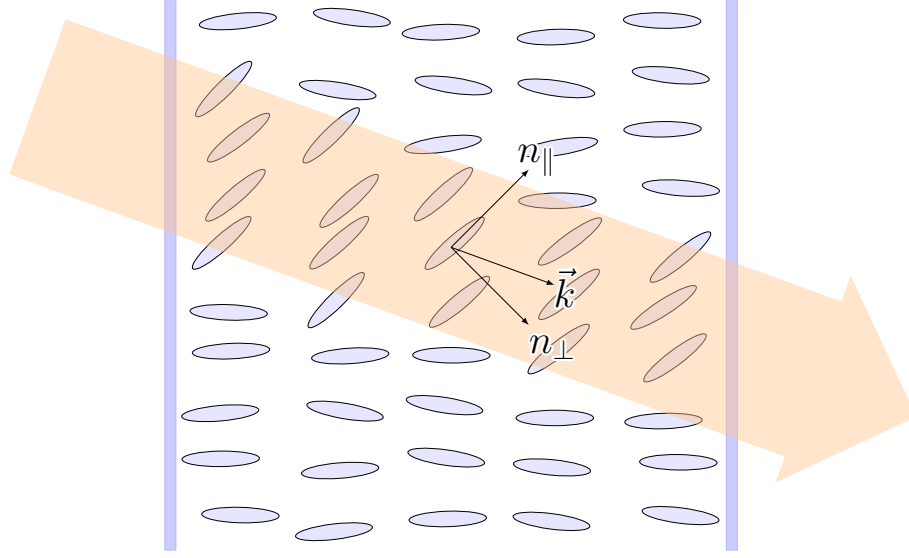
Source: Author (2019).

where $\langle(\vec{n} \cdot \vec{E})^2\rangle$ here represents the time average. Since we will be minimizing the energy density with respect to variations in the director profile, the first term will play no role in the minimization. So we can consider

$$f_{\text{op}} = -\Delta\epsilon_{\text{op}}E_{\text{op}}^2, \tag{2.67}$$

where $E_{\text{op}}^2 = \langle(\vec{n} \cdot \vec{E})^2\rangle/8\pi$. The total energy density of our system, F, will be the sum of every possible deformation plus the energy associated with the dipole-field interaction, which is

$$F = f_{\text{splay}} + f_{\text{twist}} + f_{\text{bend}} + f_{\text{op}}. \tag{2.68}$$

The surface anchoring energy will not appear in the Hamiltonian, and will instead be taken as boundary conditions for our differential equations.

For a homeotropic nematic cell under the influence of the optical electric field, f_{twist} will be null, since there won't be any twist deformations in our system. The director profile may be obtained by solving the Euler equation associated with the Hamiltonian described in equation (2.68). Such equation will be the torque balance of the molecules

in the presence of viscosity and an external optical field, which is [51, 52]

$$I\frac{d^2\theta}{dt^2} + \gamma_1\frac{d\theta}{dt} = (K_{11}\sin^2\theta + K_{33}\cos^2\theta)\frac{d^2\theta}{dz^2} + [(K_{11} - K_{33})\sin\theta\cos\theta]\left(\frac{d\theta}{dz}\right)^2 +$$
$$+ [\alpha_2\sin^2\theta - \alpha_3\cos^2\theta]\frac{d\nu}{dz} + \epsilon_0\Delta\epsilon_{\mathrm{op}}E_{\mathrm{op}}^2 f(\beta,\theta). \quad (2.69)$$

The first term on the left hand side of our equation represents the total torque of the system, where is I the moment of inertia of the molecules. The second term on the same side represents the linear damping related to the angular momentum of molecules — which will be proportional to the constant γ_1, called the rotational viscosity. On the right hand side, the first and second terms come from the splay and bend elastic distortions of the liquid crystal. The third term represents the damping associated with the linear flow of molecules — where α_2 and α_3 are called the Leslie coefficients and ν the velocity of the nematic flow. The last term on the right hand side represents the electric field drive caused by incident light — where $\Delta\epsilon_{\mathrm{op}}$ is the dielectric anisotropy of the material at an optical frequency and $f(\beta,\theta)$ will be a function dependent on the incidence of the wave in the sample.

If we consider a plane wave impinging our homeotropically-aligned cell at a certain angle β; within the one constant approximation, where $K_{11} = K_{33} = K$; neglect any nematic flow; and the torque being null; we will be left with the much simplified equation

$$\gamma_1\frac{d\theta}{dt} = K\frac{d^2\theta}{dz^2} + \epsilon_0\Delta\epsilon_{\mathrm{op}}E_{\mathrm{op}}^2\sin[2(\beta + \theta)]. \quad (2.70)$$

In the limit where local director reorientations are smaller than the incidence angle, one has $\beta + \theta \approx \beta$. If we also consider the steady-state only, $d\theta/dt$ eventually dies out. So,

$$K\frac{d^2\theta}{dz^2} + \epsilon_0\Delta\epsilon_{\mathrm{op}}E_{\mathrm{op}}^2\sin(2\beta) = 0. \quad (2.71)$$

Equation (2.71) can be solved straightforwardly to give

$$\theta(z) = \frac{-\epsilon_0\Delta\epsilon_{\mathrm{op}}E_{\mathrm{op}}^2\sin(2\beta)}{2K}z^2 + Az + B. \quad (2.72)$$

Remembering our boundary conditions, our cell is homeotropically-aligned, so $\theta = 0$ for $z = 0$ and $z = \ell_0$, such that

$$B = 0, \tag{2.73}$$

$$A = \frac{\epsilon_0 \Delta\epsilon_{\mathrm{op}} E_{\mathrm{op}}^2 \sin{(2\beta)}\ell_0}{2K}. \tag{2.74}$$

Consequently, θ will be given by

$$\theta(z) = \frac{\epsilon_0 \Delta\epsilon_{\mathrm{op}} E_{\mathrm{op}}^2 \sin{(2\beta)}}{2K}(z\ell_0 - z^2). \tag{2.75}$$

Since the director will vary along the sample thickness throughout the laser path, the material will exhibit a z-dependent extraordinary refractive index change, given by

$$\Delta n_{\mathrm{e,opt}}(z) = n_{\mathrm{e}}(\beta + \theta(z)) - n_{\mathrm{e}}(\beta) = \frac{n_\perp \Delta\epsilon_{\mathrm{op}}}{\varepsilon_\| n_\|}\theta(z)\sin{(2\beta)} = \alpha_2(z)I, \tag{2.76}$$

where $\alpha_2(z)$ is the optical nonlinearity, and I is the optical intensity. In particular, $I = n_\| E_{\mathrm{op}}^2/2\eta$, where η is the free space impedance. By using equations (2.75) and (2.76), the optical nonlinearity will be approximately

$$\alpha_2(z) \approx \frac{n_\perp \Delta\epsilon_{\mathrm{op}}^2 \eta\epsilon_0}{\varepsilon_\| n_\|^2 K}\sin^2{(2\beta)}(z\ell_0 - z^2). \tag{2.77}$$

The nonlinear refraction index, in turn, will be the average of optical nonlinearities along the sample. That is,

$$n_2 = \langle\alpha_2\rangle \approx \frac{n_\perp \Delta\epsilon_{\mathrm{op}}^2}{6\varepsilon_\| n_\|^2 cK}\ell_0^2 \sin^2{(2\beta)} \tag{2.78}$$

or

$$n_2 = \frac{\Delta\epsilon_{\mathrm{op}}^2 \ell_0^2}{24cK_{11}}\sin^2{(2\beta)}. \tag{2.79}$$

Equation (2.79) dictates the behavior of the nonlinear refractive index according to the elastic and dielectric properties of our liquid crystal. By doping liquid crystal sam-

ples with dye molecules, fullerene, or plasmonic nanoparticles, it has been reported that the nonlinear optical response of guest-host liquid crystalline systems may be enhanced by several orders of magnitude compared to undoped samples [51]. In particular, an enhancement in the optically-controlled birefringence response is desired due to its simplicity and advantages over electrically-controlled systems, such as remote access, needlessness of electronic circuits, and fine-tuning possibilities arising from the complete control of both incidence direction and polarization of the incident optical electric field [53, 51, 52].

2.4   Z-Scan technique

The Z-scan technique is a powerful tool for measuring nonlinear refraction and absorption in materials, as well as effects related to the formation of thermal lenses. While other methods are also well-established and accurate, such as nonlinear interferometry, degenerate four-wave mixing, nearly degenerate three-wave mixing, ellipse rotation, and beam distortion measurements, they either require a complex experimental apparatus or require precise scans followed by a detailed wave-propagation analysis. By using an experimental apparatus as simple as described in figure 2.4, nonlinear and thermo-optical effects can be exhaustively examined.

The experimental setup is indeed simple: it only needs to consist of a single Gaussian beam focused by a lens, where the sample will be moved around the focus, and the output then captured by a photodetector. The presence of an iris or convergent lens before the detector is also required: to either filter information to points near the z-axis only ($r = 0$) or gather information about the whole output plane ($0 \leq r < \infty$).

When interacting with our samples, laser beams may trigger refractive (or absorptive) index changes, which in turn make the sample act like a lens and distort the incident beam itself. If the refractive index gradient induced in the sample yields a convergent lens, for instance, the lens will try to further converge the beam for points at $z < 0$, shortening the beam focus and decreasing the received power captured by the detector in the closed aperture configuration. For points where $z > 0$, the convergent lens will tend to collimate the diverging photons, leading to an increase of the detected power at ($r = 0$).

The opposite will be hold true for refractive index gradients that induce divergent lenses.

As one sweeps the sample along the z-axis around $z = 0$, the detected intensities will form a characteristic profile holding information about the beam phase shift according to sample positioning. Furthermore, different phenomena lead to different profiles, and the Z-scan technique will be able to tell if the lensing effects originate from thermally-induced refractive index changes or nonlinearities in the index of refraction.

In the previous sections, we have seen two different phenomena that give rise to self-focusing and self-defocusing lensing effects, one associated with thermal diffusion (equation (2.28)) and other with nonlinearities in the refractive index (equation (2.47)) — the thermal-lens and Sheik-Bahae models, respectively. The Z-scan experiment is sensitive to both, and cannot explicitly filter beam phase distortions caused by one from the other. If we take a look at the mathematical expressions for the thermal-lens model (which will be called TL) and the Sheik-Bahae model (SB), however, we may notice that even though both curves will present a maximum-minimum profile for negative (divergent) lenses and minimum-maximum profile for positive (convergent) lenses, they are rather distinct. One way to distinguish which is the leading mechanisms behind the observed lensing phenomenon is to examine the extrema separation (valley-peak separation, or $\Delta_{\mathrm{vp}} \equiv |\xi_{\mathrm{v}} - \xi_{\mathrm{p}}|$) of the transmission curve.

Consider first the normalized Z-scan transmittance for a thermally-induced refractive index change (dn/dT effect). The TL model states that

$$T_{\mathrm{N}}^{(\mathrm{TL})}(\xi) = \left[1 - \frac{\theta}{2} \arctan\left(\frac{2\xi}{3 + \xi^2} \right) \right]^2. \tag{2.80}$$

Note that the extrema in such case will be slightly dependent on θ. If we, however, neglect small contributions of the order of θ^2, our extrema will be given by $\xi_{\mathrm{vp}} = \pm\sqrt{3}$, leading to a valley-peak separation of $\Delta_{\mathrm{vp}} \approx 3.46$.

If we consider a fast cubic nonlinearity in the refractive index (a n_2 effect) without any nonlinear absorption taking place ($\Im(\chi^{(3)}) = 0$), the normalized Z-scan transmittance in

Figure 2.6: Comparison between the transmission profile obtained by a pure dn/dT effect in the thermal-lens model (left) and pure n_2 effect in the Sheik-Bahae model (right). As one can see, the valley-peak separation is distinct for each phenomenon, and the transmittance profiles exhibit remarkably different shapes, with the Sheik-Bahae normalized transmittance being much steeper.
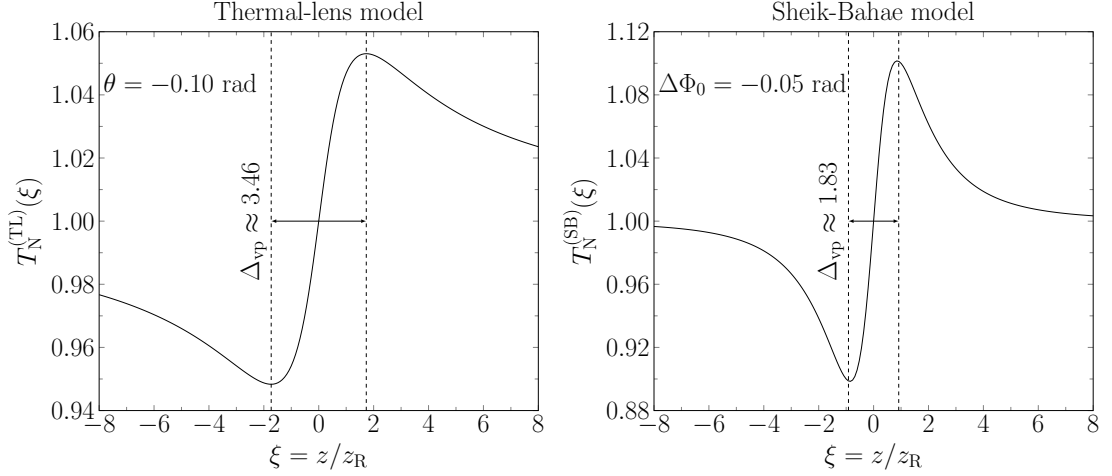
Source: Author (2019).

the Sheik-Bahae model will be

$$T_N^{(SB)}(\xi) = 1 - \frac{4\Delta\Phi_0\xi}{(\xi^2+9)(\xi^2+1)}. \tag{2.81}$$

This time, the extrema will not be dependent on any parameters, but ξ itself, and although the derivative of equation (2.81) has two non-real roots, it has two symmetric real roots at $\pm(2\sqrt{15}-5)/3$, ensuing a transmittance peak-valley separation of $\Delta_{vp} \approx 1.83$.

In order to illustrate how not only the valley-peak separations are distinct in each case, but how each phenomena yields fundamentally different curves, a plot of both models is represented in figure 2.6.

Equivalently, we can make the same analysis for a nonlinear optical absorption. If, instead of using an iris, one switches to a convergent lens to capture the overall signal of the resulting beam, the resulting curve becomes insensitive to nonlinearities in the refractive index, but sensible to nonlinear absorption. Consequently, β effects become evident. When moving a sample from negative z towards 0, the incident intensity will increase as ω decreases, which may lead to a hindered transmittance as the incident intensity is boosted (enhancement of absorption, $\beta > 0$) or to a reduction of the ensuing transmittance as the incident intensity grows (decrease of absorption, $\beta < 0$). The former

effect is called multiphoton absorption, where samples have their electrons excited to an energy level higher than linear absorption in order to deal with significant I^2 irradiance. The latter effect is called single photon saturation, happening when electrons at the ground state become excited at such a rate that there is no sufficient time for a decay before the ground state becomes depleted. Consequently, the system can hold no more excited states, and an increase the resulting transmittance is observed as a consequence. As samples move farther away from the focus, the incident light intensity is diminished, and the normalized transmittance returns symmetrically to unity.

A practical expression for the normalized Z-scan transmittance for a fully open aperture can be obtained by considering the first two terms in equation (2.61), namely,

$$T_{\mathrm{N}}^{(\mathrm{SB})}(\xi)_{S=1} \approx 1 - \frac{\beta I_0 L_{\mathrm{eff}}}{\sqrt{8}(1+\xi^2)}. \tag{2.82}$$

Such expression yields β directly from the transmittance curves, and the nonlinear refraction coefficient may be obtained by adjusting the normalized Z-scan transmittance for a predetermined finite aperture ($S < 1$), when both effects are considered. The predicted transmittance for this experiment, however, is obtained by radially integrating equation (2.51) over a predetermined finite aperture ($S < 1$), and may be impractical for quick analyses. With that in mind, it is useful to derive a way to quickly perform β and n_2 estimates.

For instance, one may follow a simple approach if $|q_0(0,0)| \leq 1$ and $\chi_{\mathrm{Im}}^{(3)} \leq \chi_{\mathrm{Re}}^{(3)}$. The first condition may be met by choosing appropriate incident beam powers, while the second will unfortunately be dependent on the physical properties of the sample, but is shown to hold for a wide variety of materials [49]. The process consists of dividing the measured closed aperture normalized Z-scan transmittance curve ($S < 1$) by the equivalent open aperture one ($S = 1$). The result will be a new Z-scan curve, where estimated values for the nonlinearity in the refractive index may be calculated by the valley-peak vertical separation $\Delta T_{\mathrm{vp}} \approx 0.406|\Delta\Phi_0|$, just like the estimates for a very small aperture ($S \to 0$) [49].

3

Electro-optical properties of twisted nematics

As we have seen in previous chapters, liquid crystalline materials may present changes in their optical properties due to interactions with the electric field of light itself. For instance, nonlinear optical absorption and refraction phenomena were shown to be considerable when matter interacts with beams presenting strong irradiance. Furthermore, an optically-induced birefringence emerges in homeotropic nematic samples under the regime of oblique light incidence, due to a reorientation of the director caused by the electric field of the incident beam.

The sources of changes in optical properties, however, are not exclusively restricted to the electric field of light. External slowly varying voltages (compared to the frequency of light) applied to cell plates may as well yield significant modifications in the optical response of samples, called electro-optical effects. One of the main mechanisms behind such alterations is the reorientation of the director — commonly known as the Freedericksz transition — and the consequent reorientation of the axis of anisotropy, influencing the phase, polarization, and amplitude of light. Electro-optical effects are of extreme importance, both because fundamental viscoelastic and dielectric properties may be obtained from simple optical experiments, and for their usefulness in technological applications.

This chapter is dedicated to the analysis of the interplay between electronically-applied external electric fields and the ensuing director configuration within twisted nematic samples, under the light of free energy minimization. At first, the steady-state director profile of samples undergone a Freedericksz transition is calculated, as well as how elastic and

dielectric constants determine the transition threshold voltage. At next, the dynamics of the Freedericksz transition is examined, and by which means the viscoelastic properties of liquid crystals will influence the director reorientation times. Further, linear optical transmission through twisted cells is evaluated, by the means of stratifying our media in layers. At last, the mechanisms connecting the microscopic anisotropy of molecules and the macroscopic birefringent nature of liquid crystals is discussed.

3.1   Freedericksz transition in twisted nematics

Twisted nematic liquid crystal cells have proven to be effective devices for switchable displays, since the experimental discovery of the transmission of light when a twist cell is placed between crossed polarizers (by Mauguin, in 1911), and the consequent development of a practical way to reorient the director and hinder such transmission — "switching the display off" — by Helfrich and Schadt, sixty years later [54, 55]. To understand the mechanisms behind the operation of twisted nematic displays (TN-LCD), it is important to comprehend the interplay between the viscoelastic constants and the director configuration. Such interactions can be clearly understood through a detailed analysis of the Freedericksz transition and how the ensuing director profile will affect the sample birefringence and following optical transmission. In the present chapter, we will part from Ericksen-Leslie coupled equations for the steady-state and arrive at the ensuing director configuration for an applied arbitrary external field, H, together with the critical values that make reorientation start to occur.

By considering a set of right-handed Cartesian coordinates, the director characterized as an unit vector, and the influence of an external field along the z-direction (perpendicular to the glass substrates), the steady-state reorientation will be given by two coupled differential equations [56],

$$f(\theta)\frac{d^2\theta}{dz^2} + \frac{1}{2}\left[\frac{d}{d\theta}f(\theta)\right]\left(\frac{d\theta}{dz}\right)^2 - \frac{1}{2}\left[\frac{d}{d\theta}g(\theta)\right]\left(\frac{d\varphi}{dz}\right)^2 -$$
$$- 2\alpha_2\tau\sin\theta\cos\theta\frac{d\varphi}{dz} + \nu H^2\sin\theta\cos\theta = 0 \qquad (3.1)$$

and

$$g(\theta)\frac{d^2\varphi}{dz^2} + \left[\frac{d}{d\theta}g(\theta)\right]\frac{d\theta}{dz}\frac{d\varphi}{dz} + 2\alpha_2\tau\sin\theta\cos\theta\frac{d\theta}{dz} = 0, \qquad (3.2)$$

where

$$f(\theta) = \alpha_1\cos^2\theta + \alpha_3\sin^2\theta, \qquad (3.3)$$

$$g(\theta) = (\alpha_2\cos^2\theta + \alpha_3\sin^2\theta)\cos^2\theta. \qquad (3.4)$$

Here, $\theta(z)$ and $\phi(z)$ are the polar and azimuthal angle of the director at position z, respectively. H is an arbitrary external field, together with a multiplicative constant ν (which may be, for example, $\Delta\epsilon$ and E), and α_i are the elastic constants of our liquid crystal. τ here is the auxiliary constant used in [57] and [58] (but labeled as s_0 in the references). Equation (3.2) can be integrated to

$$g(\theta)\frac{d\varphi}{dz} - \alpha_2\tau\cos^2\theta = C_1, \qquad (3.5)$$

with C_1 being an arbitrary constant to be determined from boundary conditions.

Multiplying equation (3.1) by the derivative of θ with respect to z, equation (3.2) by $d\varphi/dz$, summing both, and integrating, we will have

$$f(\theta)\left(\frac{d\theta}{dz}\right)^2 + g(\theta)\left(\frac{d\varphi}{dz}\right)^2 + \nu H^2\sin^2\theta = C_2. \qquad (3.6)$$

The stored energy per unit volume in a liquid crystal, W, is assumed to be a function of $\vec{n}$ and $\nabla\vec{n}$. Such function is objective to proper rigid rotations and invariant under the transformation $\vec{h} \to -\vec{h}$. If W is also invariant under reflections in planes containing the director, $\vec{n}$, we have what is called a nematic liquid crystal [59]. In such liquid crystals, consequently, W is invariant under improper orthogonal transformations, and the substitution $\vec{h} \to -\vec{h}$ in the free energy formulae leads to $\tau = 0$ [57, 58, 56].

Let us also consider initially no external field to find a homogeneous solution, and then later treat the field as a inhomogeneity in our coupled ordinary differential equations, to

find a particular solution. So, for the set

$$f(\theta)\left(\frac{d\theta}{dz}\right)^2 + g(\theta)\left(\frac{d\varphi}{dz}\right)^2 = C_2 \tag{3.7}$$

and

$$g(\theta)\frac{d\varphi}{dz} = C_1, \tag{3.8}$$

we may suppose a solution intuitively, by assuming that θ will not vary throughout the sample. Its value is already zero at both surfaces, due to anchoring $(\theta(0) = \theta(\ell_0) = 0)$. In other words, we are assuming that the twist of the substrates induces only twist deformations on the director. In this case, $f(\theta) = \alpha_1$ and $g(\theta) = \alpha_2$, both constants. Nevertheless, $d\varphi/dz$ will be constant, which will lead to the solution

$$\varphi(z) = \varphi_0\frac{z}{\ell_0}, \tag{3.9}$$

where here we consider a sample whose azimuth angle, φ, of the director varies in a homogeneous helix, going from 0 to its maximum twist angle, φ_0. This representation for $\varphi(z)$ seems not to be unique. However, we will consider such result as a homogeneous solution, as is done in [56], and find another particular solution when the field is present. Let us consider an expression for θ of the type

$$\theta(z) = \theta(\ell_0 - z),\ 0 \le \theta \le \ell_0/2, \tag{3.10}$$

$$\left.\frac{d\theta}{dz}\right|_{z=\ell_0/2} = 0, \tag{3.11}$$

and

$$\theta(\ell_0/2) = \theta_m. \tag{3.12}$$

The derivative condition will assure θ to have an extremum exactly at the middle of the sample, which, as a consequence, will also be a point of return. Since θ might be chosen to be positive without loss of generality, its value will rise from $z = 0$ to $z = \ell_0/2$, reach its extremum, and decay the same way it has risen, given the symmetry of the problem.

Analyzing such conditions, θ will reach a maximum at $\ell_0/2$, due to its positivity. That value will be called θ_m here.

Let us return to equation (3.7) and equation (3.8). Given our assumptions, they will yield

$$\frac{d\varphi}{dz} = \frac{C_1}{g(\theta)} \tag{3.13}$$

and

$$f(\theta) \left(\frac{d\theta}{dz}\right)^2 = \nu H^2 (\sin^2 \theta_m - \sin^2 \theta) + C_1^2 \left(\frac{1}{g(\theta_m)} - \frac{1}{g(\theta)}\right). \tag{3.14}$$

A solution for the polar angle then comes directly,

$$z = \int_0^\theta \left[\frac{f(\psi)}{\nu H^2 (\sin^2 \theta_m - \sin^2 \psi) + C_1^2 \left(\frac{1}{g(\theta_m)} - \frac{1}{g(\psi)}\right)}\right]^{1/2} d\psi, \tag{3.15}$$

for $0 \le z \le \ell_0/2$. Equivalently,

$$\varphi = \frac{\varphi_0}{2} + \int_0^{\theta_m} \left[\frac{f(\psi)}{\nu H^2 (\sin^2 \theta_m - \sin^2 \psi) + C_1^2 \left(\frac{1}{g(\theta_m)} - \frac{1}{g(\psi)}\right)}\right]^{1/2} \frac{C_1}{g(\psi)} d\psi. \tag{3.16}$$

Again, $0 \le z \le \ell_0/2$. The constants θ_m and C_2 must, however, satisfy some conditions. The solutions must be self consistent. Those requirements are

$$\frac{\ell_0}{2} = \int_0^{\theta_m} \left[\frac{f(\psi)}{\nu H^2 (\sin^2 \theta_m - \sin^2 \psi) + C_1^2 \left(\frac{1}{g(\theta_m)} - \frac{1}{g(\psi)}\right)}\right]^{1/2} d\psi, \tag{3.17}$$

that is, θ should be θ_m at the middle of the cell, and

$$\frac{\varphi_0}{2} = \int_0^{\theta_m} \left[\frac{f(\psi)}{\nu H^2 (\sin^2 \theta_m - \sin^2 \psi) + C_1^2 \left(\frac{1}{g(\theta_m)} - \frac{1}{g(\psi)}\right)}\right]^{1/2} \frac{C_1}{g(\psi)} d\psi, \tag{3.18}$$

which is an analogy to φ — it should be $\varphi_0/2$ in the middle of the cell. These last two equations, equation (3.17) and equation (3.18), will return the values of θ_m and C_1 for a given field strength H.

By performing the change of variables $\sin \lambda = \sin \psi / \sin \theta_m$, the aforementioned equa-

tions will become

$$\frac{\ell_0}{2} = \int_0^{\pi/2} \left[\frac{f(\psi)}{\nu H^2 - C_1^2 F(\psi, \theta_m)/[g(\psi)g(\theta_m)]} \right]^{1/2} \frac{d\lambda}{\cos \psi}, \tag{3.19}$$

$$\varphi_0 = \int_0^{\pi/2} \left[\frac{f(\psi)}{\nu H^2 - C_1^2 F(\psi, \theta_m)/[g(\psi)g(\theta_m)]} \right]^{1/2} \frac{C_1 d\lambda}{\cos (\psi)g(\psi)}, \tag{3.20}$$

where

$$F(\psi, \theta_m) = \frac{g(\theta_m) - g(\psi)}{\sin^2 \theta_m - \sin^2 \psi} \tag{3.21}$$

$$= \alpha_3 - 2\alpha_2 - (\alpha_3 - \alpha_2)(\sin^2 \psi + \sin^2 \theta_m). \tag{3.22}$$

From equations (3.19) and (3.20), it follows that

$$\lim_{\theta_m \to 0} C_1 = \frac{\alpha_2 \varphi_0}{\ell_0/2} \tag{3.23}$$

and

$$\lim_{\theta_m \to 0} \nu \left(\frac{\ell_0}{2} \right)^2 H^2 = \alpha_1 \left(\frac{\pi}{2} \right)^2 + (\alpha_3 - 2\alpha_2)\varphi_0^2. \tag{3.24}$$

In equation (3.24), we are assuming that either $\alpha_3 \geq 2\alpha_2$ or $\varphi_0^2 \leq \alpha_1 \pi^2/4(2\alpha_2 - \alpha_3)$.

By performing once again a change of variables, $\beta = \sin^2 \theta_m$, the differentiation of equations (3.19) and (3.20) with respect to β will yield

$$\ell_0 \left(\frac{dC_1}{d\beta} \right)_{\beta=0} = (\alpha_3 - 2\alpha_2)\varphi_0, \tag{3.25}$$

$$2\nu \left(\frac{\ell_0}{2} \right)^2 \left(\frac{dH^2}{d\beta} \right)_{\beta=0} = \alpha_3 \left(\frac{\pi}{2} \right)^2 - \frac{\varphi_0(\alpha_3^2 - \alpha_3\alpha_2 + \alpha_2^2)}{\alpha_2}. \tag{3.26}$$

If our previous assumptions hold, and $\varphi_0^2 < \alpha_3\alpha_2\pi^2/4(\alpha_3^2 - \alpha_3\alpha_2 + \alpha_2^2)$, we arrive at the condition that

$$\left(\frac{dH}{d\beta} \right)_{\beta=0} > 0. \tag{3.27}$$

Our assumptions were necessary, therefore, to ensure that θ_m monotonically increases as the external field is also increased.

Since there are multiple solutions to our problem, we will filter the solution that minimizes the energy function [59]

$$\varepsilon = \int_V \left\{ W - \frac{1}{2} \left[(\nu_1 - \nu_2)(\vec{H} \cdot \vec{n})^2 + \nu_2 (\vec{H} \cdot \vec{H}) \right] \right\} dV, \qquad (3.28)$$

based on the argument that we must ensure the stability of our system [56].

If we denote by ε_0 the value of the integral above (equation (3.28)) when the solution found before (equations (3.19) and (3.20)) has a null external field, and introduce $\Delta = \varepsilon - \varepsilon_0$, we arrive at [56]

$$\Delta = A \int_0^{\pi/2} \frac{[f(\psi)]^{1/2}[\nu H^2 \sin^2 \theta_m \cos 2\lambda + C_1^2/g(\theta_m) - \alpha_2 \varphi_0^2/(\ell_0/2)^2]}{\cos \psi [\nu H^2 - C_1^2 F(\psi, \theta_m)/g(\psi)g(\theta_m)]^{1/2}} d\lambda, \qquad (3.29)$$

where A is the area of the glass plates.

By differentiating equation (3.29) and the relations of self-consistency (equations (3.19) and (3.20)), one can show that [56]

$$\left(\frac{d\Delta}{d\beta} \right)_{\beta=0} = 0, \qquad (3.30)$$

$$2\ell_0 \left(\frac{d^2\Delta}{d\beta^2} \right)_{\beta=0} = -A \left[\alpha_3 \left(\frac{\pi}{2} \right)^2 - \frac{(\alpha_3^2 - \alpha_3 \alpha_2 + \alpha_2^2)\varphi_0}{\alpha_2} \right]. \qquad (3.31)$$

If our previous assumptions hold, then $\varepsilon > \varepsilon_0$ for values of θ_m in a neighbourhood of zero.

Our analysis leads to the existence of a critical field H_c, where external fields greater than this critical value disturb the simple twisted orientation pattern and lead to new solutions. That is,

$$H_c^2 = \frac{1}{\nu(\ell_0/2)^2} \left[\alpha_1 \left(\frac{\pi}{2} \right)^2 + (\alpha_3 - 2\alpha_2)\varphi_0^2 \right]. \qquad (3.32)$$

As was predicted in [60], it is possible to obtain the value of the elastic constants appearing in equation (3.32) experimentally and estimate a possible threshold value from the results. More specifically, if we consider a $\varphi_0 = \pi/2$ rad twist cell, and the external field to be an electric field, the following substitutions shall be done: $H_c \to E_c$ and

56

$\nu \to \Delta\epsilon/(4\pi)$, leading us to

$$(E_\mathrm{c}\ell_0)^2 = \frac{4\pi}{\Delta\epsilon}\pi^2(\alpha_1 + \alpha_3 - 2\alpha_2), \qquad (3.33)$$

the well-known Freedericksz threshold voltage expression for a twisted nematic cell. Or, in a more common notation, as is expressed in [53, 61],

$$V_\mathrm{th} = \pi\sqrt{\frac{\pi}{\Delta\epsilon}(4K_{11} + K_{33} - 2K_{22})}. \qquad (3.34)$$

As a reference to homeotropic and planar cells, where special cases for the Freedericksz transition threshold voltage expressions exhibit dependences only on the splay (K_{11}, pure S-effect), twist (K_{22}, pure T-effect), and bend (K_{33}, pure B-effect) elastic constants in a similar fashion to equation (3.34) (with $(4K_{11} + K_{33} - 2K_{22}) \to K_{ii}$), the constant $4K_{11} + K_{33} - 2K_{22}$ is sometimes called k, the "effective twist constant".

Straightforward experiments may be performed in order to measure the threshold voltage. By knowing the dielectric anisotropy — which may be, for instance, measured from capacitance experiments [53, 62] — one has a concrete estimative for the effective twist elastic constant. As was mentioned before and will later be discussed with detail, the reorientation of the director will change the sample birefringence, a parameter which might be easily obtained analyzing the transmittance of polarized white or monochromatic light through our material [53, 63]. For example, one may start from a null field and steadily increase its strength. As soon as the intensity captured in our detector changes, the director is starting to reorient and we have our threshold value.

3.2   Transmission spectra of twisted liquid crystals

Let us now evaluate the linear transmission of light through a twisted nematic sample. Both glass plates here present parallel-alignment boundary conditions, and the alignment directions are forming an angle θ between each other. For the purpose of this section, no external field will be present. Several fundamentally different methods can be used to

achieve the same solution for this problem [53], each one giving insight over a particular feature of twisted nematic cells: (1) the generalized geometrical-optics approximation, which considers the propagation of ordinary and extraordinary waves within samples [64]; (2) the 4x4 matrix method, which considers how the electric field components of light behave when impinging the cells at any incidence [65, 66, 67, 68, 69]; and (3) the Jones matrix method, consisting in treating polarized light propagating as Jones vectors and the material as linear optical elements, the Jones matrices [70]. Here, we will be using one of the methods described in [71], the approach of segmented layers.

Consider our medium as segmented layers, where every layer has its optical axis along the x'-direction. The $(m+1)$-th layer will have its optical axis rotated by $\delta\theta$ with respect to the m-th layer, along the z (propagation) axis.

The electric field exiting the m-th layer will be

$$E(x')_m = A_m \sin \omega t + B_m \cos \omega t, \tag{3.35}$$

$$E(y')_m = C_m \sin \omega t + D_m \cos \omega t. \tag{3.36}$$

When this wave reaches the $(m+1)$-th layer, its components will be transmitted to the $(m+2)$-th layer with a relative phase difference of $\delta\phi = 2\pi\Delta n\delta z/\lambda$, with δz being the thickness of each plate.

The light emerging from the $(m+1)$-th plate will then be

$$A_{m+1} = A_m \cos \delta\theta - C_m \sin \delta\theta, \tag{3.37}$$

$$B_{m+1} = C_m \cos \delta\theta - D_m \sin \delta\theta, \tag{3.38}$$

$$C_{m+1} = (A_m \sin \delta\theta + C_m \cos \delta\theta) \cos \delta\theta - (B_m \sin \delta\theta + D_m \cos \delta\theta) \sin \delta\theta, \tag{3.39}$$

$$D_{m+1} = (B_m \sin \delta\theta + D_m \cos \delta\theta) \cos \delta\theta + (A_m \sin \delta\theta + C_m \cos \delta\theta) \sin \delta\theta. \tag{3.40}$$

These equations can be combined to give a recursion relation on A:

$$A_{m-2} - 2A_{m-1}(1 + \cos \delta\phi) \cos \delta\theta + 2A_m[(1 + \cos \delta\phi) \cos^2 \delta\theta + \cos \delta\phi] -$$

$$- 2A_{m+1}(1 + \cos \delta\phi \cos \delta\theta + A_{m+2} = 0. \quad (3.41)$$

Equivalent relations can be found for B, C and D.

We can write A as a continuous function of z, by taking the m-th plate to be a distance z_m from the origin. That is,

$$A_{m-n} = A(z_m - n\delta z). \quad (3.42)$$

Now, it is possible to expand equation (3.41) around z_m, with $\delta\phi$, δz, $\delta\theta \to 0$. We will be left with

$$\frac{d^4 A}{dz^4} + \left[\frac{2\theta^2}{\ell_0^2} + 4\left(\frac{\pi \Delta n}{\lambda} \right)^2 \right] \frac{d^2 A}{dz^2} + \alpha^4 = 0. \quad (3.43)$$

This differential equation can be integrated to yield

$$A = a_1 \cos (q\alpha z) + a_2 \sin (q\alpha z) + a_3 \cos (\alpha z/q) + a_4 \sin (\alpha z/q), \quad (3.44)$$

with $q = \sqrt{1 + 2u^2 + 2u(1 + u^2)^{1/2}}$, and $u = \pi \ell_0 \Delta n / \theta \lambda$. The equations for B, C and D will be alike, but the constants will be represented by b_1, b_2, c_1, and so on.

If we consider as our boundary condition a perpendicularly incident beam with a polarization angle parallel to the alignment induced by the bottom glass surface — that is, parallel to the x-axis of the first layer ($z = 0$), our amplitudes are

$$A = \frac{q^2}{1 + q^2} \cos \left(\frac{\alpha z}{q} \right) + \frac{1}{1 + q^2} \cos (q\alpha z), \quad (3.45)$$

$$B = \frac{-q^2}{1 + q^2} \sin \left(\frac{\alpha z}{q} \right) + \frac{1}{1 + q^2} \sin (q\alpha z), \quad (3.46)$$

$$C = \frac{q}{1 + q^2} \sin \left(\frac{\alpha z}{q} \right) + \frac{q}{1 + q^2} \sin (q\alpha z), \quad (3.47)$$

$$D = \frac{q}{1 + q^2} \cos \left(\frac{\alpha z}{q} \right) - \frac{q}{1 + q^2} \cos (q\alpha z). \quad (3.48)$$

For the light exiting the liquid crystal, we should analyze the components at $z = \ell_0$. If

we are interested specifically in light polarization perpendicular to the angle θ, we should take $T = C^2 + D^2$, which will yield

$$T(u) = \frac{\sin^2\left(\theta\sqrt{1+u^2}\right)}{1+u^2}. \tag{3.49}$$

The previously derived expression dictates the transmission spectra of a twisted nematic cell when the input polarizer is parallel to the alignment direction at $z = 0$ and the output polarizer perpendicular to θ, the alignment direction at $z = \ell_0$. Note how equation (3.49) will present successive minima, given the dependence on the sine function at the numerator. The nuances of such expression for $\pi/2$ rad cells and its usefulness on determining the nematic birefringence will be discussed later, in section 3.4.

3.3 Birefringence and single-band model

In 1966, Vuks reported the development of a semiempirical model analogous to the Clausius-Mossotti equation for correlating the microscopic molecular polarizabilities to the macroscopic refractive indices of crystalline materials [72].

The macroscopic relative permittivity of our medium (ϵ_r) is related to the atomic polarizability (α), a microscopic parameter of the molecules constituting the system, through the Clausius-Mossotti relation [73, 74],

$$\frac{\epsilon_\mathrm{r} - 1}{\epsilon_\mathrm{r} + 2} = \frac{4\pi}{3} N\alpha. \tag{3.50}$$

Here, N is the number of molecules per cm^3, and all values here are in the cgs system of units.

This equation is valid as long as the frequency regime is low. In the optical frequency regime, one should, as a rule of thumb, substitute $\epsilon \to n^2$ to obtain the Lorentz-Lorenz equation [73, 72, 75, 76],

$$\frac{n^2 - 1}{n^2 + 2} = \frac{4\pi}{3} N\alpha. \tag{3.51}$$

In a liquid crystal, however, two refractive indices are observed — $n_\perp$ and $n_\parallel$. The same

holds true for molecular polarizabilities. In fact, a first attempt was made, considering each polarizability ($\alpha_\perp$ and $\alpha_\parallel$) to be related to a refractive index ($n_\perp$ and $n_\parallel$). There, α was simply replaced by $\alpha_{\perp,\parallel}$ and n by $n_{\perp,\parallel}$ in equation (3.51) [77], but further experiments showed this assumption to be unfit.

Several models were developed in an attempt to relate the macroscopic permittivity of liquid crystals to molecular polarizabilities [78, 79], but the expressions for the permittivities are rather intricate for practical uses. One particular semi-empirical assumption that yields fruitful results is made in [80], where the internal field in a crystal (Lorentz field) is taken to be isotropic [81]. That is,

$$\vec{E_i} = \frac{\langle n^2 \rangle + 2}{3} \vec{E}. \tag{3.52}$$

With such assumption, an useful expression relating microscopic molecular polarizabilities and macroscopic refractive indices can be derived [80]:

$$\frac{n_{\perp,\parallel}^2 - 1}{\langle n^2 \rangle + 2} = \frac{4\pi}{3} N \alpha_{\perp,\parallel}. \tag{3.53}$$

Consequently, the birefringence, $\Delta n = n_\parallel - n_\perp$, can be written as

$$\Delta n = \left(\frac{\langle n^2 \rangle + 2}{n_\parallel + n_\perp} \right) \frac{4\pi}{3} N(\alpha_\parallel - \alpha_\perp). \tag{3.54}$$

However, since our material is a liquid crystal, its polarizability will be related to that of a perfect crystal by an order parameter, S [82]. That is,

$$\alpha_\parallel - \alpha_\perp = S(\gamma_\parallel - \gamma_\perp). \tag{3.55}$$

The polarizability of a molecule in the ground state at a certain frequency is given by the sum over all possible quantum transitions [83, 84],

$$\gamma_m \propto \sum_n \frac{Z f_{mn}}{\omega_{mn}^2 - \omega^2}, \tag{3.56}$$

where Z is the number of active electrons per molecule and f_{mn} is the oscillator strength. Here, we have considered no damping in the harmonic oscillator. Equivalently, we may write equation (3.56) in terms of the wavelength

$$\frac{Zf_{mn}}{\omega_{mn}^2 - \omega^2} \propto Zf_{mn}\frac{\lambda_{mn}^2\lambda^2}{\lambda^2 - \lambda_{mn}^2}. \tag{3.57}$$

If we consider the typical absorption bands of calamitic molecules of liquid crystal systems, λ_1, λ_2, and λ_3, assume that each band is closely separated to one another, with f_1, f_2, and f_3 as their corresponding oscillator frequencies, at a wavelength far away from resonance ($\lambda \gg \lambda_1$, λ_2, and λ_3):

$$f_{m1}\lambda_1^2 + f_{m2}\lambda_2^2 + f_{m3}\lambda_3^2 \approx \bar{f}_m\bar{\lambda}^2. \tag{3.58}$$

Above, $\bar{\lambda}^2 = (\lambda_1^2 + \lambda_2^2 + \lambda_3^2)/3$ and $\bar{f}_m = f_{m1} + f_{m2} + f_{m3}$. Well, $\bar{f}_m$ here will not be of much importance, for it is only a proportionality constant. The resulting polarizability will be

$$\gamma_m \propto Z\bar{f}_m\frac{\bar{\lambda}^2\lambda^2}{\lambda^2 - \bar{\lambda}^2}. \tag{3.59}$$

Through equations (3.54), (3.56), (3.57) and (3.59), we arrive at our final expression for the birefringence,

$$\Delta n(\lambda, T) = gNZS(\bar{f}_\parallel - \bar{f}_\perp)\frac{\bar{\lambda}^2\lambda^2}{\lambda^2 - \bar{\lambda}^2}, \tag{3.60}$$

where g is a proportionality constant, involving the multiplicative constants in equation (3.54) and the proportionality factor implicit in equation (3.56). In particular, it was found empirically that the value $(\langle n^2\rangle + 2)/(n_\parallel + n_\perp)$ is bound between a narrow region, and is practically insensitive to chemical composition, temperature, and wavelength. By testing parameters for liquid crystals that maximize and minimize the values of the constant, it was found that [84]

$$\frac{\langle n^2\rangle + 2}{n_\parallel + n_\perp} = 1.40 \pm 0.03. \tag{3.61}$$

Moreover, the proportionality between the atomic polarizability and the quantum transitions is also temperature independent, because all thermal contributions are cloistered in Zf_{mn}. Consequently, we may take g as independent of temperature and wavelength. $NZS(\bar{f}_{\parallel} - \bar{f}_{\perp})$, on the other hand, is temperature dependent, but wavelength independent [53]. So we may merge all thermal contributions in a constant $G(T)$, to be left with

$$\Delta n(\lambda, T) = G(T)\frac{\bar{\lambda}^2 \lambda^2}{\lambda^2 - \bar{\lambda}^2}. \tag{3.62}$$

Equation (3.62) predicts the behavior of birefringence as temperature and wavelength are varied. What is particularly remarkable about the single-band model is that by measuring a determined birefringence at a particular wavelength, one may directly obtain $G(T)$ and estimate the birefringence as a function of wavelength for that particular temperature, as long as λ lies within the domain where equation (3.62) holds — that is, far from resonance bands. In particular, refractive indices and absorption coefficients experiments performed in cyanobiphenyls have shown that equation (3.62) and another model considering three separate absorption bands for possible quantum transitions (the three-band model) yield numerically similar results, both being equally very good in fitting experimental data [85].

3.4 Gooch-Tarry conditions and Mauguin minima

As we have seen before, the transmittance of a twisted nematic cell between parallel polarizers is given by the expression [71]

$$T = \frac{\sin^2\left(\frac{\pi}{2}\sqrt{1 + u^2}\right)}{1 + u^2}, \tag{3.63}$$

when the input polarizer is aligned parallel to input glass rubbing direction.

If we examine the plot of such function, one can see that it has infinite minima, given by the values of u in which the sine function in the numerator will be null, since the denominator in this case will never diverge for non-zero wavelengths (that is, finite u).

Figure 3.1: Transmission spectrum for a twisted nematic cell.
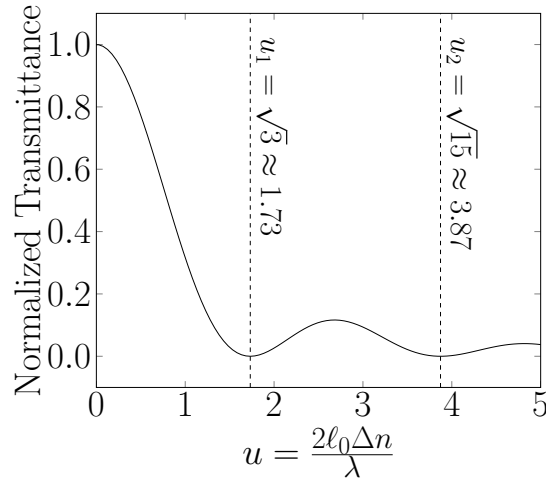
Source: Author (2019).

Consequently, the minima of our transmittance will be given by

$$\frac{\pi}{2}\sqrt{1 + u^2} = m\pi, \tag{3.64}$$

where m here will be a natural number, due to the domain of equation (3.63). For convenience, let us enumerate our minima. Since u is strictly positive, and T is regular for finite u, we will have a first minimum, a second, and so on. Let us assign each minimum to one corresponding value of m, where the first minimum of our function will be given at $m = 1$, the second at $m = 2$, and so on.

This leaves us with

$$u_m = \sqrt{4m^2 - 1}, \; m \in \mathbb{N}^*, \tag{3.65}$$

where u_m is the position of the m-th minimum of the transmittance. Writing this in terms of the wavelength,

$$\frac{2\ell_0 \Delta n}{\lambda_m} = \sqrt{4m^2 - 1}, \; m \in \mathbb{N}^*, \tag{3.66}$$

which means we can extract information of the sample birefringence at all λ_m within the physical limitations of our equipment yielding the transmission spectra. The values for the birefringence, Δn, at the measured minima, λ_m, are

$$\Delta n(\lambda_m) = \frac{\lambda_m}{d} \frac{\sqrt{4m^2 - 1}}{2}, \; m \in \mathbb{N}^*. \tag{3.67}$$

Such conditions are called the Gooch-Tarry conditions [71], which make possible for us to evaluate the liquid crystal birefringence at a specific wavelength, given that it is a minimum of transmission. These wavelengths where optical transmission is null are called the Mauguin minima. By simply measuring a Mauguin minima, one has a powerful tool to determine the sample birefringence following equation (3.67), as stated before.

Looking at equation (3.63), one may inquire why don't we analyze T at the desired λ and get $\Delta n(\lambda)$ directly, instead of going through the Mauguin minima, obtaining $\Delta n(\lambda_m)$, and then using some complementary model (such as the previously derived single-band, or three-band models) to estimate $\Delta n(\lambda)$. The answer is simple: it is not quite easy to normalize T, because we never know how far in the infrared one should go to obtain a satisfactory approximation for $T(u \to 0)$. Furthermore, it is rather uncommon for portable spectrometers to measure a good range of IR transmission, together with the fact that polarizers don't perform well in long wavelength ranges — making the use of several polarizers necessary and the experimentation involved. Another important consideration to take into account is the scenario where the sample is doped with guests presenting strong absorption coefficients, such as dyes and plasmonic nanoparticles. The transmittance will be heavily influenced by the presence of doping agents, being unreliable in magnitude to describe the twist structure. Still, the minima will never change, no matter how extreme the extinction coefficients of dopants are.

Let us also consider a real case scenario and make a simple estimative to illustrate how experimentation will usually work. For typical liquid-crystalline materials like cyanobiphenyls, Δn is of the order of 0.1 to 0.2. Sample thickness, ℓ_0, is usually around 10 μm with cellulose spacers. Portable spectrometers usually measure about 400 to 900 nm wavelength. These parameters will yield a first minimum at 1000 to 2000 μm, a second minimum at 500 to 1000 μm, a third minimum at 350 to 700 μm, and so on. So, in experiments employing portable spectrometers, m for the related minima will usually range from 2 to 4. Of course, thicker or thinner samples might be employed. One may use, for example, mylar spacers, whose thickness can reach 100 μm, and this will change the ensuing wavelengths and values of m observed experimentally.

4

Samples preparation and experimental setups

This chapter is dedicated to carefully describe the steps taken to set our experiments up, from the production of gold nanorods to beam waist measurements to the programming of instruments. The first section contains a discussion on the synthesis of gold nanorods using the seed-mediated method, as well as procedures related to their characterization. In the second section, our liquid crystal compound is presented, together with the protocol employed to transfuse gold nanorods to it. The third section is focused on detailing the treatment of substrates to ensure alignment, as well as cell assembly process and its initial characterizations. Further, the experimental setups for the Z-scan and electro-optical response are outlined in sections four and five, respectively.

4.1   Seed-mediated synthesis of gold nanorods

Gold nanorods were prepared in aqueous solution by the seed-mediated method, described in reference [86], with cethyltrimethylammonium bromide (CTAB) as the capping agent. According to the concentration of the growth solution added to the seed solution, different aspect ratios of gold nanorods could be obtained. In order to verify if the aqueous dispersions contain the characteristic extinction profile of gold nanorods and obtain a first estimative of the mean aspect ratio, aqueous dispersions were analyzed in a quartz cuvette, and unpolarized light extinction curves were measured using a portable UV-VIS spectrometer (Ocean Optics USB 4000) and Ocean Optics Spectra Suite software. Several

Figure 4.1: Plasmonic extinction spectra for gold nanorod aqueous dispersions obtained through several different syntheses. Here, the longitudinal plasmonic extinction peak is highlighted for each dispersion, together with the aspect ratio estimated from peak position. Besides the shown curves ($\bar{r} = 1.9, 2.1, 3.1, 3.5$), other aspect ratios were also obtained, namely, $\bar{r} = 2.0, 2.5$ (not shown).
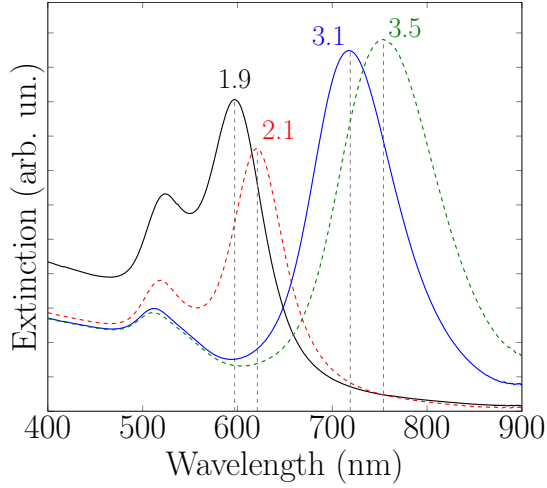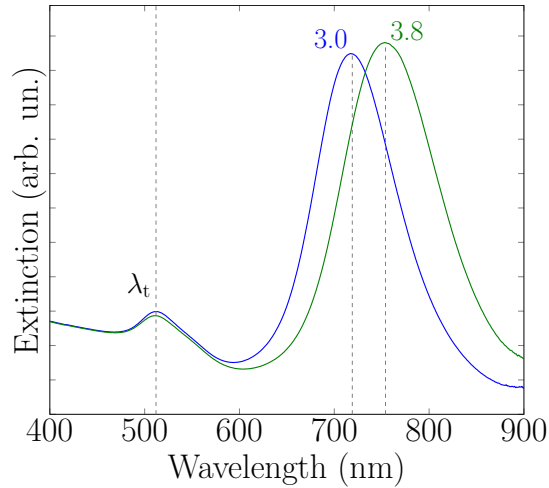

Source: Author (2019).

gold nanorod aqueous dispersions presenting nanoparticles at different aspect ratios were synthesized, ranging from $\bar{r} = 1.8$ to $\bar{r} = 3.8$, and their extinction spectra are shown in figure 4.1. Even though all nanoparticles from the aqueous dispersions were transfused to the liquid crystal compound and the doped materials transferred to closed cells, not all samples were used. For the thermo-optical and nonlinear optical characterization, only $\bar{r} = 2.5$ was available at the time, so it was the only sample studied. For the viscoelastic and birefringence characterization, all samples except the higher aspect ratio ones ($\bar{r} = 3.0$ and $\bar{r} = 3.8$) presented strong absorption bands encompassing $\lambda = 633$ nm, which made measurements unreliable, because that was the wavelength of our probe beam. In spite of having lasers operating at several wavelengths available in our laboratory, from ultraviolet to infrared, only the helium-neon (at 633 nm) had enough stability around the required power to be used as a probe beam.

For clarity, the extinction spectra of the gold nanorod dispersions used in each section of the experimental results chapter are shown separately. Figure 4.3 shows the spectra for $\bar{r} = 2.5$ gold nanorods, where one may observe the transversal extinction band peaked at $\lambda_t \approx 512$ nm and the longitudinal band peaked at $\lambda_l = 656$ nm. Figure 4.2 equivalently shows $\bar{r} = 3.0$ and $\bar{r} = 3.8$ spectra, with the same transversal plasmonic extinction peak at $\lambda_t = 512$ nm, and slightly separated longitudinal peaks, at $\lambda_l = 719$ nm for $\bar{r} = 3.0$

Figure 4.2: Extinction spectra of gold nanorod aqueous suspension for two aspect ratios, $\bar{r} = 3.0$ and $\bar{r} = 3.8$. As we can see, both nanoparticle suspensions present the same transversal plasmon peak, located at $\lambda_t = 512$ nm, with slightly different longitudinal peaks, at 719 and 754 nm for $\bar{r} = 3.0$ and $\bar{r} = 3.8$, respectively.

Source: Author (2019).

Figure 4.3: Extinction spectra for $\bar{r} = 2.5$ gold nanorods in aqueous suspension. Here, the transversal absorption band is centered at $\lambda_t = 514$ nm, while the longitudinal band at $\lambda_l = 656$ nm. Note how the transversal plasmonic band is positioned close to the λ_t for the aqueous dispersions represented in figure 4.2.
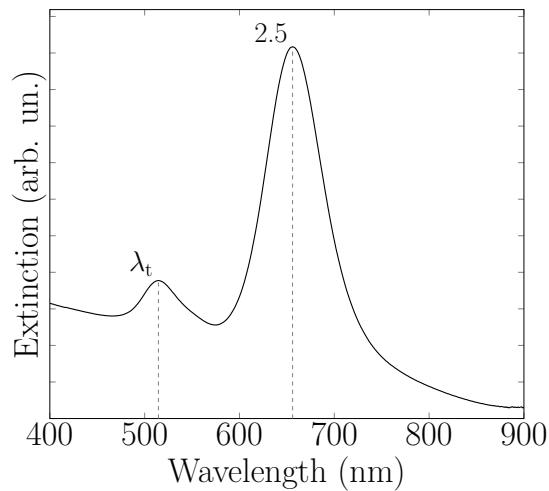
Source: Author (2019).

and $\lambda_l = 754$ nm for $\bar{r} = 3.8$.

4.2 Liquid crystal sample

The liquid crystal sample of choice here is 4-octyl-4-n'-cyanobiphenyl, commonly known as 8CB. Cyanobiphenyls, in particular, have several advantages for technological applications as well as experimentation [87, 88]. Their nematic phase is observed near room temperatures, while also presenting a wide nematic range and good chemical stability under laser exposure. Our liquid crystal, 8CB, was purchased from Sigma-Aldrich and used as obtained, without further purification. It presents both nematic and smectic-A phases, with the isotropic to nematic phase transition occurring at 313.5 K and the nematic to smectic-A phase transition at 306.5 K. A ball-and-stick model schematic representation of 8CB is shown in figure 4.4, where carbons are represented as gray spheres, nitrogen as the blue sphere and hydrogen atoms as white spheres. The molecular positioning and angles were calculated at $T = 0$ using the universal force field for the atomic potentials, where energy was then minimized via the steepest descents method, all calculations done by Avogadro (the software). Please note that the molecules and bonds are out of scale to represent the space-filling model. In order to clarify the visualization of positioning and relative angles for atoms and bonds, both spheres and bonds had their radii divided by half, and bonds were further stretched to double length. Overall, the molecules present an average length of 25 Å.

Table 4.1: Average length, L, and diameter, D, of gold nanorods, measured in nm, together with the aspect ratio, $\bar{r} = L/D$, for each of the obtained samples. One example micrograph for each of the grids is shown in figure 4.5.

Sample label	L (nm)	D (nm)	$\bar{r} = L/D$
8CBNR1	42 ± 4	14 ± 1	3.0
8CBNR2	38 ± 3	10 ± 1	3.8

After the syntheses described in section 4.1, gold nanorods were transfused to 8CB in the isotropic phase at a small weight concentration of $c = 0.02$ wt.%, aiming the formation of a stable dispersion without any visible aggregates in the ensuing system. CTAB was shown to stay stable during the exchange of solvents and subsequent transfer process

Figure 4.4: Ball-and-stick model for 8CB, calculated using the universal force field as the interaction potential model, with parameters given by Avogadro (the software). The potential energy was minimized via the steepest descents method. Even though atomic positioning and bond angles are accurate, atomic and bond sizes are out of scale to improve visibility.
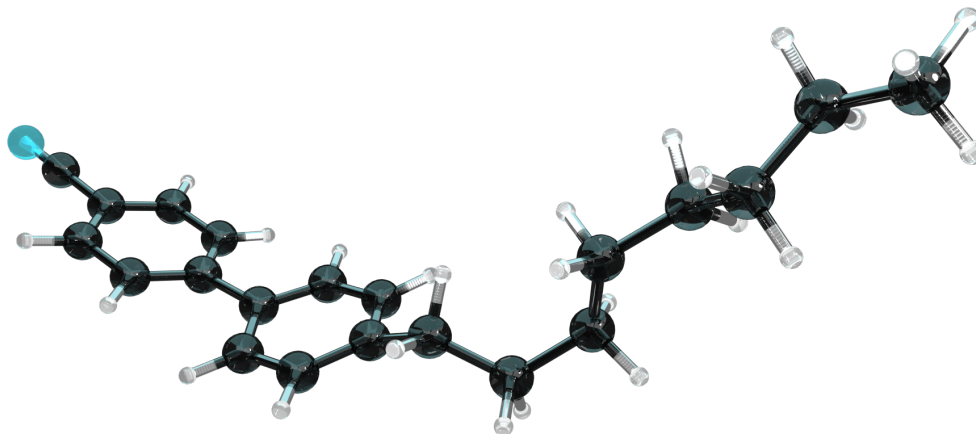
Source: Author (2019).

to the liquid crystal, with a homeotropic anchoring being expected at the nanoparticles surfaces [34]. In order to evaluate the mean size and aspect ratio of the gold nanorods inside the liquid-crystalline system, images obtained by transmission electron microscopy were examined, with the grids being prepared as described in [86], by casting a thin film of our doped samples over a copper grid coated with a porous carbon film. The first aqueous dispersion, shown in figure 4.3, was evaluated using a FEI-Tecnai 20 operating at 200 kV. The resulting micrographs were examined using the software Sigma Scan to determine mean particle size and their distribution, where approximately 100 nanoparticles were taken into account for each sample. A sample image captured by the microscope is shown in figure 4.6. The analysis returned an average length of $L = 40$ nm, average diameter of $D = 16$ nm, and aspect ratio of $\bar{r} = 2.5$ for the gold nanorods. Such material was used to perform the Z-scan experiment characterization. The other two aqueous dispersions, shown in figure 4.2, were subsequently transfused to 8CB and inspected by a FEI Tecnai Spirit Biotwin operating at 120 kV. For those samples, micrographs were analyzed via the software ImageJ Version 1.48v. Once again, approximately 100 nanoparticles were considered for each grid, and the results are summarized in table 4.1. For simplicity, the

Figure 4.5: Transmission electron microscopies after nanorods transfusion to 8CB. $\bar{r} = 3.0$ gold nanorods are presented in (a), while $\bar{r} = 3.8$ are shown in (b). Note that gold nanorods are surrounded by an 8CB shell, where a short-range alignment of guest particles is observed.
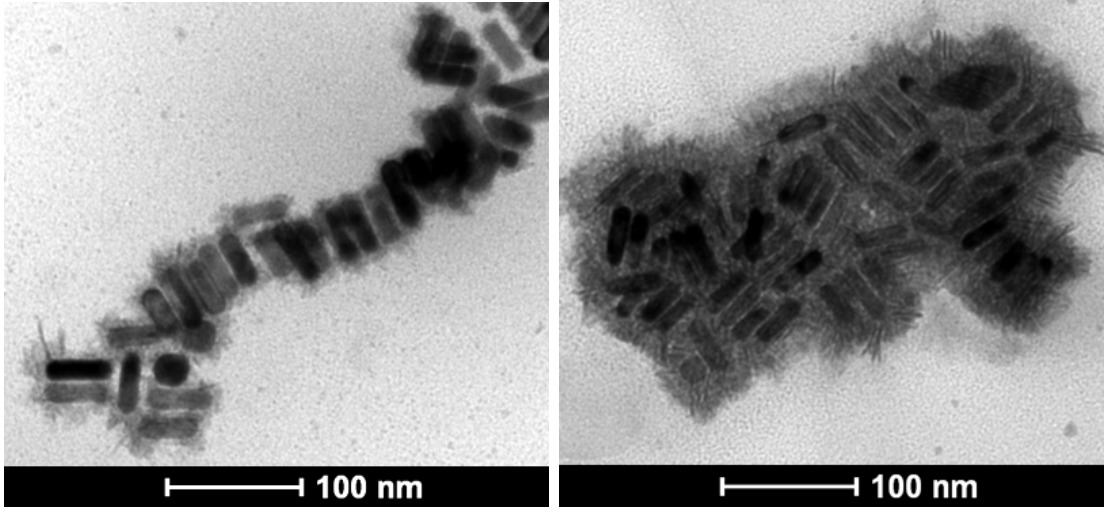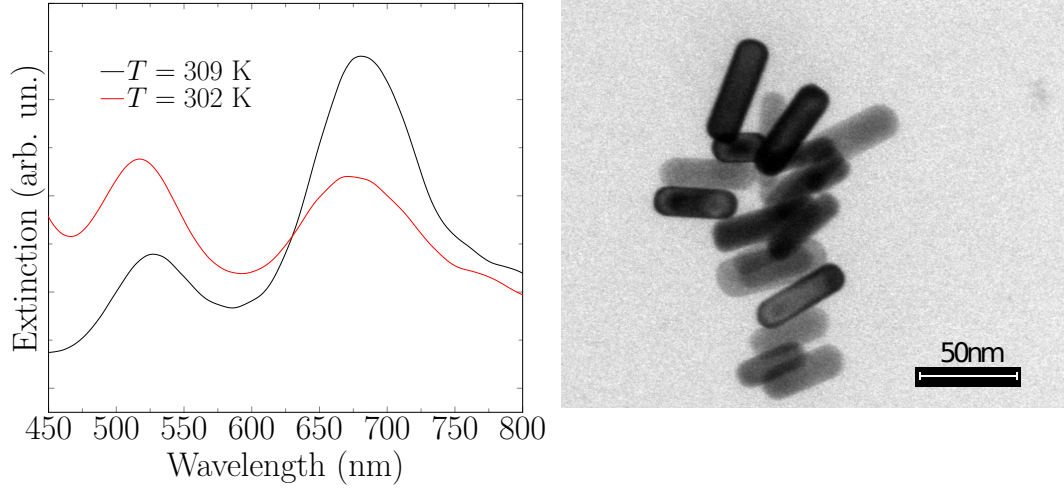

Source: Author (2019).

samples were labeled 8CBNR1 and 8CBNR2. Those samples were used in the electro-optical experiments, and a micrograph for each is shown in figure 4.5.

4.3   Cell preparation

In order to characterize the nonlinear optical properties of our samples using the Z-scan technique, a homeotropically-aligned cell was prepared by treating cleaned glass surfaces with octadecyl chlorosilane, a surfactant purchased from Sigma-Aldrich. Two homeotropic substrates were set parallel to each other, separated by two fixed thickness sheets (100 μm mylar spacers), and glued together using epoxy glue. After the resin was cured, our sample (8CB + 0.02 wt.% AuNR at $\bar{r} = 2.5$) was filled inside the cell through capillarity at the isotropic phase of 8CB ($T \approx 330$ K), closed with epoxy glue again, and slowly cooled to room temperature. To verify the alignment conditions, the sample was placed between crossed polarizers and analyzed through optical microscopy. Since homeotropic samples are optically isotropic to normal incidence, a light gray homogeneous pattern was observed, due to small fluctuations of the director within a thick sample. Extinction spectra for unpolarized white light perpendicularly at the filled cell is shown in figure 4.6, for two different temperatures, $T = 309$ K (nematic phase) and $T = 302$ K (smectic phase). As

Figure 4.6: Extinction spectra (a) and transmission electron microscopy (b) of 8CB samples doped with gold nanorods. The extinction curves were obtained for cells presenting a homeotropic alignment, and were measured at two distinct temperatures, $T = 309$ K (nematic phase) and $T = 302$ K (smectic-A phase). One observes a significant suppression of the longitudinal plasmonic peak together with an increase of the transversal peak as the temperature is lowered. Such behavior reveals the importance of the nematic and smectic ordering in the mean alignment of guest nanorods.
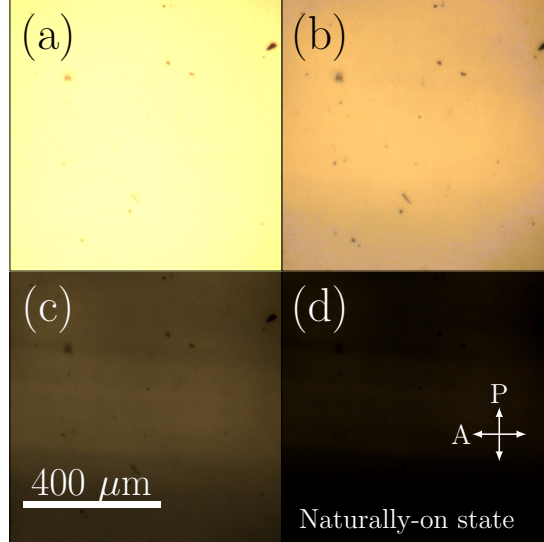

Source: Author (2019).

one can see, for temperatures where the smectic order is well established, the longitudinal plasmonic extinction band is hindered while the transversal band is boosted, indicating a reduction of thermal fluctuations of the orientation of gold nanorods together with an overall mean alignment along the far-field director.

The twisted alignment cells were prepared by coating indium-tin oxide (ITO) cleaned glass surfaces with polyvinyl alcohol (PVA) and further rubbing the substrate with velvet, in a way that each glass plate presents a rubbing direction perpendicular to the alignment of their matching plate. The direction of rubbing here also dictates the imposed alignment direction of molecules over the substrate. Two homogeneously aligned glass surfaces with alignment directions perpendicular to each other were then put together, separated by 10 μm thick cellulose spacers, and glued with epoxy resin. The thickness of empty cells were measured by the interferometric method described in [89]. Afterwards, the cells were filled with undoped 8CB, 8CBNR1, and 8CBNR2 samples by capillary action at the isotropic phase of 8CB ($T \approx 330$ K), closed with epoxy glue and slowly cooled to room temperature. Once again, samples were put into a hot stage and analyzed between crossed polarizers. When the input polarizer was set parallel to the input alignment direction and the analyzer parallel to the output alignment direction (the "correct" alignment

Figure 4.7: Polarized optical microscopy of 8CBNR1 at $T = 314$ K for several external AC voltage amplitudes at $f = 1.2$ kHz. The input polarizer was set parallel to the input alignment direction, with the analyzer perpendicular to the polarizer. (a) no applied voltage, (b) 1000 mV, (c) 2000 mV, (d) 3000 mV. Exposure time, white balance, gain, as well as other parameters were kept constant for all pictures. Notice how samples go from being fully-bright to dark as electronically-applied voltages increase in magnitude.

for full transmission), cells appear completely bright, as was previously shown. When temperature increases and samples enter the isotropic liquid phase, images get dark and the N $\leftrightarrow$ I transition temperature can be promptly determined. To ensure the proper functioning of the electronic circuit, external voltages were applied to the ITO-coated glasses, and samples appeared darker and darker as voltage amplitudes increased (see figure 4.7). It is important to stress that there is no distinction between left- and right-handed director twisting pattern here, so no handedness preference can be imposed. When sample temperatures are abruptly changed, domains of different handedness visible from optical microscopy form within the sample, separated by defect walls. To avoid such artifacts, sample temperatures were varied carefully and slowly, at an empirically ideal rate of approximately 0.3 K/min, where no defects could be observed.

4.4   Z-scan experiment setup

The experimental setup used to obtain the Z-scan transmittance curves is shown in figure 4.8. A diode-pumped solid-state laser operating at 532 nm was used as both pump

Figure 4.8: Diagram for the Z-scan experiment. The vertically polarized and collimated beam exiting the DPSS laser is focused and re-collimated afterwards by two convergent lenses. Such re-collimation allows the optical chopper to modulate the laser beam at the focus, thus reducing errors due to finite spot size. After being re-collimated, the beam is deflected through two mirrors, used to facilitate beam alignment. The light beam is then divided by a beam splitter, part to a reference detector (trigger signal), and part being later focused by a convergent lens. The liquid crystal cell is placed inside a thermal stage, moving back and forth the beam propagation direction by a computer-controlled stepper motor-powered optical rail. According to the sample position, a different beam intensity profile will impinge the sample, and a consequent position-dependent transmitted signal will be observed. Both open ($S = 1$) and closed ($S = 0.1$) aperture Z-scan transmittances are detected and sent to the oscilloscope, to be further acquired by the computer.
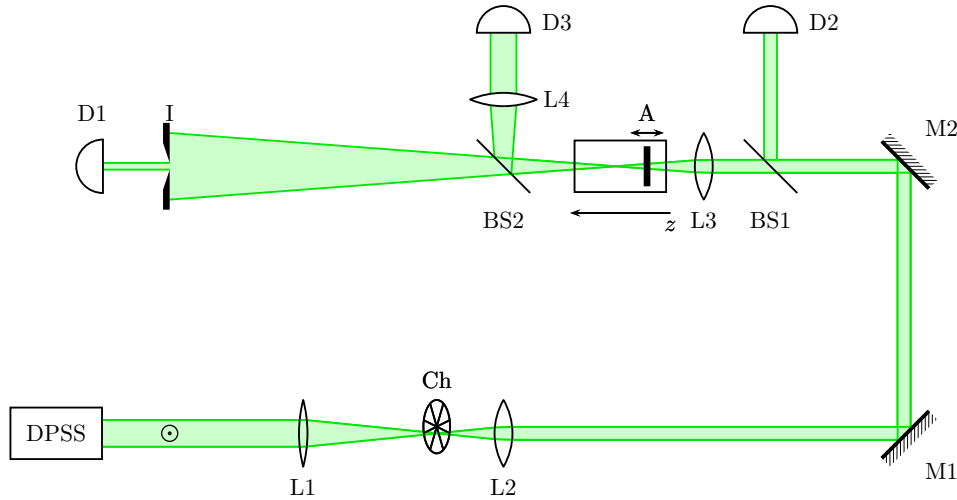
Source: Author (2019).

and probe beam (Coherent Verdi V6). The beam was focalized by a short focus lens to be mechanically modulated by an optical chopper at a smaller beam radius, as a means to improve square wave shapes. The modulated beam was then re-collimated and deflected by two mirrors, used to facilitate alignment, and split in two by a beam splitter. The light intensity from one of the arms was measured by a photodetector to be used as a trigger signal for the oscilloscope, and the other was focused by a convergent lens. A hot stage containing the sample was set over a long travel range motorized stage (Newport), where stage position could be fine-tuned by a computer. After exiting the sample, two possible experimental configurations were detected by photodetectors connected to the oscilloscope (Tektronix TDS 2022 B), one after passing an almost closed iris ($S = 0.1$) and the other being converged by a lens to the detector ($S = 1$). Five transient intensity curves were captured at each position, and 50 positions were used, with steps of 5 mm between each other. A computer script was written in Python language to automatize the experiments and yield CSV output data. Such experiment was performed for several

Figure 4.9: Normalized transmitted power through a 50 μm pinhole as a function of position along the light path (z-axis), for a Gaussian beam focused at $z = 0$. By adjusting the data points (grey circles) according to equation (4.3) (red line) with $\lambda = 532$ nm, a minimum beam waist of $\omega_0 = 50$ μm and a Rayleigh range of $z_\mathrm{R} = 14.7$ mm were obtained.
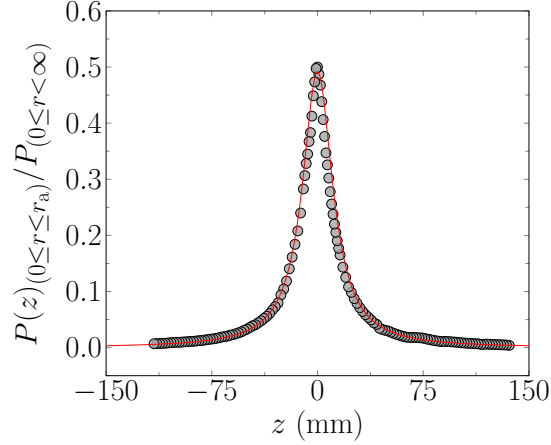
temperatures in the smectic-A as well as nematic ranges, in increments of 0.5 K, and a set thermal stabilization time of approximately 15 min.

In order to measure the beam waist and further obtain the Rayleigh range, a 50 μm pinhole was moved back and forth along the z-axis (propagation direction) and the transmitted power recorded for each position. Since we know the transmitted power for a fixed aperture and the input intensity, we also know the beam radius, ω, as a function of z. In fact, one can obtain the transmitted power by integrating the Gaussian distribution of intensities from 0 to r_a, the aperture radius, which gives us

$$P(z)_{(0 \leq r \leq r_\mathrm{a})} = P_{(0 \leq r < \infty)} \left[1 - \exp\left(\frac{-2r_\mathrm{a}^2}{\omega^2(z)} \right) \right]. \tag{4.1}$$

$P_{(0 \leq r < \infty)}$ can be obtained by measuring the incident power before the aperture, and r_a, the radius of the pinhole, is specified by the manufacturer. As shown in previous chapters, $\omega^2(z)$ is given by

$$\omega^2(z) = \omega_0^2 \left[1 + \left(\frac{\lambda z}{\pi \omega_0^2} \right)^2 \right]. \tag{4.2}$$

Inserting equation (4.2) in equation (4.1), we have

$$\frac{P(z)_{(0\leq r\leq r_{\mathrm{a}})}}{P_{(0\leq r<\infty)}} = 1 - \exp\left(\frac{-2r_{\mathrm{a}}^2}{\omega_0^2 + \left(\frac{\lambda z}{\pi\omega_0}\right)^2}\right). \tag{4.3}$$

So, in order to measure the minimum beam waist, one can simply take into account the light power exiting a pinhole with respect to the position z of the pinhole and fit the data points using equation (4.3), as shown in figure 4.9.

In particular, all z-scan experiments in the present work were performed with a beam waist of $\omega_0 = 50$ μm and a Rayleigh range of $z_{\mathrm{R}} = 14.7$ mm, as obtained from the fits of figure 4.9.

4.5   Electro-optical response experiment setup

In order to investigate the mechanisms behind the director reorientation under an external applied field, an experimental apparatus to measure the transmittance of twisted cells under a varying, electronically-applied, external electric field was built, as shown in figure 4.10. A helium-neon laser (633 nm) polarized vertically was used as our light source. Twisted nematic cells were placed in a hot stage, aligned in a way that the alignment of the first substrate in the optical path matched laser polarization. The light beam exiting the sample was split in two by a beam splitter at the Brewster angle, such that p- and s-waves were properly separated, to be analyzed independently. Each detector was connected to a channel in the oscilloscope (Tektronix TDS 2012 B), which was set in scan mode. The external voltage was applied to the cell by connecting the two ITO-coated glass surfaces to the output channels of a function generator (Tektronix AFG 1022 C), where square-shaped AC voltages at $f = 1.2$ kHz of varying amplitude were generated. Turning the field on, samples take a few milliseconds to fully reorient, and as reorientation occurs, the transmitted signal for each detection channel is also altered. The time-dependent transient profile is then acquired and analyzed.

As a means to enable the execution of several averages for each configuration as well as

Figure 4.10: Experimental apparatus used to indirectly calculate director reorientation times through voltage dependence of the transmitted s- and p-wave intensities. Here, samples are submitted to an external electric field resulting from a function generator outputting a square-wave AC voltage, and the signal obtained by the detectors is directed to the oscilloscope. A computer program controls the amplitude of the applied voltage and captures the resulting time-evolution of the p- and s-wave transmittances. In particular, when $V < V_{th}$, no director reorientation occurs, and no signal change is observed. As V is increased to exceed V_{th}, molecules tend to align themselves parallel to the applied electric field, thus reducing the angle made by the director and the external field (for positive dielectric anisotropy, $\Delta\epsilon > 0$, which is the case for 8CB).
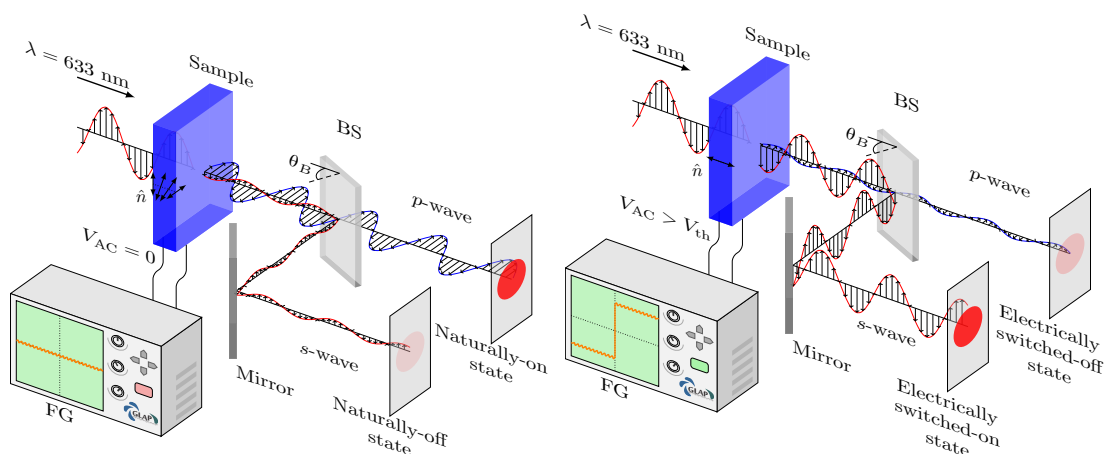
Source: Author (2019).

increase the accuracy of results, a computer script was written in Python programming language. Instruments were connected via USB-B to a USB-A port in the computer and controlled through National Instrument's virtual instrument software architecture application programming interface (NI-VISA API), which enables the computer to send user-defined standard commands for programmable instruments (SCPI) to our electronic equipments [1]. The script consisted of intermittently setting voltages on and off at a defined rate and acquire the time-dependent transmittance signal. Describing in more detail, the voltage was turned on for a couple hundred milliseconds, long enough for steady-state to be reached. After that, the data obtained by the oscilloscope were acquired, unpacked to

---

[1] At the time of writing, the author now realizes that a more elegant, portable, efficient, and lightweight solution could be achieved using different tools. Readers trying to reproduce this or perform similar work are encouraged to employ different methods. The usbtmc module of the Linux kernel, for instance, is recommended in place of the NI-VISA backend. That's because the module makes the kernel see instruments as regular terminals, rendering communication straightforward and any external dependencies superfluous. Fortunately, several Python usbtmc implementations have already been developed. Thus, users willing to stick to a high-level powerful scripting programming language instead of a less resource-hungry, lower-level compiled language should not be discouraged from migrating towards the simpler solution. Currently, the author is working in a multi purpose graphical toolbox to control bench instruments, written in C and GTK 3. The project is yet to be released, but will be made available as free software soon. A quick web search on the author's name is predicted to yield positive results by the time you're reading this.

CSV format, and stored. The voltage was then turned off, a couple hundred milliseconds were waited for stabilization another time, and output files were stored as described before. The voltage was subsequently turned on again, but at a higher amplitude, and the procedure aforementioned repeated in a loop until reaching the final voltage. Ten to fifteen repetitions of the full experiment were performed for each temperature, changing the incidence location within the sample, aiming to minimize local effects. After all repetitions of the experiment for a determined temperature have been performed, another program written in FORTRAN 95 calculated the reorientation time from output data of the Python script and yielded off- and on-time versus voltage curves, together with the corresponding error bars. The temperature was then varied in the hot stage controller, and after 15 min for thermalisation, the procedure described in this paragraph was repeated.

5

Results

In this work, we explore the thermo-optical, nonlinear optical, and electro-optical properties of gold nanorod-doped 8CB samples. The results have been split in two sections, according to the experiments performed and samples studied. The first section is dedicated to the Z-scan experiments, where the thermo-optical and nonlinear optical properties of the homeotropic sample containing $\bar{r} = 2.5$ gold nanords were examined. In the second section, we discuss the results obtained in the electro-optical switching and spectrophotometry experiments, where the twisted samples containing $\bar{r} = 3.0$ and 3.8 gold nanorods were investigated.

5.1   Thermo-optical and nonlinear optical properties of 8CB + AuNR liquid-crystalline systems

Figure 5.1 represents the normalized Z-scan transmittance for homeotropically-aligned 8CB cells containing gold nanorods at two different incidence angles. In both cases, temperature was fixed at $T = 309$ K, which is well above the temperature where the N $\leftrightarrow$ Sm-A phase transition occurs. At the left, we see the optical response of cells at normal incidence, $\phi = 0$, while right shows the optical response at an oblique incidence of $\phi = 5°$. In both curves, scattered gray points represent experimental data, while solid lines are the best fits for Thermal-lens (blue) and Sheik-Bahae (red) models. In particular, left curve shows a valley-peak profile with extrema separation of $\Delta_{\mathrm{vp}} \approx 3.4 z_{\mathrm{R}}$, suggesting that

Figure 5.1: Normalized Z-scan transmittance in closed aperture configuration for homeotropically-aligned samples of 8CB doped with gold nanorods at two incidence angles, normal (left) and $\phi = 5°$ (right). Gray circles represent experimental points. Solid blue and dashed red lines represent the best fits using the Thermal-lens and Sheik-Bahae models, respectively. Sample temperature was set to $T = 309$ K, well above N $\leftrightarrow$ Sm-A phase transition temperature. For normal incidence, the Thermal-lens model shows to be more appropriate, while the Sheik-Bahae model appears to excel at fitting the oblique incidence data. Such feature shows that samples seem to be highly sensitive to incidence angle, leading to the conclusion that phase distortions are governed by different mechanisms in each configuration.
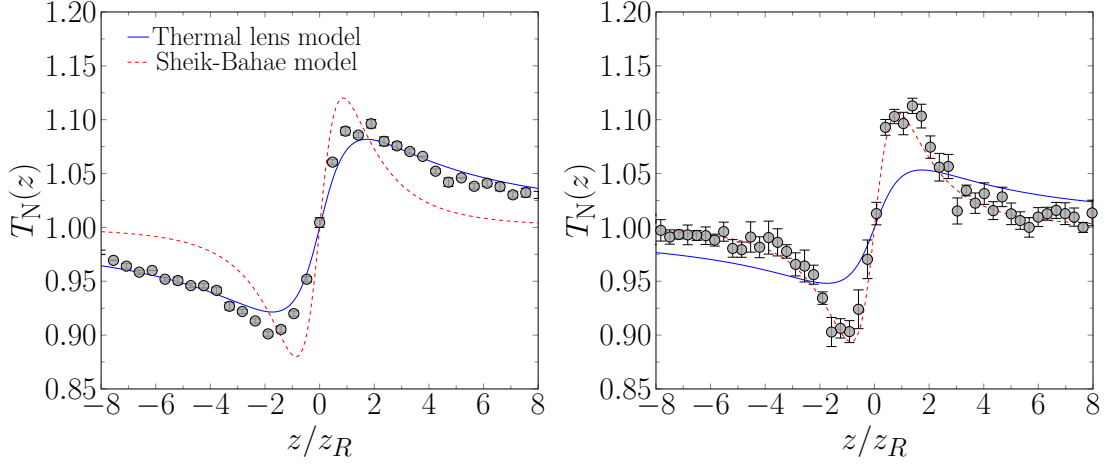
Source: Author (2019).

distortions on the wavefront are caused mainly due to thermal lensing phenomena. When fitting experimental data with the Thermal-lens model described before, one can see that the model suits the data nicely, with a well-adjusted curve for the beam phase shift set to $\theta = -0.153$ rad. The Sheik-Bahae model, on the other hand, doesn't seem to adjust the data well, indicating that neither nonlinear optical absorption nor nonlinear refraction are contributing much to the phase shift and distortions on the exiting wave. Such results lead us to believe that heat generation from nonradiative decay of the plasmon excitation in guest particles provokes a thermally-induced variation in the sample birefringence upon laser exposure. Moreover, previous studies show that even though a collective plasmonic excitation may result in a pronounced nonlinear optical response in homeotropically-aligned samples at wavelengths not far away from the transversal plasmon band [34], the nematic orientational ordering is apparently not sufficient to induce an ensuing strong nonlinear response, and optical nonlinearity may be neglected. The same argument does not hold true for oblique incidence, $\phi = 5°$, where the valley-peak separation is $\Delta_{\mathrm{vp}} \approx 1.8z_{\mathrm{R}}$. If we try to adjust a TL curve fit to the data points, an unsatisfactory result is obtained, even though the self-focusing pattern also present in the TL model persists.

The Sheik-Bahae model, on the other hand, seems to perform a much better job in this case. With a nonlinear phase shift $\Delta\Phi_0 = -0.592$ rad, one can observe that the ensuing curve lays adequately within experimental points. In fact, when light impinges at oblique incidence on a homeotropically-aligned cell, an optically-induced director reorientation occurs, which gives rise to a nonlinearity in the sample refractive index [51, 52]. Such effect is taken into account in the SB model, and even though the incidence angle is rather small ($\phi = 5°$), distortions on the beam wavefront seem to be governed mainly by optically-induced nonlinearities in the refractive index, overtaking thermal effects due to heat generation by plasmonic nanoparticles.

As we have seen before, $\Delta\Phi_0$ is proportional to the nonlinear refraction index, n_2, according to the relation

$$\Delta\Phi_0 = \frac{-2\pi I_0 L_{\text{eff}}}{\lambda} n_2. \tag{5.1}$$

I_0, the input intensity, is easily measured before the experiments. For a low absorption thin sample, $L_{\text{eff}} \approx \ell_0$, and our DPSS laser operated at $\lambda = 532$ nm. In particular, for an incidence angle much larger than the optically-induced director reorientation, n_2 relates to the incidence angle, ϕ, as states the previously derived equation (2.79),

$$n_2 = \frac{\Delta\epsilon_{\text{op}}^2 \ell_0^2}{24 c K_{11}} \sin^2 2\phi. \tag{5.2}$$

$\Delta\epsilon_{\text{op}}$ here is the electrical anisotropy for an optical field, c is the speed of light in vacuum and K_{11} is the splay elastic constant. If we make a simple estimative, taking $\Delta\epsilon_{\text{op}} = 0.48$, $\phi = 5°$ and $K_{11} = 5.40 \times 10^{-7}$ dyn [90], we arrive at an expected nonlinear refractive index of $n_2 \approx 1.79 \times 10^{-5}$ cm^2/W for pristine 8CB samples of $\ell_0 = 100$ μm. Our experiments yield similar results. By fitting closed aperture Z-scan curves for pure 8CB at oblique incidence at $\phi = 5°$, we get $n_2 \approx 1.73 \times 10^{-5}$ cm^2/W, close enough to our estimative. If we take the SB fit for figure 5.1(b), with $\Delta\Phi_0 = -0.592$ rad, the nonlinear refractive index is estimated to be $n_2 \approx 3.48 \times 10^{-5}$ cm^2/W, almost twice as much as that for the undoped sample. As a matter of fact, previous studies have shown that the addition of gold nanorods in cyano-biphenyl samples promotes a significant reduction in the splay

Figure 5.2: Temperature dependence of nonlinear refractive index n_2 for a homeotropic 8CB sample containing gold nanorods. The dashed line is shown to guide the eyes. Notice that the nonlinear refractive index exhibits a pronounced increase in the vicinity of the nematic–smectic-A phase transition.
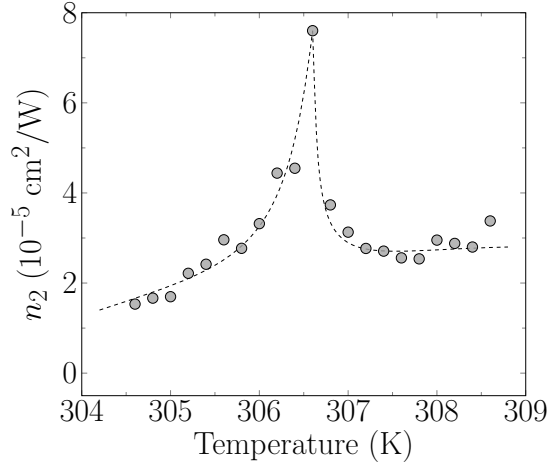
elastic constant, together with a substantial diminution of the temperature dependence of such parameters [91, 37], while the dielectric anisotropy is slightly enhanced in such gold nanorod-LC guest-host systems [92]. Indeed, our results confirm the prediction that gold nanorods in liquid crystal samples should increase nonlinearities in the refraction index.

By adjusting experimental data as those represented in figure 5.1(b) with the SB model for various temperature values, the temperature dependence of n_2 could be obtained, as shown in figure 5.2. The results seem to be in contrast with the thermal behavior predicted by equation (5.2), since the dielectric anisotropy tends to exhibit a slight increase as the temperature approaches the N $\leftrightarrow$ Sm-A phase transition temperature [93], and so does the splay elastic constant [94, 95]. The anomalous increase in the refractive index may be related with a thermally-induced change in the relative angle between the director and the incident beam, due to the emergence of a spatial instability in the orientational order of a homeotropically-aligned nematic liquid crystal film in the vicinity of the N $\leftrightarrow$ Sm-A phase transition [96, 97]. In fact, as temperature decreases and the nematic sample approaches the N $\leftrightarrow$ Sm-A phase transition, the splay elastic constant (K_{11}) remains unchanged, while the twist (K_{22}) and bend (K_{33}) elastic constants diverge to suppress the spatial instability modes. Thus, a new director configuration ensues to hold such enhanced nematic anisotropy, and an optical (or external) electric field-induced director

Figure 5.3: Normalized Z-scan transmittance in open aperture configuration for homeotropically-aligned samples of 8CB doped with gold nanorods at two different temperatures, $T = 302$ K (gray circles), and $T = 305$ K (blue squares). The incidence angle was set to $\phi = 5°$. Solid lines are curve fits according to the Sheik-Bahae model for open aperture. From such curve fits, one may extract β, the nonlinear absorption coefficient.
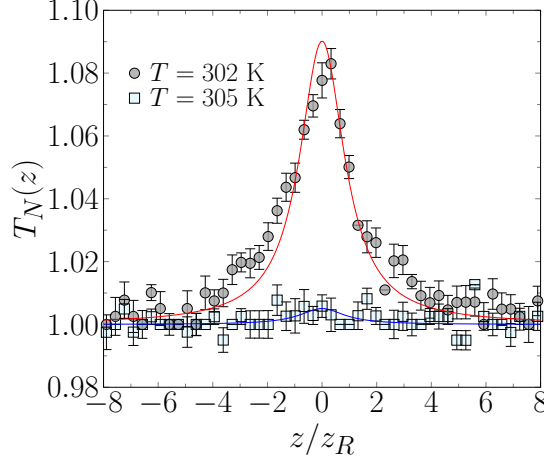
reorientation is observed in homeotropically-aligned liquid crystal films, with an ensuing formation of a striped pattern within the sample [97].

If we analyze the open aperture configuration for the Z-scan experiment, information about thermal effects and nonlinear refraction is lost, but mechanisms related to nonlinear optical absorption become important to the ensuing transmittance, as mentioned in the previous sections. Figure 5.3 presents the curves for the normalized Z-scan transmittance at an oblique incidence ($\phi = 5°$) for homeotropically-aligned 8CB cells doped with gold nanorods at two different temperatures. As we can see, curves stay approximately constant near the N $\leftrightarrow$ Sm-A transition temperature, but as temperature drops, a pronounced peak in the normalized Z-scan transmittance appears at $z = 0$, which is a characteristic behavior of nonlinear optical absorption (in particular, single-photon absorption saturation). This response is a consequence of the strengthening of the smectic order and consequent suppression of fluctuations on the mean alignment of guest nanorods, where a self-organization process may rise to reduce costly elastic perturbations in the energy of the smectic order. Such effect was already reported in the literature for normal incidence, where authors have found that as the temperature of gold nanorod-liquid crystal systems is reduced, the equilibrium configuration may favor the alignment of elongated nanoparticles, giving rise to a saturation in the linear absorption of plasmon bands [34].

Figure 5.4: Dependence of the nonlinear optical absorption coefficient on temperature. Data points were obtained from the best fits of open aperture Z-scan curves at various temperatures, such as curves shown in figure 5.3. As the temperature rises, β tends to a constant value, reflecting the ordering degree of gold nanorod guests inside the liquid crystal host.
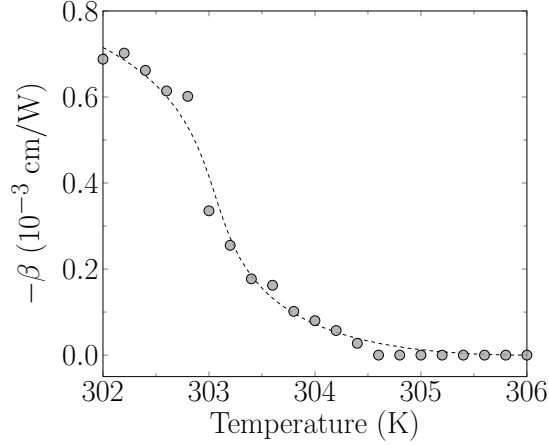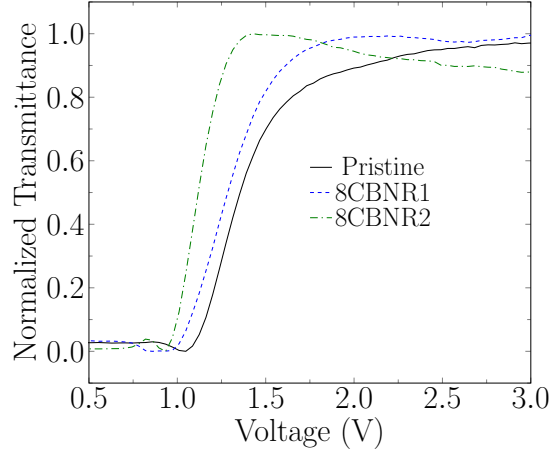

Source: Author (2019).

As oblique incidence is concerned, the angle between the optical field and LC director does not seem to play an important role in the saturation of single-photon absorption in the system.

In figure 5.4, we represent the temperature dependence of the nonlinear optical absorption coefficient, β, for oblique incidence ($\phi = 5°$). The experimental points obtained here come from fitting curves such as figure 5.3 for various temperature values using the SB model. As we have seen before, the open aperture normalized Z-scan transmittance is given by equation (2.82). Since the linear absorption coefficient is small ($\alpha < 1$ cm^{-1}, $\ell_0 \approx 100$ μm), we may assume $L_{\text{eff}} \approx \ell_0$, and β is determined straight away from the free parameter. The input intensity ranged from 5 to 20 kW/cm^2. By examining the plot of $-\beta$ versus T, we see that β is initially negative for lower temperatures, and, as samples are heated, the nonlinear absorption coefficient slowly rises to an apparent constant value. As the temperature is further increased, β rapidly grows to a steady regime of $\beta = 0$, where nonlinear absorption ceases to exist, completely disappearing at $T \approx 2$ K below the N $\leftrightarrow$ Sm-A phase transition temperature. This behavior appears to be a consequence of how the mean alignment of nanorods behaves as temperature drops. For lower temperatures inside the smectic range, a self-organization of the nanorods may occur to reduce energetically costly elastic distortions in the smectic order, favoring the alignment of

Figure 5.5: Steady-state transmittance as a function of applied AC voltage for pristine 8CB, and 8CB doped with gold nanorods at two different aspect ratios, $\bar{r} = 3.0$ (8CBNR1) and $\bar{r} = 3.8$ (8CBNR2). The AC field frequency was fixed at $f = 1.2$ kHz. All measurements have been performed at the same reduced temperature $t_{\mathrm{red}} = |(T/T_{\mathrm{NI}}) - 1| \approx 0.01$, where the nematic order is well established (approximately 3 K below N $\leftrightarrow$ I transition temperature). As disorder is introduced through colloidal guests in 8CB, the threshold voltage is slightly decreased and the transmittance reaches a plateau at lower voltages. As aspect ratio is increased, such plateau is attained at even lower voltages.
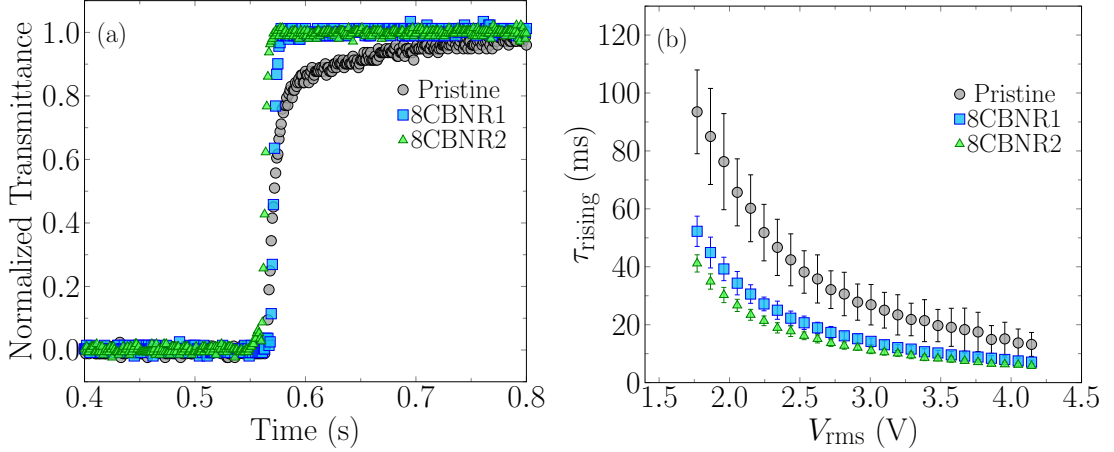

Source: Author (2019).

elongated colloids and ensuing a saturation of the linear absorption of plasmonic bands. Similar behavior has been observed in polymeric films, where an enhanced absorptive nonlinearity is obtained from the nanorods alignment induced by the film stretching [98].

5.2 Electro-optical response of twisted nematic samples containing gold nanorods

By applying a square-wave shaped external AC electric field with $f = 1.2$ kHz and acquiring the resulting steady-state intensities for the exiting s-wave of the probe beam (as shown in figure 4.10), the normalized steady-state transmittance as a function of the amplitude of the external field could be obtained as shown in figure 5.5, for pristine (solid black), 8CBNR1 (dashed blue), and 8CBNR2 (dash-dot green) twisted nematic samples. Here, all measurements have been performed approximately at the same reduced temperature, $t_{\mathrm{red}} = |(T/T_{\mathrm{NI}}) - 1| \approx 0.01$, well below the N $\leftrightarrow$ I phase transition. As one can see, both the Freedericksz reorientation and optical thresholds are lowered when the colloids are added to our liquid crystal. In particular, the pristine sample presents a

Figure 5.6: Transient intensities (a) for pristine and gold nanorod-doped 8CB, where gold nanorods come at two different aspect ratios, $\bar{r} = 3.0$ (8CBNR1) and $\bar{r} = 3.8$ (8CBNR2). From the time interval required by each sample to go from 0.1 to 0.9 of total intensity, τ_{rising} versus voltage could be obtained as shown in (b). The AC field frequency was fixed at $f = 1.2$ kHz. All measurements have been performed at the same reduced temperature, $t_{\text{red}} = |(T/T_{\text{NI}}) - 1| \approx 0.01$, where the nematic order is well established (approximately 3 K below N $\leftrightarrow$ I phase transition temperature). In order to eliminate imperfections and local effects, experiments were performed at 15 different sample positions. The gold nanorod-doped samples reach steady state much faster than pristine one, with more elongated particles presenting an even faster electro-optical response, together with a more systematical decrease of response times, where error bars shrink considerably, indicating a decrease of inconsistencies due to sample positioning.

Source: Author (2019).

reorientation threshold at $V_{\text{th}} = 950$ mV, while in both gold nanorod-doped samples this value was reduced to $V_{\text{th}} = 750$ mV. The optical threshold was also dramatically reduced when the guests were added to 8CB, being even lower in the sample containing the more elongated particles. Furthermore, the maximum transmittance state is reached at much lower voltages as impurities are introduced and the aspect ratio is increased. More specifically, the nanoparticles capped with CTAB induce a homeotropic alignment over their surface, provoking the appearance of topological defects around them. The lowering in Freedericksz transition voltage is likely related to elastic distortions in the nematic order induced by the colloid guests, where the ensuing configuration may yield different elastic constants in order to accommodate the presence of generated defects.

In order to evaluate the effects of guest particles in the viscoelastic constants, the dynamics of the Freedericksz transition is analyzed. By acquiring the time-dependent curves for the ensuing s-wave transmittance, several curves such as figure 5.6(a) could be obtained. Here, we show an example of resulting transmittances in response to the time evolution of the director profile for pristine 8CB (gray circles), 8CBNR1 (blue squares),

and 8CBNR2 (green triangles) for an AC square-wave voltage with an amplitude of $V = 4$ V at $f = 1.2$ kHz and approximately the same reduced temperatures ($t_{\text{red}} = |(T/T_{\text{NI}}) - 1| \approx 0.01$). As we can see, the steady-state configuration is reached much faster for gold nanorod-doped samples, with an even faster response for the sample containing more elongated particles. By calculating the time interval required by each configuration to go from 10% ($I(\tau_{10}) = 0.1 \cdot I(\tau \to \infty)$) to 90% ($I(\tau_{90}) = 0.9 \cdot I(\tau \to \infty)$) of the total transmittance, one can calculate $\tau_{\text{rising}} = \tau_{90} - \tau_{10}$, the characteristic switching time for each sample at each voltage. We have then acquired time-dependent transmittance curves such as shown in figure 5.6(a) for various voltages, and repeated the experiment with the incident beam impinging the cell at 15 different positions on each sample in order to reduce local effects and ease artifacts due to imperfections. An average of $\tau_{\text{rising}}(V)$ for each of the 15 experiments was calculated and is shown in figure 5.6(b), together with the respective error bars. As one can see, the introduction of gold nanorods significantly reduces the reorientation times, with the switching times being slightly faster in 8CBNR2 than 8CBNR1. Such reduction of response times is also accompanied by a systematical decrease of error bar size, indicating that the response is also more consistent and reliable than in pristine samples. In particular, τ_{rising} is dependent on the applied voltage as follows [99, 61]

$$\tau_{\text{rising}} = \left(\frac{\gamma_1 d^2}{\pi^2 k}\right) \frac{1}{(V/V_{\text{th}})^2 - 1}, \tag{5.3}$$

where γ_1 here is the rotational viscosity and $k = K_{11} - (2K_{22} - K_{33})/4$ is an effective elastic constant for the twist sample. One can fit the voltage dependence of the characteristic reorientation times using equation (5.3) to calculate the ratio γ_1/k. Our calculations reveal a ratio of 23.7 mPa·s/pN for the pristine sample, 16.8 mPa·s/pN for 8CBNR1, and 12.8 mPa·s/pN for 8CBNR2. As one may observe, the presence of impurities and subsequent increase of aspect ratio decreases the viscoelastic constant γ_1/k, reducing the reorientation times.

Figure 5.7(a) shows transmission spectra for 8CBNR1 between parallel polarizers, with the incident light polarization being parallel to the input alignment of the cell. Here, we can see the typical transmittance profile for a twisted nematic sample placed between

Figure 5.7: Transmission spectra are shown in (a) for 8CB doped with $\bar{r} = 3.0$ nanoparticles (8CBNR1) for three temperatures, all within the nematic phase range. One can note that, as the temperature is lowered, a redshift of the Mauguin minima is observed, leading to an increase of the birefringence, as expected. From the position of the Mauguin minima observed and its consequent minimum number identification, one can use the single-band model to calculate the ensuing temperature dependence of birefringence at $\lambda = 633$ nm, as shown in (b). Notice that the addition of gold nanorods reduces the discontinuity in the birefringence observed at the N $\leftrightarrow$ I phase transition.
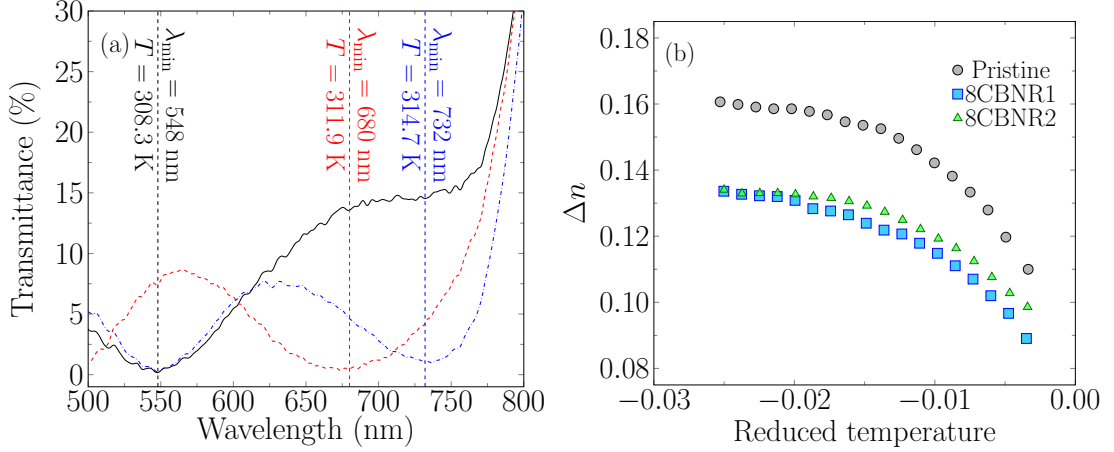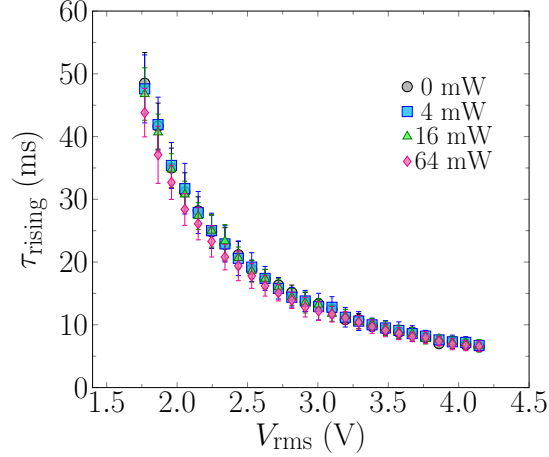

Source: Author (2019).

parallel polarizers, as shown in previous sections, for $T = 314.7$ K (blue), $T = 311.9$ K (red) and $T = 308.3$ K (black). One can note how the Mauguin minima shifts to longer wavelengths as temperature is decreased. By slowly cooling samples, the thermal dependence of the Mauguin minima position can be obtained, and the system birefringence can be calculated according to the Gooch-Tarry conditions. Such value for the birefringence is, however, valid for the Mauguin minima only. Using the single-band model, already described in previous sections, we can accurately estimate Δn for $\lambda = 633$ nm. In particular, 8CB presents absorption peaks at $\lambda_0 = 200$ nm, $\lambda_1 = 220$ nm and $\lambda_2 = 282$ nm, resulting in an average of $\bar{\lambda}^2 = (\lambda_0^2 + \lambda_1^2 + \lambda_2^2)/3 \approx (237 \text{ nm})^2$. The thermal behavior of the birefringence is shown in figure 5.7 for pristine 8CB (gray circles), 8CBNR1 (blue squares) and 8CBNR2 (green triangles). Note that a decrease in birefringence is observed for temperatures where the nematic order is well established, together with a reduction of the birefringence discontinuity near the N $\leftrightarrow$ I phase transition, indicating that the presence of colloid guests induce an emergence of disorder in the orientational order of the molecules.

In order to examine the contribution of the surface plasmon resonance to director re-orientation times, a pump beam was aimed at the 8CBNR2 sample and the electro-optical

Figure 5.8: Optical switching times versus voltage for 8CB samples doped with $\bar{r} = 3.8$ gold nanorods for different powers of longitudinal plasmonic excitation. The sample was pumped by a DPSS laser beam at $\lambda = 785$ nm, close to the longitudinal plasmonic extinction peak of $\bar{r} = 3.8$ gold nanorods. The external AC voltage had the same frequency $f = 1.2$ kHz, and the temperature was set to $t_{red} = |(T/T_{NI}) - 1| \approx 0.01$, the same setup as figure 5.6. Curves show that the electro-optical response is roughly independent of excitation power, indicating that the elastic distortions induced by nanoparticles shape are responsible for the decrease in τ_{rising} over the plasmonic nature of such guests.
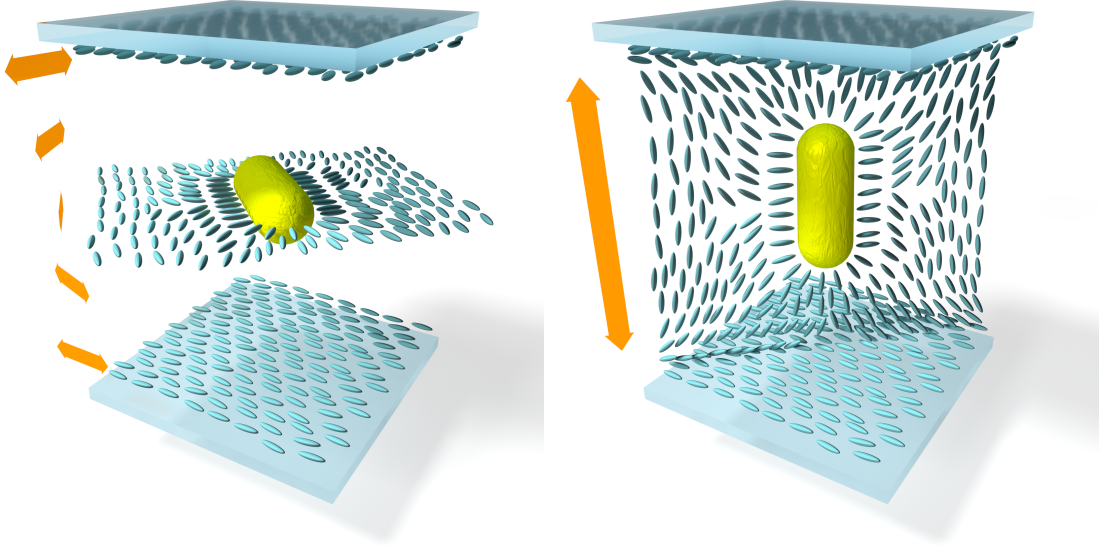

Source: Author (2019).

experiment related above was repeated with various excitation powers, ranging from 0 to 64 mW. The laser pump operated at $\lambda = 785$ nm (OBIS DPSS laser, by Coherent), close to the longitudinal plasmonic extinction peak of $\bar{r} = 3.8$ gold nanorods (754 nm). The pump beam spot covered the whole sample, in order to assure the maximum excitation area possible. Again, experiments for each excitation power were performed at the usual temperature of $t_{red} = |(T/T_{NI}) - 1| \approx 0.01$, and points obtained from 15 different sample positions were used to calculate an average $\tau_{rising}(V)$, with their respective error bars. Our results are summarized in figure 5.8. As one can notice, plasmonic effects do not seem to play a major role in the reorientation dynamics, with effects associated with the local electric field near nanoparticles being overtaken by elastic distortions induced in the nematic order, even though plasmonic effects having previously shown to be leading thermo-optical and nonlinear phenomena [34, 100, 101].

More specifically, CTAB capped gold nanorods induce a homeotropic alignment of the liquid crystal molecules over their surfaces. A scheme of the director alignment over the nanoparticles is shown in figure 5.9. When no reorientation is present ($V < V_{th}$), the twist configuration prevails, as shown in (a). Meanwhile, when the applied field exceeds the threshold voltage, the far field director tends to align itself parallel to the external

Figure 5.9: Schematic representation of a gold nanorod inside a twisted nematic cell with homeotropic anchoring expected at the LC-gold interface, as imposed by CTAB. Note how molecules align perpendicular to the surface of the nanoparticle, inducing a disclination ring around its center. The presence of such defects reduce the orientational order of the system and yields the modifications observed in the viscoelastic properties of the sample. In (a), the characteristic configuration of the director under twisted anchoring conditions is represented, while the director profile for samples undergone a Freedericksz transition is shown in (b). Specifically, colloidal nanorods tend to align themselves parallel to the director [102, 34].

Source: Author (2019).

field, depicted in (b). In particular, such topological defects induce disorder in the sample and consequently reduce the elastic constants due to a lowering in the orientational order parameter, leading to smaller values of the Freedericks threshold voltage. This behavior has been previously shown to hold for nematic samples in parallel planar (homogeneous alignment) cells containing gold nanoparticles [102]. The effects of the introduction of gold nanorods in nematic samples on the rotational viscosity can be understood by analyzing the Osipov-Terentjev framework, which states that the rotational viscosity of the sample can be expressed as [103]

$$\gamma_1 = \frac{\rho \xi}{6 v_m} \sqrt{\frac{\bar{J}_0 s}{k_{\mathrm{B}} T}} \exp\left(\frac{\bar{J}_0 s}{k_{\mathrm{B}} T} \right), \tag{5.4}$$

where ρ is the mass density, ξ is the molecular frictional coefficient, v_m is the molecular volume, $\bar{J}_0$ is the mean field coupling and s the order parameter. Due to the low concentration of colloids, the volume fraction of molecules is only slightly changed, with effects related to the molecular frictional coefficient being negligible. Expression 5.4 shows,

however, that the rotational viscosity is strongly sensitive to alterations in the order parameter. As we have discussed before, the nematic order parameter is reduced as the gold nanorods are introduced in the systems, leading to a decrease in the ensuing rotational viscosity. Figure 5.7(b) further confirms our assertion, since the sample birefringence is proportional to the nematic order parameter ($\Delta n \propto s$).

6

Concluding remarks

In conclusion, we have first studied the thermo-optical and nonlinear optical response of 8CB liquid crystals containing gold nanorods. The extinction spectra analysis has showed us how thermal fluctuations are important in the mean alignment of gold nanorods, where a strong suppression of the longitudinal plasmon peak together with a significant boost in the transversal peak follows on homeotropic samples as temperature is reduced and the smectic order begins to establish itself. By investigating normalized Z-scan curves for closed aperture configuration, we have found that birefringence changes leading to lensing phenomena are governed by two distinct mechanisms according to beam incidence angle. Thermal effects are predominant in the regime of normal incidence, where nanorods act as individual heat sources within the liquid crystal host, due to plasmonic excitation of the extinction bands. When oblique incidence is concerned, however, thermal lensing is no longer dominant, with birefringence changes occurring due to director reorientations in response to light's electric field. Such observations lead us to conclude that the incidence angle is rather important, because both gold nanorod mean alignment and the director orientation are extremely sensitive to excitation angle. At normal incidence, director reorientation is hindered, while transversal plasmonic excitation reaches its peak, making thermal effects prevalent, due to the colloids acting as heat sources. When beam incidence is changed to oblique, however, plasmonic excitation of extinction bands are hamstrung, leading to thermal effects being overthrown by optically-induced changes in the birefringence, as a result of director reorientation. Moreover, an anomalous behavior

has been observed for the temperature dependence of the nonlinear refractive index n_2 at the vicinity of the N $\leftrightarrow$ Sm-A phase transition, where a spatial instability may occur due to the enhanced nematic anisotropy of the elastic constants [97], yielding an enhanced optically-induced director reorientation and consequent boosted nonlinear refraction response. For the open aperture configuration, a peak centered at $z = 0$ in the Z-scan transmittance curve surges as temperature drops to values well below the N $\leftrightarrow$ Sm-A phase transition temperature, for both normal and oblique incidence. The dependence on temperature of the nonlinear optical absorption coefficient is then obtained for oblique incidence by adjusting the Sheik-Bahae model for open aperture normalized Z-scan curves. Our results show that even though changes in birefringence due to optically-induced director reorientation were dominant in the closed aperture configuration, surface plasmon resonance still plays an important role in nonlinear optical absorption, with a negative nonlinear absorption coefficient appearing for temperatures where the smectic order is well established, and increasing in absolute value until reaching an apparent plateau.

The director reorientation properties have also been explored, through the analysis of the resulting transmittance of twisted nematic samples under an AC voltage for pure 8CB, and 8CB containing gold nanorods in two different aspect ratios. By applying a square-wave voltage at $f = 1.2$ kHz and awaiting for transient effects to die out, the steady-state transmittance and, indirectly, the equilibrium director configuration could be obtained for various voltages. As nanorod guests were added to 8CB, Freedericksz reorientation threshold voltages were lowered, keeping constant for both aspect ratios of gold nanorod guests. The Freedericksz optical threshold, however, was also lowered as impurities were added to 8CB, but presented a slight decrease as the aspect ratio was increased. Such reduction is related with a greater degree of disorder being induced in the samples due to elastic distortions in the orientational order. Moreover, steady-state transmittance curves presented a pronounced enhancement in steepness, with gold nanorod-doped samples reaching near-complete transmission at much lower voltages than the pristine one. In particular, such effect was more evident in the sample containing the more elongated particles. The dynamic behavior of the director was also evaluated, and a

significant decrease of reorientation times was reported as disorder centers were introduced in 8CB, with an even faster response for the sample containing the higher aspect ratio gold nanorods. By analysing the thermal dependence of the birefringence for each sample according to the transmission spectra, we could conclude that such reduction is associated with a drop of the rotational viscosity, caused by the decrease of the order parameter, as predicted by the Osipov-Terentjev framework. Such behavior is a consequence of the disrupting of the nematic orientational order around the anisotropic nanoparticles. Even though the reported increase of the nematic-isotropic phase transition temperature may at first sight seem contradictory with the overall reduction of the order parameter together with a slight suppression of the discontinuity at the phase transition, both phenomena are led by different mechanisms. In the former, the dilution effect related to the excluded volume contribution plays a major role, in contrast to the second. Furthermore, the plasmonic contribution to reorientation times was evaluated, where results show that the local electric field caused by the plasmonic nature of gold nanorods does not present much significance compared to elastic distortions in the nematic orientational order produced by guest nanoparticles shapes, despite being crucial to thermo-optical and nonlinear optical phenomena.

Bibliography

[1] P. G. de Gennes and J. Prost. *The Physics of Liquid Crystals*. Clarendon Press, 2 edition, 1995.

[2] Charles Kittel. *Introduction to Solid State Physics*. LTC, 8 edition, 2006.

[3] Neil W. Ashcroft and Nathaniel D. Mermin. *Solid State Physics*. Cengage Learning, 1 edition, 1976.

[4] David Chandler. *Introduction to Modern Statistical Mechanics*. Oxford University Press, 1 edition, 1987.

[5] N. Boccara. Violation of rotational invariance and mesomorphic phase transitions characterized by an order parameter. *Annals of Physics*, 76:72–79, 1973.

[6] Alenka Mertelj and Darja Lisjak. Ferromagnetic nematic liquid crystals. *Liquid Crystals Reviews*, 5:1–33, 2017.

[7] M. Schadt. Low-Frequency Dielectric Relaxations in Nematics and Dual-Frequency Addressing of Field Effects. *Molecular Crystals and Liquid Crystals*, 89:77–92, 2006.

[8] Yuhua Huang, Ying Zhou, Charlie Doyle, and Shin-Tson Wu. Tuning the photonic band gap in cholesteric liquid crystals by temperature-dependent dopant solubility. *Optics Express*, 14:1236–1242, 2006.

[9] Tatsunosuke Matsui, Masanori Ozaki, and Katsumi Yoshino. Tunable photonic defect modes in a cholesteric liquid crystal induced by optical deformation of helix. *Physical Review E*, 69:061715–061719, 2004.

[10] Jisoo Hwang, Myoung Hoon Song, Byoungchoo Park, Suzushi Nishimura, Takehiro Toyooka, J. W. Wu, Yoichi Takanishi, Ken Ishikawa, and Hideo Takezoe. Electro-tunable optical diode based on photonic bandgap liquid-crystal heterojunctions. *Nature Materials*, 4:383–387, 2005.

[11] Heino Finkelmann, Sung Tae Kim, Antonio Munoz, Peter Palffy-Muhoray, and Bahman Taheri. Tunable Mirrorless Lasing in Cholesteric LiquidCrystalline Elastomers. *Advanced Materials*, 13:1069–1072, 2001.

[12] Weny Cao, Antonio Munoz, Peter Palffy-Muhoray, and Bahman Taheri. Lasing in a three-dimensional photonic crystal of the liquid crystal blue phase II. *Nature Materials*, 1:111–113, 2002.

[13] Yuhua Huang, Ying Zhou, and Shin-Tson Wu. Spatially tunable laser emission in dye-doped photonic liquid crystals. *Applied Physics Letters*, 88:011107–011110, 2006.

[14] Andro Chanishvili, Guram Chilaya, Gia Petriashvili, Riccardo Barberi, Roberto Bartolino, Gabriella Cipparrone, Alfredo Mazzulla, Raquel Gimenez, Luis Oriol, and Milagros Pinol. Widely tunable ultraviolet-visible liquid crystal laser. *Applied Physics Letters*, 86:051107–051110, 2005.

[15] N. Konforti, E. Marom, and S.-T. Wu. Phase-only modulation with twisted nematic liquid-crystal spatial light modulators. *Optics Letters*, 13:251–253, 1988.

[16] Jeffrey A. Davis, Ignacio Moreno, and Philbert Tsai. Polarization eigenstates for twisted-nematic liquid-crystal displays. *Applied Optics*, 37:937–945, 1998.

[17] E. G. van Putten, I. M. Vellekoop, and A. P. Mosk. Spatial amplitude and phase modulation using commercial twisted nematic LCDs. *Applied Optics*, 47:2076–2081, 2008.

[18] Shin-Tson Wu and Chiung-Sheng Wu. Mixed-mode twisted nematic liquid crystal cells for reflective displays. *Applied Physics Letters*, 68:1455–1457, 1996.

[19] David Shrekenhamer, Wen-Chen Chen, and Willie J. Padilla. Liquid Crystal Tunable Metamaterial Absorber. *Physical Review Letters*, 110:177403–177408, 2013.

[20] Salvatore Savo, David Shrekenhamer, and Willie J. Padilla. Liquid Crystal Metamaterial Absorber Spatial Light Modulator for THz Applications. *Advanced Optical Materials*, 2:275–279, 2014.

[21] Douglas H. Werner, Do-Hoon Kwon, Iam-Choon Khoo, Alexander V. Kildishev, and Vladimir M. Shalaev. Liquid crystal clad near-infrared metamaterials with tunable negative-zero-positive refractive indices. *Optics Express*, 15:3342–3347, 2007.

[22] Qian Zhao, Lei Kang, Bo Du, Bo Li, and Ji Zhoua. Electrically tunable negative permeability metamaterials based on nematic liquid crystals. *Applied Physics Letters*, 90:011112–011115, 2007.

[23] Alexander Minovich, James Farnell, Dragomir N. Neshev, Ian McKerracher, Fouad Karouta, Jie Tian, David A. Powell, Ilya V. Shadrivov, Hark Hoe Tan, Chennupati Jagadish, and Yuri S. Kivshar. Liquid crystal based nonlinear fishnet metamaterials. *Applied Physics Letters*, 100:121113–121117, 2012.

[24] R. Pratibha, K. Park, I. I. Smalyukh, and W. Park. Tunable optical metamaterial based on liquid crystal-gold nanosphere composite. *Optics Express*, 17:19459–19469, 2009.

[25] R.B. Meyer, L. Liebert, L. Strzelecki, and P. Keller. Ferroelectric liquid crystals. *Journal de Physique Letters*, 36:69–71, 1975.

[26] L. A. Bresnev, V. G. Chigrinov, D. I. Dergachev, E. P. Poshidaev, J. Fuenfschilling, and M. Schadt. Deformed helix ferroelectric liquid crystal display: A new electrooptic mode in ferroelectric chiral smectic C liquid crystals. *Liquid Crystals*, 5:1171–1177, 1989.

[27] G. H. Heilmeier and L. A. Zanoni. Guest-host interactions in liquid crystals, a new electro-optic effect. *Applied Physics Letters*, 13:91, 1968.

[28] Helmut Ringsdorf and Hans-Werner Schmidt. Electro-optical effects of azo dye containing liquid crystalline copolymers. *Macromolecular Chemistry and Physics*, 185:1327–1334, 1984.

[29] Lena M. Lopatina and Jonathan V. Selinger. Theory of Ferroelectric Nanoparticles in Nematic Liquid Crystals. *Physical Review Letters*, 102:197802, 2009.

[30] Oleksandr Buchnev, Andriy Dyadyusha, Malgosia Kaczmarek, Victor Reshetnyak, and Yuriy Reznikov. Enhanced two-beam coupling in colloids of ferroelectric nanoparticles in liquid crystals. *Journal of the Optical Society of America B*, 24:1512–1516, 2007.

[31] I. Smalyukh. Liquid Crystal Colloids. *Annual Review of Condensed Matter Physics*, 9:207–226, 2018.

[32] Ye Yuan, Angel Martinez, Bohdan Senyuk, Mykola Tasinkevych, and Ivan I. Smalyukh. Chiral liquid crystal colloids. *Nature Materials*, 17:71–79, 2018.

[33] Michael G. Campbell, Mykola Tasinkevych, and Ivan I. Smalyukh. Topological Polymer Dispersed Liquid Crystals with Bulk Nematic Defect Lines Pinned to Handlebody Surfaces. *Physical Review Letters*, 112:197801, 2014.

[34] P. B. de Melo, A. M. Nunes, L. Omena, S. M. S. do Nascimento, M. G. A. da Silva, M. R. Meneghetti, and I. N. de Oliveira. Thermo-optical properties and nonlinear optical response of smectic liquid crystals containing gold nanoparticles. *Physical Review E*, 92:042504, 2015.

[35] O. Kurochkin, Y. K. Murugesan, T. P. Bennett, G. D'Alessandro, Y. Reznikov, B. J. Tang, G. H. Mehl, and M. Kaczmarek. Thermal optical non-linearity of nematic mesophase enhanced by gold nanoparticles - an experimental and numerical investigation. *Physical Chemistry Chemical Physics*, 18:11503–11512, 2016.

[36] V. M. Lenart, R. F. Turchiello, G. F. Goya, and S. L. Gómez. Enhanced Thermal Lens Effect in Gold Nanoparticle-Doped Lyotropic Liquid Crystal by Nanoparticle Clustering Probed by Z-Scan Technique. *Brazilian Journal of Physics*, 45:213–218, 2015.

[37] P. L. Madhuri, S. K. Prasad, P. Shinde, and B. L. V. Prasad. Large reduction in the magnitude and thermal variation of Frank elastic constants in a gold nanorod/nematic composite. *Journal of Physics D: Applied Physics*, 49:425304–425313, 2016.

[38] Qingkun Liu, Ye Yuan, and Ivan I. Smalyukh. Electrically and optically tunable plasmonic guest-host liquid crystals with long-range ordered nanoparticles. *Nano Letters*, 14:4071–4077, 2014.

[39] Ghadah H. Sheetah, Qingkun Liu, and Ivan I. Smalyukh. Self-assembly of pre-designed optical materials in nematic codispersions of plasmonic nanorods. *Optics Letters*, 41:4899–4902, 2016.

[40] J. P. Gordon, R. C. C. Leite, R. S. Moore, S. P. S. Porto, and J. R. Whinnery. Long-Transient Effects in Lasers with Inserted Liquid Samples. *Journal of Applied Physics*, 36:3–8, 1965.

[41] M. Giglio and A. Vendramini. Thermal lens effect in a binary liquid mixture: A new effect. *Applied Physics Letters*, 25:555–557, 1974.

[42] W. Koechner. Thermal Lensing in a Nd:YAG Laser Rod. *Applied Optics*, 9:2548–2553, 1970.

[43] S. J. Sheldon, L. V. Knight, and J. M. Thorne. Laser-induced thermal lens effect: a new theoretical model. *Applied Optics*, 21:1633–1669, 1982.

[44] Christine A. Carter and Joel M. Harris. Comparison of models describing the thermal lens effect. *Applied Optics*, 23:476–481, 1984.

[45] Christine A. Carter and Joel M. Harris. Comparison of single- and dual-beam configurations for thermal lens spectrometry. *Analytical Chemistry*, 55:1256–1261, 1983.

[46] John R. Whinnery. Laser measurement of optical absorption in liquids. *Accounts of Chemical Research*, 7:225–231, 1974.

[47] Orazio Svelto. *Principles of Lasers.* Springer, 5 edition, 2009.

[48] M. Sheik-Bahae, A. A. Said, and E. W. Van Stryland. High-sensitivity, single-beam n_2 measurements. *Optics Letters*, 14:955–957, 1989.

[49] Mansoor Sheik-Bahae, Ali A. Said, Tai-Huei Wei, David J. Hagan, and E. W. Van Stryland. Sensitive Measurement of Optical Nonlinearities Using a Single Beam. *IEEE Journal of Quantum Electronics*, 26:760–769, 1990.

[50] D. Weaire, B. S. Wherrett, D. A. B. Miller, and S. D. Smith. Effect of low-power nonlinear refraction on laser-beam propagation in InSb. *Optics Letters*, 4:331–333, 1979.

[51] Iam Choon Khoo. Nonlinear optics, active plasmonics and metamaterials with liquid crystals. *Progress in Quantum Electronics*, 38:77–117, 2014.

[52] Demetrios N. Christodoulides, Iam Choon Khoo, Gregory J. Salamo, George I. Stegeman, and Eric W. Van Stryland. Nonlinear refraction and absorption: mechanisms and magnitudes. *Advances in Optics and Photonics*, 2:60–200, 2010.

[53] Iam-Choon Khoo and Shin-Tson Wu. *Optics and Nonlinear Optics of Liquid Crystals.* World Scientific, 1 edition, 1993.

[54] Joseph A. Castellano. Modifying Light: Ubiquitous today, liquid-crystal displays are the outgrowth of more than a century of experimentation and development. *American Scientist*, 94:438–445, 2006.

[55] M. Schadt and W. Helfrich. Voltage-dependent optical activity of a twisted nematic liquid crystal. *Applied Physics Letters*, 18:127–128, 1971.

[56] F. M. Leslie. Distortion of Twisted Orientation Patterns in Liquid Crystals by Magnetic Fields. *Molecular Liquid Crystals and Liquid Crystals*, 12:57–72, 1970.

[57] J. L. Ericksen. Inequalities in Liquid Crystal Theory. *The Physics of Fluids*, 9:1205–1207, 1966.

[58] F. C. Frank. On the Theory of Liquid Crystals. *Discussions of the Faraday Society*, 25:19–28, 1958.

[59] Constantine M. Dafermos. Stability of orientation patterns of liquid crystals subject to magnetic fields. *SIAM Journal of Applied Mathematics*, 16:1305–1318, 1968.

[60] Alfred Saupe. Die Biegungselastizitaet der nematischen Phase von Azoxyanisol. *Zeitschrift fuer Naturforschung A*, 15:815–822, 1960.

[61] L. M. Blinov and V. G. Chigrinov. *Electrooptic Effects in Liquid Crystal Materials*. Springer-Verlag, 1 edition, 1994.

[62] Hp. Schad. The rotational viscosity of nematic liquid crystal mixtures at low temperatures. *Journal of Applied Physics*, 4994:4994, 1983.

[63] Shin-Tson Wu, Uzi Efron, and LaVerne D. Hess. Birefringence measurements of liquid crystals. *Applied Optics*, 23:3911–3915, 1984.

[64] H. L. Ong. Origin and characteristics of the optical properties of general twisted nematic liquid crystal displays. *Journal of Applied Physics*, 64:614–628, 1988.

[65] S. Teitler and B. W. Henvis. Refraction in stratified anisotropic media. *Journal of the Optical Society of America*, 60:830, 1970.

[66] Dwight W. Berreman. Optics in Stratified and Anisotropic Media: 4×4-Matrix Formulation. *Journal of the Optical Society of America*, 62:502–510, 1972.

[67] Ralph J. Gagnon. Liquid-crystal twist-cell optics. *Journal of the Optical Society of America*, 71:348–353, 1981.

[68] H. Woehler, G. Haas, M. Fritsch, and D. A. Mlynski. Faster 4x4 matrix method for uniaxial inhomogeneous media. *Journal of the Optical Society of America A*, 5:1554–1557, 1988.

[69] P. J. Lin-Chung and S. Teitler. 4x4 Matrix formalisms for optics in stratified anisotropic media. *Journal of the Optical Society of America A*, 1:703–705, 1984.

[70] Robert C. Jones. A New Calculus for the Treatment of Optical Systems I. Description and Discussion of the Calculus. *Journal of the Optical Society of America*, 31:488–493, 1941.

[71] C. H. Gooch and H. A. Tarry. The optical properties of twisted nematic liquid crystal structures with twist angles $\leq$ 90 degrees. *Journal of Physics D*, 8:1575–1584, 1975.

[72] Jun Li and Shin-Tson Wu. Self-consistency of Vuks equations for liquid-crystal refractive indices. *Journal of Applied Physics*, 96:6253–6258, 2004.

[73] John D. Jackson. *Classical Electrodynamics*. Wiley, 2 edition, 1962.

[74] Paul Lorrain and Dale Corson. *Electromagnetic fields and waves*. W. H. Freeman, 2 edition, 1970.

[75] L. Lorenz. Ueber die Refractionsconstante. *Annalen der Physik*, 247:70–103, 1880.

[76] H. A. Lorentz. Ueber die Anwendung des Satzes vom Virial in der kinetischen Theorie der Gase. *Annalen der Physik*, 248:127, 1881.

[77] C. W. Bunn and R. de. P. Daubeny. The polarizabilities of carbon—carbon bonds. *Transactions of the Faraday Society*, 50:1173, 1954.

[78] H. E. J. Neugebauer. Clausius-Mosotti equation for certain types of anisotropic crystals. *Canadian Journal of Physics*, 32:1–8, 1954.

[79] W. H. de Jeu and P. Bordewijk. Physical studies of nematic azoxybenzenes. II. Refractive indices and the internal field. *Journal of Chemical Physics*, 68:109–115, 1978.

[80] M. F. Vuks. . *Optische Spektroskopie*, 20:644, 1966.

[81] G. Vertogen and W. H. de Jeu. *Thermotropic Liquid Crystals, Fundamentals*. Springer-Verlag, 1 edition, 1988.

[82] L. M. Blinov. *Structure and Properties of Liquid Crystals*. Springer, 1 edition, 2011.

[83] V. Astapenko. *Polarization Bremsstrahlung on Atoms, Plasmas, Nanostructures and Solids*. Springer-Verlag, 1 edition, 2013.

[84] Shin-Tson Wu. Birefringence dispersions of liquid crystals. *Physical Review A*, 33:1270–1274, 1986.

[85] Shin-Tson Wu. A semiempirical model for liquid-crystal refractive index dispersions. *Journal of Applied Physics*, 69:2080–2087, 1990.

[86] Monique G. A. da Silva, Ábner M. Nunes, Simoni M. P. Meneghetti, and Mario R. Meneghetti. New aspects of gold nanorod formation via seed-mediated method. *Comptes Rendus Chimie*, 16:640–650, 2013.

[87] G. W. Gray, K. J. Harrison, and J. A. Nash. New family of nematic liquid crystals for displays. *Electronics Letters*, 9:130–131, 1973.

[88] George W. Gray. Reminiscences from a life with liquid crystals. *Liquid Crystals*, 24:5–13, 1998.

[89] K. H. Yang. Measurements of empty cell gap for liquid-crystal displays using interferometric methods. *Journal of Applied Physics*, 64:4780–4781, 1988.

[90] M.J. Bradshaw, E.P. Raynes, J.D. Bunning, and T.E. Faber. The Frank constants of some nematic liquid crystals. *Journal de Physique France*, 46:1513–1520, 1985.

[91] K. K. Vardanyan, E. D. Palazzo, and R. D. Walton. Nematic nanocomposites with enhanced optical birefringence. *Liquid Crystals*, 38:709–715, 2011.

[92] S. Sridevi, S. Krishna Prasad, Geetha G. Nair, Virginia D'Britto, and B. L. V. Prasad. Enhancement of anisotropic conductivity, elastic, and dielectric constants in a liquid crystal-gold nanorod system. *Applied Physics Letters*, 97:151913, 2010.

[93] Sudeshna DasGupta, Pinku Chattopadhyay, and Soumen Kumar Roy. Effect of a rigid nonpolar solute on the splay, bend elastic constants, and on rotational viscosity coefficient of 4,4′-n-octyl-cyanobiphenyl. *Physical Review E*, 63:041703, 2001.

[94] F. Jaehnig and F. Brochard. Critical elastic constants and viscosities above a nematic-smectic a transition of second order. *Journal de Physique France*, 35:301–313, 1974.

[95] Patrick Oswald and Camille Scalliet. Measurements of the dielectric and viscoelastic constants in mixtures of 4,4′-n-octyl-cyanobiphenyl and biphenyl. *Physical Review E*, 89:032504, 2014.

[96] P. E. Cladis and S. Torza. Growth of a smectic-A from a bent nematic phase and the smectic light valve. *Journal of Applied Physics*, 46:584–599, 1975.

[97] Corinne Chevallard and Marcel G. Clerc. Inhomogeneous Freedericksz transition in nematic liquid crystals. *Physical Review E*, 65:011708, 2001.

[98] Claudio Conti, Marco Peccianti, and Gaetano Assanto. Observation of Optical Spatial Solitons in a Highly Nonlocal Medium. *Physical Review Letters*, 92:113902, 2004.

[99] R. V. dos Santos, P. B. de Melo, A. M. Nunes, M. R. Meneghetti, M. L. Lyra, and I. N. de Oliveira. Electro-optical switching in twisted nematic samples doped with gold nanorods. *Journal of Molecular Liquids*, 295:111704–111712, 2019.

[100] D. Lysenko, E. Ouskova, S. Ksondzyk, V. Reshetnyak, L. Cseh, G. H. Mehl, and Y. Reznikov. Light-induced changes of the refractive indices in a colloid of gold nanoparticles in a nematic liquid crystal. *The European Journal of Physics E*, 35:33–40, 2012.

[101] Nina Podoliak, Dorota Bartczak, Oleksandr Buchnev, Antonios G. Kanaras, and Malgosia Kaczmare. High Optical Nonlinearity of Nematic Liquid Crystals Doped with Gold Nanoparticles. *The Journal of Physical Chemistry C*, 116:12934–12939, 2012.

[102] Q. Liu, Y. Cui, D. Gardner, X. Li, S. He, and I. I. Smalyukh. Self-Alignment of Plasmonic Gold Nanorods in Reconfigurable Anisotropic Fluids for Tunable Bulk Metamaterial Applications. *Nano Letters*, 10:1347–1353, 2010.

[103] M. A. Osipov and E. M. Terentjev. Rotational diffusion and rheological properties of liquid crystals. *Zeitschrift Naturforsch*, 44:785–792, 1988.